

# Deep part load operation of combined cycles and combined heat and power plants

Marco Persico



# Deep part load operation of combined cycles and combined heat and power plants

by

## Marco Persico

to obtain the degree of Master of Science  
at the Delft University of Technology,  
to be defended publicly on Friday 21 April, 2017 at 14:00.

Student number: 4420047  
Project duration: August 1, 2016 – April 21, 2017  
Thesis committee: Prof. dr. ir. S. Klein, TU Delft, supervisor  
Dr. ir. B. J. Boersma, TU Delft  
Dr. ir. A. Gangoli Rao, TU Delft  
Ir. G. J. Otero, TU Delft



# Preface

I would like to thank Dr. Sikke Klein for his excellent guidance during this project. Sincere thanks go to Gustavo Otero Rodriguez and Simone Silvestri for giving me advices.

I wanna express my profound gratitude to "Famiglia Persico" for always supporting me and for being emotionally close during my studies. The last words go to America for always encouraging me and for endless patience during this months.

**Marco Persico**  
*Delft, April 2017*



# Abstract

The world energy market has become very volatile due to the increase of renewable sources of power (solar and wind energy) and it asks more flexibility to fossil power stations. Gas turbines are of great importance for the generation of power both in combined cycles and in combined heat and power installations. If in the past gas turbines operated on a continuous basis (base load), nowadays there is the necessity for gas turbines to operate at part load during periods of excess of renewables. Up to now, many combined cycles and combined heat and power installations show little flexibility and their contribution to grid stability is limited. Vendors use several traditional techniques to part-load gas turbines: decreasing firing temperature, decreasing inlet airflow (inlet guide vane closure), recirculating the compressor airflow or a combination of these techniques. The cycle efficiency drops significantly at part load when using these traditional control techniques. Furthermore, traditional gas turbine control techniques struggle to keep emission levels low (NO<sub>x</sub> and CO). An option to overcome these problems is the use of Flue Gas Recirculation (FGR) for which the gas turbine flue gases are recirculated to the gas turbine inlet. When recirculating the flue gases, the inlet temperature of the gas turbine will rise resulting in a lower mass flow through the installation and lower power production. Flue Gas Recirculation has been studied before in the literature to increase the CO<sub>2</sub> content and decrease the NO<sub>x</sub> content in flue gases but not to allow part load operation. The uniqueness of this research is to enable part load operation of combined heat and power plants and combined cycles with FGR. In particular, there is a lack of studies on the impact of FGR on the thermodynamic cycle and the gas turbines components (e.g. compressor and turbine). In order to investigate the part load controls, a model of a Brayton cycle has been developed and validated with THERMOFLEX. The results show that FGR is more efficient than the other part load controls for both the combined heat and power plants and combined cycles. In particular, the use of FGR can theoretically increase the cycle efficiency of the combined heat and power plants at part load up to 9% with respect to traditional control techniques.



# Contents

<b>Abstract</b>	<b>v</b>
<b>List of Figures</b>	<b>ix</b>
<b>List of Tables</b>	<b>xiii</b>
<b>Abbreviations</b>	<b>xv</b>
<b>List of Symbols</b>	<b>xvii</b>
<b>1 Introduction</b>	<b>1</b>
1.1 Gas turbines for power generation . . . . .	1
1.2 Recovery of exhaust heat from Gas Turbines . . . . .	2
1.3 Development of energy markets . . . . .	3
1.4 Part load operation . . . . .	4
1.5 Objective of the thesis. . . . .	5
1.6 Outline of the report . . . . .	5
<b>2 Part load operation of gas turbines</b>	<b>7</b>
2.1 Theoretical background. . . . .	7
2.2 Off-design operation . . . . .	9
2.2.1 Compressor airflow . . . . .	9
2.2.2 GT pressure ratio. . . . .	12
2.3 Engine control theory. . . . .	14
2.3.1 Turbine inlet temperature control . . . . .	14
2.3.2 Inlet guide vanes control . . . . .	15
2.3.3 Compressor airflow recirculation (CAR) . . . . .	17
2.3.4 Flue gases recirculation (FGR) . . . . .	20
2.3.5 Part load efficiency. . . . .	23
2.4 Conclusions. . . . .	24
<b>3 Part load operation of a combined heat and power plant</b>	<b>25</b>
3.1 Modeling of the CHP plant . . . . .	25
3.2 Part load operation . . . . .	28
3.2.1 TIT control. . . . .	29
3.2.2 IGV control . . . . .	29
3.2.3 CAR control . . . . .	30
3.2.4 FGR control . . . . .	31
3.2.5 Part load efficiency. . . . .	32
3.3 Conclusions. . . . .	35
<b>4 Part load operation of Combined Cycles</b>	<b>37</b>
4.1 Combined cycles (CC) . . . . .	37
4.2 Design of a Combined Cycle . . . . .	38
4.3 Part load operation . . . . .	40
4.3.1 Steam turbines load . . . . .	40
4.3.2 Part load efficiency. . . . .	42
4.4 Conclusions. . . . .	45
<b>5 Impact of part load operation on the turbine vane/blade temperature</b>	<b>47</b>
5.1 Cooling of gas turbines . . . . .	47
5.1.1 External cooling . . . . .	48
5.1.2 Internal cooling . . . . .	49

---

5.2	Turbine cooling equations . . . . .	51
5.2.1	External heat transfer ( $Q_{ext}$ ) . . . . .	52
5.2.2	Internal heat transfer ( $Q_{int}$ ) . . . . .	56
5.3	Part load operation . . . . .	62
5.3.1	Coolant flow . . . . .	63
5.3.2	Off-design simulations. . . . .	64
5.4	Conclusions. . . . .	65
<b>6</b>	<b>Case study including duct/blower calculations and limitation imposed by the turbine blade temperature</b>	<b>67</b>
6.1	Proposed solutions to the limitation imposed by the turbine temperature . . . . .	67
6.1.1	FGR&TIT+ IGV combination control. . . . .	68
6.1.2	IGV + FGR&TIT combination control . . . . .	68
6.2	Blower . . . . .	69
6.3	Summary and conclusions . . . . .	72
<b>7</b>	<b>Conclusions and recommendations</b>	<b>73</b>
7.1	Conclusions. . . . .	73
7.2	Recommendations . . . . .	74
	<b>Bibliography</b>	<b>81</b>

# List of Figures

1.1	Schematic of a gas turbine. C is the compressor, CC is the combustion chamber and T is the turbine. . . . .	1
1.2	General electric gas turbine [5]. . . . .	2
1.3	The picture shows the Combined Cycle Power Plant Enecogen in The Netherlands. . . . .	2
1.4	Average annual growth rates of renewable electricity in electricity consumption [22]. . . . .	3
1.5	Electricity shares of renewables by 2030-2040 [22]. . . . .	3
1.6	German wind power production in 2012 [29]. . . . .	4
1.7	Relative combined cycle efficiency drop at part load [20]. . . . .	4
2.1	Brayton model - flow diagram. . . . .	7
2.2	Brayton model: T-S diagram at the design point. . . . .	8
2.3	Compressor operation at part load (blue line) for a corrected speed line (constant compressor inlet temperature and shaft rotational speed). . . . .	9
2.4	Variable inlet guide vanes. . . . .	10
2.5	Absolute velocity vector at the GT inlet when the airflow is not purely axial ( $\alpha_1 > 0$ ). . . . .	10
2.6	Velocity triangles at the outlet of the inlet guide vanes (compressor intake). The inlet guide vanes causes the absolute velocity vector to rotate by the angle $\alpha_{IGV}$ . . . . .	11
2.7	Turbine nozzle (stator) and rotor. . . . .	12
2.8	Model validation: GT pressure ratio versus TIT for THERMOFLEX (red line) and the developed model (blue line). The error is less than 0.6%. . . . .	14
2.9	T-S diagram of Brayton cycle for TIT control: the cycle in black defines the Brayton cycle at the design conditions whereas the other in red represents the cycle when the GT load is 70% and $T_{3OD} = 980^\circ\text{C}$ . . . . .	15
2.10	T-S diagram of Brayton cycle for IGV control: the cycle in black defines the Brayton cycle at the design point whereas the other in red represents the cycle when the GT load is 80% and $\alpha_{IGV} = 12.5^\circ$ . . . . .	15
2.11	Brayton model. The GT power (a) and compressor airflow (b) decrease when closing the inlet guide vanes. . . . .	16
2.12	Model validation: GT pressure ratio versus GT airflow for THERMOFLEX (red line) and the developed model (blue line). The error is less than 0.1%. . . . .	16
2.13	Compressor map - IGV control. The blue line is the design corrected iso-speed line (constant compressor inlet temperature and shaft rotational speed). The map shows the minimum value of inlet airflow when closing the inlet guide vanes. In reality, the surge line slightly shifts to the left improving the surge margin [26]. The worst case scenario is considered and the surge margin line is assumed to not shift. . . . .	17
2.14	Simple Brayton model: flow diagram for CAR. . . . .	17
2.15	T-S diagram of Brayton cycle for CAR control: the cycle in black defines the Brayton cycle at the design point whereas the other one in red represents the cycle when the engine load is 64% and $T_{1OD} = 45^\circ\text{C}$ . . . . .	18
2.16	Simple Brayton model for CAR control: Compressor inlet temperature vs GT power and fraction recirculated. The black curve (a) shows how the output power decreases when the compressor inlet temperature rises whereas the red curve (b) calculates the required fraction (of airflow) recirculated. For instance, if 10 % of the airflow is recirculated, the compressor inlet temperature will rise up to $55^\circ\text{C}$ for a GT power of approximately 20 MW. . . . .	18
2.17	Model validation: compressor discharge pressure versus GT airflow for THERMOFLEX (red line) and the developed model (blue line). The error is less than 0.1%. . . . .	19
2.18	Compressor map - CAR control. The blue lines represent the operation of the compressor at different iso-corrected speeds (constant inlet temperature and shaft rotational speed). When recirculating the compressor airflow, the surge margin is respected. . . . .	19

2.19	Simple Brayton model: flow diagram for FGR. . . . .	20
2.20	T-S diagram of Brayton cycle for FGR control: the cycle in black defines the Brayton cycle at the design point whereas the other one in red represents the cycle when the engine load is 85.3% and $T_{1OD} = 35^{\circ}\text{C}$ . . . . .	20
2.21	Simple Brayton model for FGR control: Compressor inlet temperature vs GT power and fraction (of flue gases) recirculated. The compressor inlet temperature rises because a fraction of the flue gases is recirculated (b) causing the output power to reduce(a). For instance, if 6% of the flue gases are recirculated, the compressor inlet temperature will rise up to $50^{\circ}\text{C}$ for a cycle output power of approximately 26 MW. . . . .	21
2.22	Simple Brayton model: combustion. . . . .	21
2.23	Model developed: compressor discharge pressure versus GT airflow for THERMOFLEX (red line) and the developed model (blue line). The error is less than 0.7%. . . . .	22
2.24	Simple Brayton model: compressor inlet temperature vs GT power for CAR and FGR controls. . . . .	22
2.25	Compressor map - FGR control. The blue lines represent the operation of the compressor at different iso-corrected speeds (constant inlet temperature and shaft rotational speed). When recirculating the flue gases, the surge margin is respected. . . . .	23
2.26	Brayton model: GT efficiency vs GT power for all the part load techniques. . . . .	23
3.1	CHP plant flow diagram. . . . .	25
3.2	CHP plant: T-Q diagram at the design conditions. Negative values of Q express the amount of heat required in the SFU to keep the process heat $Q_{HRSG}$ constant. . . . .	26
3.3	CHP plant: energy balance. . . . .	27
3.4	T-Q diagram for TIT control. Negative values of Q express the amount of heat required in the SFU to keep the process heat $Q_{HRSG}$ constant. The dotted lines (- - -) represents the HRSG operation when the CHP load is 50%. . . . .	29
3.5	T-Q diagram for IGV control. Negative values of Q express the amount of heat required in the SFU to keep the process heat $Q_{HRSG}$ constant. The dotted lines (- - -) represents the HRSG operation for the minimum achievable CHP load of 82%. . . . .	30
3.6	T-Q diagram for CAR control. Negative values of Q express the amount of heat required in the SFU to keep the process heat $Q_{HRSG}$ constant. The dotted lines (- - -) represents the HRSG operation when the CHP load is 50 %. . . . .	30
3.7	(a) FGR control for CHP plant - Mole percentage of $O_2$ at the inlet of the gas turbine. (b) FGR control for CHP plant: fraction of exhaust gases recirculated to the gas turbine inlet . . . . .	31
3.8	T-Q diagram for FGR control. Negative values of Q express the amount of heat required in the SFU to keep the process heat $Q_{HRSG}$ constant. The dotted lines (- - -) represents the HRSG operation for the minimum CHP load of 68 %. . . . .	31
3.9	CHP plant: Delta stack losses $\Delta Q_{StackOD}$ at part load for the developed control techniques. . . . .	32
3.10	CHP efficiency vs $GT_{load}$ for different control techniques . . . . .	32
3.11	Brayton cycle: Delta stack losses $\Delta Q_{StackOD}$ at part load for the developed control techniques. The lower the stack losses, the higher the part load efficiency. . . . .	33
3.12	(a) CHP efficiency at part load for combined controls: FGR + IGV combination control (b) CHP efficiency at part load for optimum combined control (FGR + TIT + IGV) control. . . . .	33
3.13	CHP plant: Standard control technique combination used in industry. The IGVs are closed up to the limit position and later on the TIT temperature is decreased. . . . .	34
3.14	CHP plant control combination: (a)marginal efficiency $\eta_{marg} = \frac{\eta_{optimum} - \eta_{standard}}{\eta_{standard}}$ , (b)CHP efficiency of the optimum & standard combined controls. . . . .	34
4.1	Schematic flow diagram of the CC. The detailed flow diagram is shown in the appendix. . . . .	38
4.2	CC: ST h-s diagram at design. The blue curves represent the water/steam saturation curves and steam isobars. The red iso-temperature curve shows that when exiting the high pressure turbine, the steam is reheated before being expanded in the intermediate ST. . . . .	39
4.3	Combined cycle: energy balance. . . . .	39
4.4	CC: $Q_{HRSG}$ versus GT exhaust flow keeping the BIT constant (a) & BIT keeping the GT exhaust flow constant (b). . . . .	40
4.5	CC: $ST_{load}$ (a) & steam/water flow in the condenser (b) versus $CC_{load}$ . . . . .	41

4.6	(a) $\Delta Q_{stack}$ for the different part load techniques. (b) $\Delta Q_{cond}$ for the different part load techniques. . . . .	42
4.7	CC: delta system losses $\Delta Q_{losses}$ for the different part load techniques. The delta system losses are equal to the sum of the delta condensation and delta stack losses. . . . .	43
4.8	CC efficiency at part load. . . . .	43
4.9	Optimum CC control combination: (a) CC efficiency & (b) Boiler inlet temperature at part load. The boiler inlet temperature is maintained below $BIT_{limit}$ due to the limitation imposed by the material properties of the wall insulation of the boiler and of the turbine. . . . .	44
4.10	Standard CC control combination: (a) CC efficiency & (b) Boiler inlet temperature at part load. . . . .	44
4.11	CC control combination: (a) marginal efficiency $\eta_{marg} = \frac{\eta_{optimum} - \eta_{standard}}{\eta_{standard}}$ , (b) CC efficiency of the optimum & standard combined controls. . . . .	45
5.1	Cycle efficiency as a function of the firing temperature and pressure ratio for a compressor efficiency of 87% and turbine efficiency of 92% [5]. . . . .	47
5.2	Increase of the TIT over the years [16]. . . . .	48
5.3	Blade/vane external heat transfer: film cooling. . . . .	49
5.4	Blade cooling mechanisms in gas turbines [16]. . . . .	49
5.5	Internal cooling: jet impingement nozzle. . . . .	50
5.6	Blade cooling mechanisms in gas turbines: jet impingement . . . . .	50
5.7	Turbine cooling: vanes/blades shape. . . . .	51
5.8	Multi-layered surface of blade. . . . .	51
5.9	Schematic temperature profile in a blade. . . . .	52
5.10	Turbine blade cooling: vanes/blades shape simplification. . . . .	53
5.11	Stagnation point (red area) in the leading edge. . . . .	53
5.12	Turbine blade cooling - film cooling [5]. . . . .	54
5.13	Internal cooling: longitudinal cut of the cooling channels in a turbine blade/vane . . . . .	57
5.14	Turbine cooling model. Design calculations of the coolant outlet temperature for convection cooling. The solution converges for infinite numbers of discretizations. . . . .	58
5.15	Internal cooling: jet impingement array. . . . .	59
5.16	Internal cooling: velocity distribution in jet impingement array. . . . .	60
5.17	Turbine cooling model. Cross flow velocity (a) and Nusselt number per jet (b) for impingement cooling. . . . .	61
5.18	Turbine cooling model. Heat transfer coefficient per jet for impingement cooling. . . . .	61
5.19	Turbine cooling model. Coolant mass flow at part load. . . . .	63
5.20	Turbine cooling model. Coolant pressure(a) and temperature (b) at part load. . . . .	63
5.21	Turbine cooling model. Blade temperature profile at part load for FGR and IGV controls for the middle-trailing(a) and leading(b) edges. . . . .	64
5.22	Turbine cooling model for FGR control. Percent of metal temperature increase if the coolant composition would not change. . . . .	65
5.23	Turbine cooling model for FGR control. Film cooling effectiveness at part load for IGV and FGR controls. . . . .	65
6.1	Optimum control combination for the CHP plant of chapter 3. . . . .	67
6.2	Case study. FGR&TIT+ IGV combination control (including control of maximum turbine blade temperature) (a) and turbine blade temperature profile at part load. . . . .	68
6.3	Case study. IGV + FGR&TIT combination control (including control of maximum turbine blade temperature). . . . .	69
6.4	CHP plant flow diagram with blower. . . . .	69
6.5	Fitting pressure losses for a 90°C curved elbow [17]. . . . .	70
6.6	Velocity profile in the recirculating duct for the deep part load control. . . . .	71
6.7	Blower power(a) and CHP plant efficiency drop (b) with respect to the optimum control with turbine cooling limitations of figure 6.2a . . . . .	71
6.8	Results of the case study: combined heat and power plant efficiency at part load for the different controls. . . . .	72
7.1	Combined cycle flow diagram at design. . . . .	77

---

7.2	Turbine cooling model. External heat transfer for IGV control. . . . .	78
7.3	Turbine cooling model. Internal heat transfer for convection cooling (a) and impingement cooling (b) for IGV control. . . . .	78
7.4	Turbine cooling model. External heat transfer for FGR control. . . . .	79
7.5	Turbine cooling model. Internal heat transfer for convection cooling (a) and impingement cooling (b) for FGR control. . . . .	79

# List of Tables

3.1	Selected gas turbine for the CHP plant. . . . .	26
3.2	CHP plant - HRSG design values . . . . .	26
4.1	Gas turbine selected for the CC . . . . .	38
4.2	CC: design values of the boiler/HRSG . . . . .	38
5.1	Vanes/blades geometric design. . . . .	52
5.2	Turbine cooling model: external heat transfer design calculations for the middle-trailing edge. . . . .	55
5.3	Turbine cooling model: external heat transfer design calculations for the leading edge. . . . .	56
5.4	Cooling channels geometry . . . . .	56
5.5	Turbine cooling model. Design results for internal cooling in the middle-trailing edge. . . . .	58
5.6	Design impingement cooling - geometry parameters. . . . .	59
5.7	Constants to use in equation (5.35) [15]. . . . .	60
5.8	Turbine cooling model. Design results for internal cooling in the leading edge. . . . .	62
5.9	FGR for CHP plant. Volumetric percentage composition at the GT inlet. Data taken from chapter 3. . . . .	62



# Abbreviations

<i>AP</i>	Air pre-heating
<i>BIT</i>	Boiler inlet temperature
<i>CAR</i>	Compressor airflow recirculation
<i>CC</i>	Combined cycle
<i>CHP</i>	Combined heat and power
<i>CMR</i>	Coolant to main-stream ratio
<i>ED</i>	Engineering design
<i>FGR</i>	Flue gas recirculation
<i>GT</i>	Gas turbine
<i>HRSG</i>	Heat recovery steam generator
<i>IGV</i>	Inlet guide vanes
<i>LHV</i>	Lower heating value
<i>OD</i>	Off-design
<i>SFU</i>	Supplementary firing unit
<i>STIT</i>	Steam turbine inlet temperature
<i>TIT</i>	Turbine inlet temperature
<i>UHC</i>	Unburned hydrocarbons



# List of Symbols

$A_1$	Compressor suction area
$A_{3n}$	Throat area
$A_{conv}$	Heat transfer area due to convective heat transfer
$A_{CC}$	Cooling channel cross section area
$A_{duct}$	Duct cross sectional area
$A_{ext}$	External heat transfer area
$A_{int}$	Internal heat transfer area
$A_j$	Jet impingement area
$BIT$	Boiler inlet temperature
$BIT_{limit}$	Maximum boiler inlet temperature
$c_{3n}$	Sound speed at the turbine throat
$c_p$	Air heat capacity at constant pressure
$c_{pFG}$	Flue gases heat capacity at constant pressure
$C_d$	Dimensionless friction factor for distributed pressure losses
$C_f$	Dimensionless friction factor for fitting pressure losses
$C_D$	Jet discharge coefficient
$CC_{load}$	Combined cycle load
$CMR$	Coolant to main-stream ratio
$CMR_{conv}$	Coolant to main-stream ratio for convective heat transfer
$CMR_{imp}$	Coolant to main-stream ratio for impingement heat transfer
$d_h$	Hydraulic diameter of the cooling channel
$d_j$	Jet diameter
$D_{duct}$	Duct diameter
$D_{hole}$	Film hole diameter
$GT_{load}$	Gas turbine load
$h$	Chord height
$h_{conv}$	Heat transfer coefficient due to convective heat transfer
$h_{in}$	Water enthalpy at the inlet of the HRSG
$h_{int}$	Heat transfer coefficient due to internal heat transfer
$h_{imp}$	Averaged heat transfer coefficient due to impingement heat transfer
$h_{out}$	Water enthalpy at the outlet of the HRSG
$h_{ext}$	Heat transfer coefficient due to external heat transfer
$h_{stack}$	Enthalpy of air at ambient conditions
$h_{amb}$	Enthalpy of air at ambient conditions
$H_{CC}$	Cooling channel height
$k$	Air isentropic exponent
$k_{FG}$	Flue gases isentropic exponent
$k_g$	Thermal conductivity of resin bounded glass-wool
$k_h$	Conductivity of the hot gases
$k_s$	Thermal conductivity of the super alloy
$l$	Chord length
$L$	Duct length
$L_{jx}$	Stream-wise length
$L_{jy}$	Span-wise length
$\dot{m}_a$	Gas turbine airflow
$\dot{m}_{coolant}$	Coolant airflow
$\dot{m}_{aOD}$	OD gas turbine airflow

$\dot{m}_{cond}$	Water/steam flow in the condenser
$\dot{m}_{condOD}$	OD water/steam flow in the condenser
$\dot{m}_{conv}$	Coolant airflow for convective heat transfer
$\dot{m}_{duct}$	Duct mass flow
$\dot{m}_{imp}$	Coolant airflow for impingement heat transfer
$\dot{m}_f$	Gas turbine fuel flow
$\dot{m}_{fOD}$	OD gas turbine fuel flow
$\dot{m}_w$	Water/steam flow in the HRSG
$\dot{m}_{wOD}$	OD water/steam flow in the HRSG
$\dot{m}_j$	Coolant mass flow
$M$	Bowing rate
$M_{a4}$	Mach number at turbine exhaust
$n_{CC}$	Number of cooling channels
$n_j$	Number of jets
$n_{jx}$	Number of jets stream-wise
$n_{jy}$	Number of jets span-wise
$Nu$	Nusselt number of the hot gases for internal heat transfer
$Nu_h$	Nusselt number of the hot gases for external heat transfer
$P_1$	Compressor inlet pressure
$P_2$	Compressor discharge pressure
$P_{03}$	Turbine inlet total pressure
$P_3$	Turbine inlet pressure
$P_{3n}$	Turbine pressure at the throat
$P_4$	Turbine discharge pressure
$P_{1OD}$	OD Compressor inlet pressure
$P_{2OD}$	OD Compressor discharge pressure
$P_{3OD}$	OD Turbine inlet pressure
$P_{4OD}$	OD Turbine discharge pressure
$P_{ev}$	Water evaporation pressure
$P_{1ev}$	Water evaporation level - first pressure level of the HRSG
$P_{2ev}$	Water evaporation level - first pressure level of the HRSG
$P_{3ev}$	Water evaporation level - first pressure level of the HRSG
$P_0$	Total pressure
$P_{blower}$	Blower shaft power
$P_{el}$	Cycle output power
$Pr$	Prandtl number of the cooling gases for internal heat transfer
$Pr_h$	Prandtl number of the hot gases for external heat transfer
$q$	steam quality
$Q_{boiler}$	Boiler heat
$Q_c$	Channel cross-flow mass flow per unit area
$Q_{channel}$	Internal heat transfer due to convective heat transfer in one cooling channel
$Q_{conv}$	Internal heat transfer due to convective heat transfer
$Q_{ext}$	External heat transfer
$\dot{Q}_f$	Cycle fuel input (or cycle fuel consumption)
$Q_{imp}$	Internal heat transfer due to impingement
$Q_{SFU}$	Heat added in the SFU
$Q_{HRSG}$	Process heat
$Q_{losses}$	Cycle losses
$Q_{stack}$	Stack losses
$Q_{cond}$	Condensation losses
$Q_j$	Coolant flow per unit area
$Re_h$	Reynolds number of the hot gases
$Re_j$	Reynolds number of the jet nozzle
$R$	Gas constant of ambient air

$R_h$	Gas constant of the hot flue gases
$R_s$	Heat transfer resistance due to conduction
$Re$	Reynolds number of the coolant flow
$Re_h$	Reynolds number of the hot gases
$Re_{duct}$	Reynolds number in the recirculating duct
$S_1$	Specific entropy of air at the compressor inlet
$S_2$	Specific entropy of air at the compressor outlet
$S_3$	Specific entropy of flue gases at the turbine inlet
$S_4$	Specific entropy of flue gases at the turbine outlet
$STIT$	Steam turbine inlet temperature
$ST_{load}$	Steam turbines load
$t_i$	Thickness of the duct insulation
$t_s$	Thickness of the super alloy
$TIT$	Turbine inlet temperature
$T_1$	Compressor inlet temperature
$T_2$	Compressor discharge temperature
$T_{03}$	Turbine inlet total temperature
$T_3$	Turbine inlet temperature
$T_{03n}$	Total temperature at the turbine throat
$T_{3n}$	Temperature at the turbine throat
$T_4$	Turbine discharge temperature
$T_5$	Flue gases temperature at the inlet of the HRSG temperature
$T_c$	Coolant temperature
$T_{cond}$	Water/steam condensation temperature
$T_{in}$	Water temperature at the inlet of the HRSG
$T_h$	Static hot gas temperature
$T_{out}$	Water temperature at the outlet of the HRSG
$T_{stack}$	Flue gases temperature at the outlet of the HRSG / stack temperature
$T_{1OD}$	OD Compressor inlet temperature
$T_{2OD}$	OD Compressor discharge temperature
$T_{3OD}$	OD Turbine inlet temperature
$T_{4OD}$	OD Turbine discharge temperature
$T_{5OD}$	OD Flue gases temperature at the inlet of the HRSG temperature
$T_f$	Film temperature
$T_{condOD}$	OD Water/steam condensation temperature
$T_{inOD}$	OD Water temperature at the inlet of the HRSG
$T_{outOD}$	OD Water temperature at the outlet of the HRSG
$T_{stackOD}$	OD Flue gases temperature at the outlet of the HRSG / stack temperature
$T_{max}$	Maximum blade temperature
$T_{wi}$	Inner wall temperature
$T_{wo}$	Outer wall temperature
$V_1$	Velocity of the exhaust flow in the duct
$V_1$	Compressor flow velocity
$V_{1ax}$	Compressor axial flow velocity
$V_3$	Turbine inlet velocity
$V_m$	Coolant velocity in the cooling channel
$w$	Velocity of the hot gases
$w_c$	Chord width
$\dot{W}_c$	Compressor shaft power
$\dot{W}_t$	Turbine shaft power
$W_{CC}$	Cooling channel width
$x_{CAR}$	Fraction of airflow recirculated
$x/d$	Stream-wise distribution
$y/d$	Span-wise distribution
$z/d$	Height distribution

**Greek letters**

$\alpha_1$	Compressor inlet velocity angle
$\alpha_{IGV}$	Inlet guide vanes angle
$\beta$	Flow distribution parameter
$\chi$	Streamwise distance from the film holes
$\Delta P_{duct}$	Duct pressure losses
$\Delta P_d$	Distributed pressure losses
$\Delta P_f$	Fitting pressure losses
$\Delta Q_{cond}$	Delta condensation losses
$\epsilon$	Film cooling effectiveness parameter
$\epsilon_{duct}$	Surface roughness
$\eta_{CHP}$	Efficiency of the combined heat and power plant
$\eta_{CC}$	Efficiency of the combined cycle
$\bar{\eta}_f$	Streamwise and laterally averaged film effectiveness
$\bar{\eta}_{f,lat}$	Laterally averaged film effectiveness
$\eta_{blower}$	Blower efficiency
$\eta_{isC}$	Compressor isentropic efficiency
$\eta_{isT}$	Turbine isentropic efficiency
$\eta_{GT}$	Gas turbine efficiency
$\eta_{marg}$	Marginal efficiency
$\pi$	Gas turbine pressure ratio
$\pi_{OD}$	OD Gas turbine pressure ratio
$\rho_{duct}$	density of the exhaust air
$\rho_1$	Compressor inlet density
$\rho$	Coolant density
$\rho_h$	Hot gases density
$\mu$	Coolant dynamic viscosity
$\mu_h$	Hot gases dynamic viscosity

# Introduction

This section provides an overview of the gas turbine technology for power generation and introduces the combined cycles and combined heat and power plants. The importance of part load operation for fossil power station is presented in section 1.3. However, the main issue of part load operations is that the cycle efficiency drops significantly when using traditional control techniques [6, 20]. Flue gas recirculation (FGR) is presented as a possible solution to this issue in section 1.4 and the structure of the report is outlined.

## 1.1. Gas turbines for power generation

Gas turbines (GT) are continuous flow machines which produce a great amount of energy considering their size and weight. Figure 1.1 shows the schematic of a gas turbine. In their simpler form, gas turbines are characterized by 4 thermodynamic processes: compression (1-2), heat addition by combustion (2-3) and expansion in a turbine (3-4). The working fluid of gas turbines is usually air. They are suitable for working with multiple fuels such as natural gas, methane, diesel, and biomass gases.

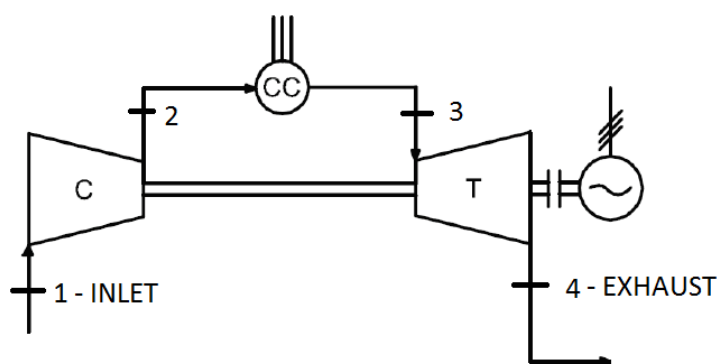


Figure 1.1: Schematic of a gas turbine. C is the compressor, CC is the combustion chamber and T is the turbine.

The gas turbines for power generation can be classified as follows:

- **Aeroderivatives gas turbines.** They are jet engines with power turbine and they are used in industry for power production in small scale (up to 50 MWe). As the name says, these engines have been adapted for power generation removing the by pass fans and adding a turbine for power production [5]. They are lighter weight variations of gas turbines and they are becoming popular for their fast response.
- **Heavy-duty gas turbines.** They are designed for power production in large scale (up to 250MWe) in industry and shipping. They are less flexible because of their slower response. Figure 1.2 shows an heavy duty gas turbine. The heavy-duty gas turbines have longer life and slightly higher thermal efficiencies

than aeroderivatives gas turbines [5].

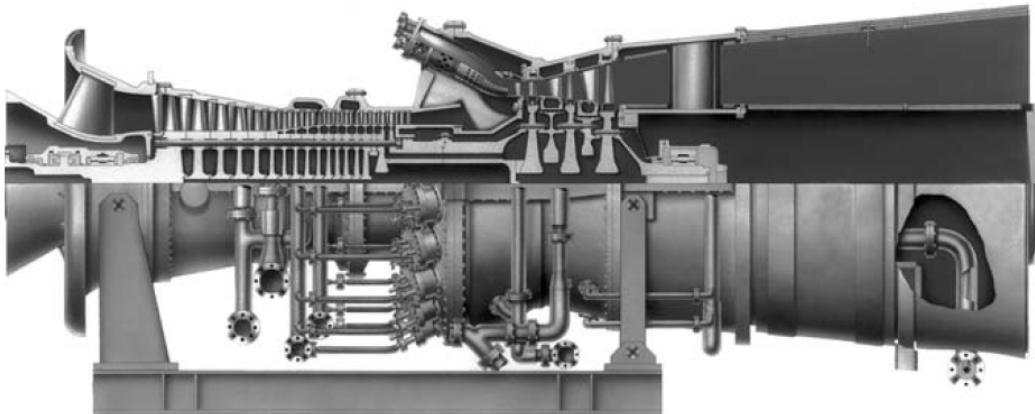


Figure 1.2: General electric gas turbine [5].

The gas turbine design efficiency usually varies from 20% to nearly 40% among heavy duty gas turbines for power generation on the market [20]. In order to improve the efficiency of power production, the heat from the exhaust gases of gas turbines is recovered. Sections 1.2 elaborates on the recovery of exhaust heat.

## 1.2. Recovery of exhaust heat from Gas Turbines

The gas turbine exhaust gases can be used to improve the efficiency of power generation both in combined cycles and in a combined heat and power plants. More detailed descriptions of such power stations are presented in chapters 2 and 3.

**Combined cycles** In a combined cycle (figure 1.3) the gas turbine exhaust gases enter the heat recovery steam generator (HRSG), a series of heat exchangers, where the gases transfer heat to the steam/water.



Figure 1.3: The picture shows the Combined Cycle Power Plant Encogen in The Netherlands.

The steam produced is delivered to a steam turbine and additional electricity is produced. The efficiency of power production increases because for the same amount of fuel injected in the combustion chamber

of gas turbine, more power is produced. Combined cycles can reach efficiencies of 55% and in the newest installations around 60 – 65% [28].

**Combined heat and power plants** In a combined heat and power plant the waste heat recovered in the HRSG is not converted into electricity but rather used for other applications (e.g. hot water for district heating heating, chemical industry etc.). Large offices and apartment buildings, hotels and shopping centers generate their own power and use the waste steam for building heat. By capturing the exhaust heat, the CHP plant uses heat that would otherwise escape through the exhaust duct in a conventional power plant, potentially reaching an efficiencies of 80%.

### 1.3. Development of energy markets

During the last 30 years, the electricity production from renewable sources has grown with an average annual rate of 2.2% accounting in 2014 for 22% of world power production [29]. Growth is especially high for wind, solar photovoltaic, biogas and biofuel (figure 1.4).

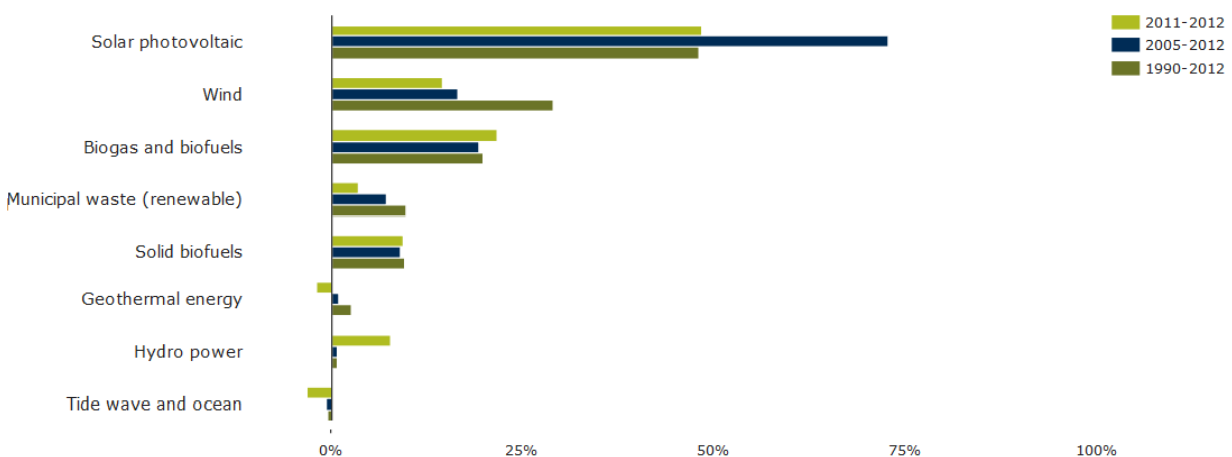


Figure 1.4: Average annual growth rates of renewable electricity in electricity consumption [22].

For instance, from 2005 to 2012 it was registered an average annual growth rate of 75% and 20% for wind and solar photovoltaic respectively. In the next years it is expected a further increase of the shares of renewables in the energy market. Figure 1.5 shows global share projections for the years 2030 to 2040 from three different scenarios [22]. These predictions refer to two moderate scenarios by the IEA (WEO “New Policies” and “450”), and a high-renewables scenario by Greenpeace. All the scenarios show a growth of the renewable energy for the electricity production.

Scenario	By Year	Electricity
<b>By 2030–2040</b>		
IEA <i>World Energy Outlook</i> (2012) “New Policies”	2035	31%
IEA <i>World Energy Outlook</i> (2012) “450”	2035	48%
Greenpeace (2012) <i>Energy [R]evolution</i>	2030	61%

Figure 1.5: Electricity shares of renewables by 2030-2040 [22].

However, power production from renewable sources has in general an intermittent character (especially wind and solar photovoltaic). For instance, the German wind power production (figure 1.6) shows the intermittent nature of this renewable source of energy.

Due to the increase of intermittent renewable sources of power on the grid, the requirements for balancing

### Actual production wind

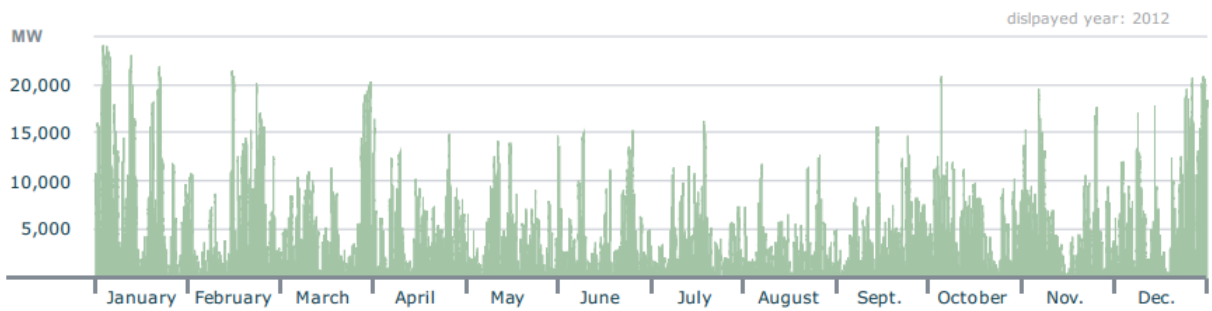


Figure 1.6: German wind power production in 2012 [29].

the grid become more important. This imposes challenges to the fossil power sources to provide more flexibility to keep the electricity grid stable.

The business case from power generation by a gas turbine has deteriorated during the last years due to the decrease in power price (caused by the increase of renewables) while the gas price stayed on a relatively high level. Up to now, many combined cycles and combined heat and power installations show little flexibility and their contribution to grid stability is limited. Especially during periods with a high contribution of renewables and a low power demand the operation of gas turbines using natural gas becomes very unattractive because of the low power prices. An option to overcome this problem is to operate gas turbines at deep part load during the period of excess of renewable power.

Summarizing, the European energy market became very volatile and it asks more flexibility to fossil power stations: if in the past gas turbines operated on a continuous basis (base load), nowadays there is the necessity for gas turbines to operate at part load.

## 1.4. Part load operation

Most of the current installations especially those older than 15-20 years, are mostly designed for base load operation. Part load operation is especially difficult for industrial CHP installations because they have to deliver to industrial steam consumers a constant and reliable heat supply. The gas turbine based technologies have relatively poor part-load performance [6]. For instance, figure 1.7 shows the power efficiency of a generic comined cycle drops at part load using traditional control strategies. The ideal situation would be if the power plants operated flexibly from 0%-100% with a high efficiency.

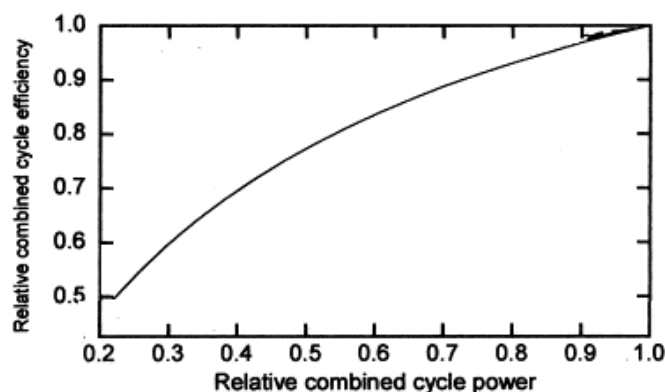


Figure 1.7: Relative combined cycle efficiency drop at part load [20].

**Flue Gas Recirculation** A solution to this problem is the use of Flue Gas Recirculation (FGR) for which flue gas from the chimney are recirculated to the gas turbine inlet. When recirculating the flue gases, the inlet

temperature of the gas turbine will rise resulting in a lower mass flow through the installation and lower power production. This aspect makes FGR a very prospective technology to be applied to gas turbine installations such as combined heat and power plants and combined cycles. Although FGR is a common technology for NO<sub>x</sub> reduction [9], only some indicative studies are available. These studies focus mostly on increasing CO<sub>2</sub> levels in exhaust gases [7, 13, 21, 23, 27] to facilitate CO<sub>2</sub> capture. FGR can improve the part load efficiency [30], however, it might lead to combustion stability issues [13] and increasing CO emissions [3, 12]. Flue Gas Recirculation has been studied before in the literature to increase CO<sub>2</sub> content in flue gases, but not to allow part load operation of power plants. The part load efficiency gain for FGR still needs to be defined.

## 1.5. Objective of the thesis

Gas turbine control techniques need to be researched to enable the use of FGR in existing CHP and CC installations. Furthermore, there is a lack of studies on the impact of FGR on the thermodynamic cycle, the gas turbines components, like compressor and cooling of the turbine. The objective of this master thesis is to:

- Identify and study in detail the gas turbine part load control techniques (including FGR).
- Identify the cycle limitations and the range of operationability and efficiency of each control.
- Apply the controls to a combined heat and power plant and to a combined cycle in order to quantify the part load efficiency gain when using FGR .
- Compare FGR with the other control techniques.
- Study the impact of FGR on the cooling of the turbine.

## 1.6. Outline of the report

The report is structured as follows:

- **Chapter 2.** It introduces a Brayton model developed to study the part load operation of gas turbines. Besides FGR, three other part load controls are proposed and the theoretical range of operationability of each control is discussed in detail.
- **Chapter 3.** The proposed control techniques of chapter 2 are applied to an industrial combined heat and power plant. In accordance with the control limitations the most efficient part load control combination is proposed.
- **Chapter 4.** Similarly to chapter 3, the proposed controls of chapter 2 are applied to an industrial combined cycle, the limitations of part load operation are discussed and the most efficient part load control combination is proposed.
- **Chapter 5.** It studies the impact of FGR on the cooling of the turbine. In order to do so, a model has been developed.
- **Chapter 6.** A case study takes into account the duct/blower (required to push the air to the gas turbine inlet) calculations and the limitation imposed by the maximum turbine blade temperature.



# 2

## Part load operation of gas turbines

This chapter introduces a model of a Brayton cycle used to predict the part load operation of gas turbines. In section 2.1, the thermodynamic relations for gas turbines are recalled. In industry, the gas turbine (GT) load is controlled by decreasing the firing temperature or compressor airflow (inlet guide vanes closure) as described in sections 2.3.1 and 2.3.2 respectively. In addition to these standard control techniques, air pre-heating control (AP) is introduced. In particular, AP can be achieved by recirculating to the GT inlet either the gas turbine exhaust flue gases (2.3.4) or the discharge compressor airflow (2.3.3). The off-design (OD) equations for each control technique are derived and written in dimensional form. The systems of equations are solved numerically in MATLAB and in section 2.3.5 the pros and cons of each part load technique are explained in detail.

### 2.1. Theoretical background

This section recalls basic information about the Brayton cycle for part load operation. Figure 2.1 shows the flow diagram of a gas turbine engine. The engine is composed of three components: the compressor, the combustion chamber and the turbine.

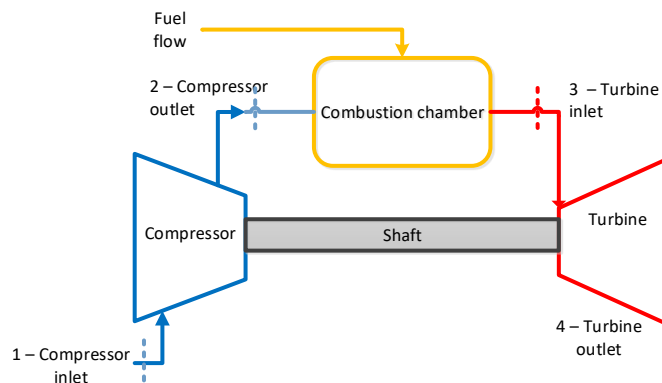


Figure 2.1: Brayton model - flow diagram.

**Model assumptions** For the model of this chapter the following assumptions were made [24]:

- The air behaves as in ideal gas.
- The air and flue gases heat capacities at constant pressure are constant and equal to  $c_p = 1 \frac{kJ}{kg K}$  and  $c_{pFG} = 1.1 \frac{kJ}{kg K}$  respectively.

- The air and flue gases isentropic exponents are constant and equal to  $k = 1.4$  and  $k_{FG} = 1.35$  respectively.
- No pressure losses in the combustion chamber ( $P_2 = P_3$ ).

The temperature - entropy (T-S) diagram in figure 2.2 shows the operation of the gas turbine at the design point.

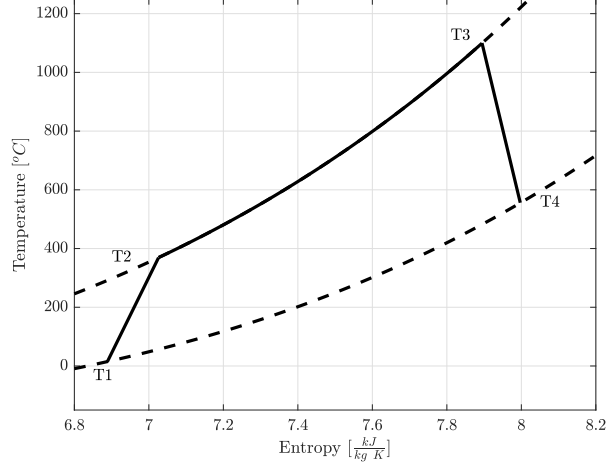


Figure 2.2: Brayton model: T-S diagram at the design point.

The airflow  $\dot{m}_a$  is sucked at ambient conditions by the compressor that increases the pressure and temperature of the fluid by reducing its volume. Ideally, the compression is isentropic but in reality, losses occur due to friction and heat losses ( $S_2 > S_1$ ) [24]. Therefore, an isentropic efficiency  $\eta_{isC}$  correlates the real compressor work with the ideal one. Assuming that the air behaves as an ideal gas, the compressor work is calculated as:

$$\dot{W}_c = \dot{m}_a c_p T_1 \frac{(\pi^{\frac{k-1}{k}} - 1)}{\eta_{isC}}, \quad (2.1)$$

where  $\pi$  is the GT pressure ratio,  $k$  is the isentropic exponent of the air ( $k = 1.4$ ) and  $c_p$  is air heat capacity at ambient pressure and temperature. The pressurized air heads to the combustion chamber where its temperature is increased to the turbine inlet temperature  $T_3$ . This is achieved by adding fuel  $\dot{m}_f$  to the combustion chamber and burning the air-fuel mixture. If  $T_3$  is the desired turbine inlet temperature and LHV is the lower heating value of the fuel, from the energy and mass balance at the combustor chamber, the fuel flow is calculated according to equation (2.2):

$$\dot{m}_f LHV + \dot{m}_a c_p T_2 = (\dot{m}_a + \dot{m}_f) c_{pFG} T_3. \quad (2.2)$$

The product  $\dot{m}_f LHV$  is also regarded as cycle fuel input (or fuel consumption)  $\dot{Q}_f$ .

Analogously to the compressor, an isentropic efficiency  $\eta_{isT}$  is defined for the turbine due to losses that occur during expansion ( $S_4 > S_3$ ):

$$\dot{W}_t = (\dot{m}_a + \dot{m}_f) c_{pFG} T_3 \left(1 - \pi^{\frac{1-k_{FG}}{k_{FG}}}\right) \eta_{isT}. \quad (2.3)$$

Finally, an important parameter that evaluates the gas turbine performance is the GT thermal efficiency  $\eta_{GT}$ . It is defined as the ratio of the useful output ( $\dot{W}_t - \dot{W}_c$ ) and the fuel input.

$$\eta_{GT} = \frac{\dot{W}_t - \dot{W}_c}{\dot{Q}_f}. \quad (2.4)$$

## 2.2. Off-design operation

Part-load refers to power production at levels below the full-load that may be achieved at a given ambient conditions with given installation parameters. Thus, part-load does not refer to a specific power level, but to a specific fraction of the possible full-load power achievable, all else being given. When part-loading the GT, the GT airflow, pressure ratio and fuel consumption change. The off-design (OD) airflow is imposed by the compressor (section 2.2.1), whereas the GT pressure ratio by the turbine (section 2.2.2). In this section, the derivation of the off-design equations to compute the GT airflow and pressure ratio for the part load modeling of the the Brayton cycle is addressed. In particular, the application of scale analysis to compressible fluids is used due to the complexity of the functional off – design relationships. Therefore, for the sake of simplicity, in this section scaling relations are derived. In this analysis, the compressor and turbine isentropic efficiencies are assumed constant.

### 2.2.1. Compressor airflow

The compressor airflow is a function of the compressor suction area  $A_1$ , the inlet axial component of the velocity  $V_{1ax}$  and the inlet density  $\rho_1$

$$\dot{m}_a = \rho_1 A_1 V_{1ax}. \quad (2.5)$$

If we express the density in terms of pressure and temperature using the ideal gas equation of state (EOS) :

$$\dot{m}_a = \frac{P_1}{RT_1} A_1 V_{1ax}. \quad (2.6)$$

When the gas turbine is operating at part load, the compressor airflow delivered changes. The compressor map is used to predict the OD airflow and isentropic efficiency. Figure 2.3 shows the compressor operation for a corrected speed line (constant compressor inlet temperature and shaft rotational speed) :

- When increasing the compressor airflow the axial velocity increases until it reaches its maximum value at the choked point, also called stonewall point. The velocity flow does not increase any further since the volumetric flow is limited by the cross-section area at the compressor inlet[18]. The operating point of the compressor is between the design point and the stonewall point.  
For the proposed model it is assumed the compressor operating line is vertical (stonewall assumption).
- In figure 2.3, the surge line represents a limit beyond which the compressor cannot work steadily. If the compressor has to work at conditions near the surge line, it can be detrimental for the engine. In particular, stall cause the compressor blades to vibrate and in the worst cases all the engine to tremble (surge) [26]. Vibrations reduces the useful life of the blades/engine. Hence, it is strongly recommended for the GT to operate below the surge margin conditions.

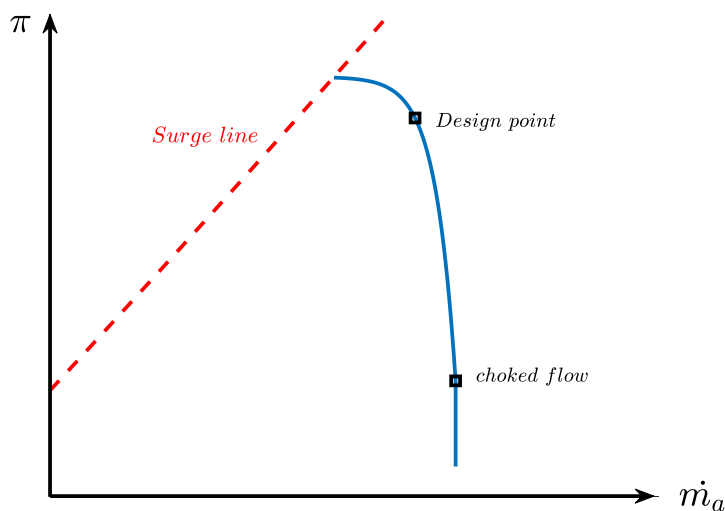


Figure 2.3: Compressor operation at part load (blue line) for a corrected speed line (constant compressor inlet temperature and shaft rotational speed).

### Variable inlet guide vanes

This section recalls basic information about the usage of inlet guide vanes in industry to vary the GT airflow. IGV are used to control the engine load when the power demand is lower than the average demand level. Inlet guide vanes in their application consist of wedge-shaped steel blades mounted around the inside circumference of a short length of inlet pipe as shown in figure 2.4[1].

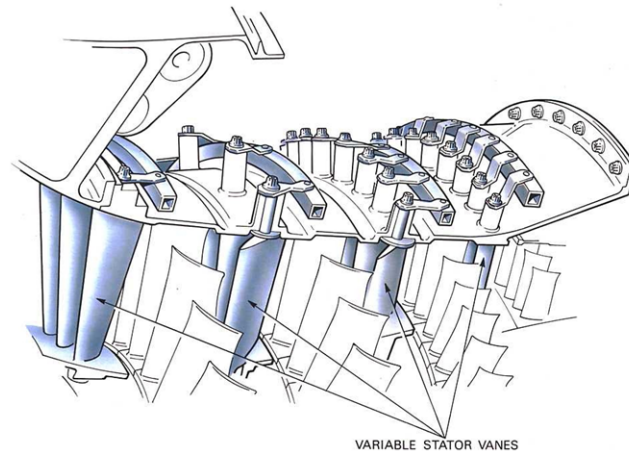


Figure 2.4: Variable inlet guide vanes.

They are turned in synchronization by a ring or yoke assembly on the outside of the pipe. Each vane is designed with an airfoil cross-section (similar to an airplane wing) to minimize air resistance when in its full open position (vanes positioned parallel to the air stream). The guide vanes are placed at the compressor inlet, that is before the compressor rotor.

In equation (2.5), the velocity can be expressed in terms of the inlet velocity angle  $\alpha_1$  (figure 2.5):

$$\dot{m}_a = \rho_1 A_1 V_1 \cos \alpha_1. \quad (2.7)$$

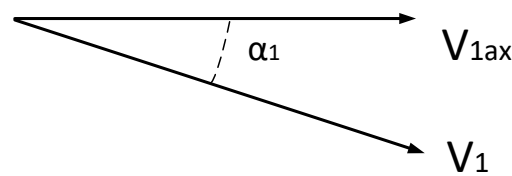


Figure 2.5: Absolute velocity vector at the GT inlet when the airflow is not purely axial ( $\alpha_1 > 0$ ).

According to figure 2.6, when closing the guide vanes ( $\alpha_{IGV} > 0$ ) the flow is deviated to a certain direction. For small variations of  $\alpha_{IGV}$ , the pressure losses across the guide vanes are assumed negligible. As a result, the air density  $\rho_1$  does not change when the engine is operating at part load. For the sake of simplicity the module of the absolute velocity is assumed to be constant. Hence, when closing the vanes, the GT airflow decreases because the axial component of the velocity diminishes from  $V_{1ax} = V_1 \cos(\alpha_1)$  to  $V_{1axOD} = V_1 \cos(\alpha_1 + \alpha_{IGV})$ .

As a result, the OD GT airflow is computed as follows:

$$\dot{m}_{aOD} = \dot{m}_a \frac{\cos(\alpha_{IGV} + \alpha_1)}{\cos(\alpha_1)}. \quad (2.8)$$

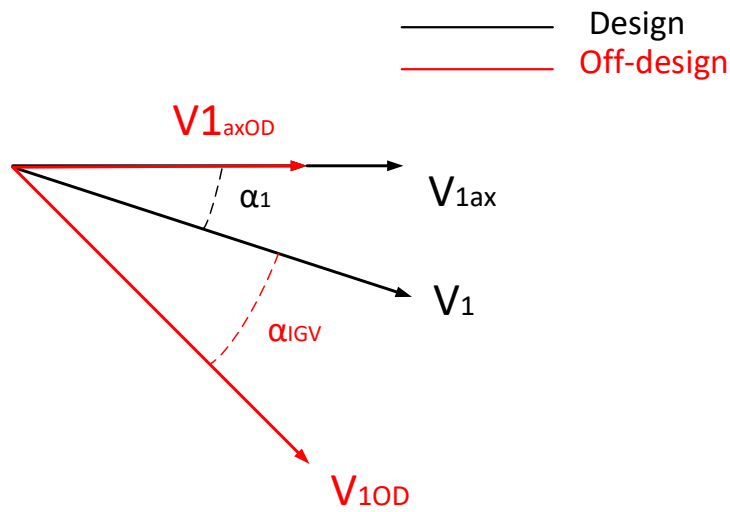


Figure 2.6: Velocity triangles at the outlet of the inlet guide vanes (compressor intake). The inlet guide vanes causes the absolute velocity vector to rotate by the angle  $\alpha_{IGV}$ .

where:

1.  $\alpha_{IGV} = 0$  at the design point.
2.  $\alpha_{IGV} > 0$  at part load.

#### **Air preheating control:**

The air preheating control increases the compressor inlet temperature in order to decrease the GT airflow, hence the GT power.

At part load, :

1.  $A_1$  is constant because the compressor geometry is fixed.
2. Any change of the compressor inlet temperature does not vary the compressor axial velocity  $v_{1ax}$  [11].
3. The inlet pressure  $P_1$  is constant.

Follows from equation (2.6) that when preheating the air the compressor airflow scales with compressor thermodynamic inlet temperature  $T_1$ .

$$\dot{m}_a \sim \frac{1}{T_1}. \quad (2.9)$$

$$\dot{m}_{aOD} = \dot{m}_a \frac{T_1}{T_{1OD}}. \quad (2.10)$$

### 2.2.2. GT pressure ratio

Figure 2.7 shows the turbine nozzle and rotor in a gas turbine.

When the flow enters the nozzle, its velocity is relatively low ( $v_3 \approx 50 \frac{m}{s}$ ) [5] and consequently increases the static temperature ( $T_3 \approx 1000K$ ) of approximately 1.25 K. Therefore, the velocity contribution in the total temperature expression can be neglected ( $T_3 \approx T_{03}$ ) [5].

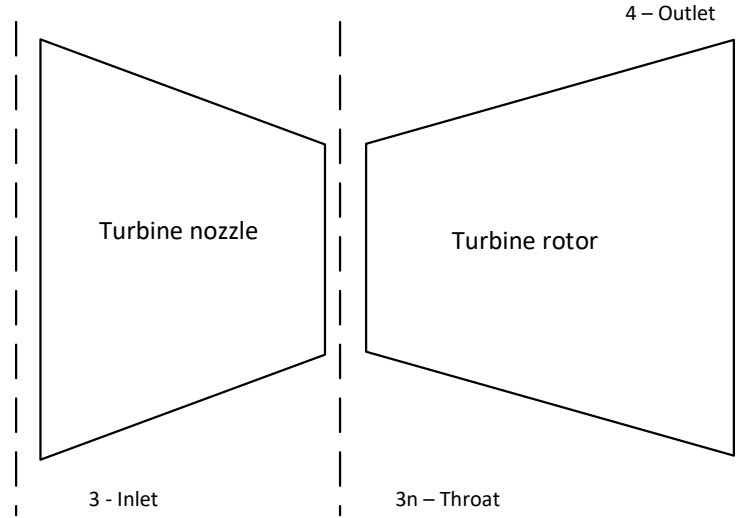


Figure 2.7: Turbine nozzle (stator) and rotor.

The following assumptions were made in order to compute the GT pressure ratio at part load:

1. The turbine flow is choked at the throat.
2. No losses occur in the turbine nozzle for simplification purposes.
3. The flow is expanded up to the atmospheric (static) pressure  $P_4$ .
4. The Mach number at the exhaust of the turbine is assumed constant ( $M_{a4} \approx 0.3$ ) [11].

At the choked throat (assumption 1):

$$\dot{m}_a + \dot{m}_f = \frac{P_{3n}}{RT_{3n}} A_{3n} c_{3n}, \quad (2.11)$$

where  $c_{3n}$  is the speed of sound at the temperature  $T_{3n}$ :

$$c_{3n} = \sqrt{kRT_{3n}}. \quad (2.12)$$

Following from assumption 2, the total temperature and pressure remain constant across the nozzle ( $T_{03} = T_{03n}$  and  $P_{03} = P_{03n}$  respectively).

From the definition of stagnation temperature and pressure at the choked nozzle [11]:

$$\begin{cases} T_{03n} = T_{3n} \left(1 + \frac{k-1}{2}\right) \\ P_{3n} = \frac{P_{03n}}{\left(1 + \frac{k-1}{2}\right)^{\frac{k}{k-1}}} = \frac{P_{03}}{\left(1 + \frac{k-1}{2}\right)^{\frac{k}{k-1}}} \end{cases} \quad (2.13)$$

Therefore:

$$T_3 \approx T_{03} = T_{03n} = T_{3n} \left(1 + \frac{k-1}{2}\right). \quad (2.14)$$

As a result, the static pressure and temperature at the throat are calculated as:

$$\begin{cases} T_{3n} \approx \frac{T_3}{(1 + \frac{k-1}{2})} \\ P_{3n} = \frac{P_{03}}{(1 + \frac{k-1}{2})^{\frac{k}{k-1}}} \end{cases} \quad (2.15)$$

Inserting equations (2.15) and (2.12) into equation (2.11):

$$\dot{m}_a + \dot{m}_f = \frac{P_{03}(1 + \frac{k-1}{2})}{(1 + \frac{k-1}{2})^{\frac{k}{k-1}} RT_3} A_{3n} \sqrt{kR \frac{T_3}{(1 + \frac{k-1}{2})}} \quad (2.16)$$

Rearranging equation (2.16):

$$\dot{m}_a + \dot{m}_f = \frac{P_{03}}{\sqrt{T_3}} \frac{A_{3n} \sqrt{\frac{k}{R}}}{(1 + \frac{k-1}{2})^{\frac{k+1}{2(k-1)}}} \quad (2.17)$$

When the engine is operating at part load the term  $C = \frac{A_{3n} \sqrt{\frac{k}{R}}}{(1 + \frac{k-1}{2})^{\frac{k+1}{2(k-1)}}}$  in equation (2.17) is constant whereas  $P_{03}$  and  $T_3$  differ from the design values:

$$\dot{m}_a + \dot{m}_f = \frac{P_{03}}{\sqrt{T_3}} C \quad (2.18)$$

As a result, the turbine flow will scale with:

$$\dot{m}_a + \dot{m}_f \sim \frac{P_{03}}{\sqrt{T_3}} \quad (2.19)$$

Finally, following from assumption 3 and 4, the total exhaust pressure  $P_{04}$  will be constant. Hence, the turbine flow scales with the (total) pressure ratio  $\Pi_{OD}$  and the square root of the turbine inlet temperature:

$$(\dot{m}_a + \dot{m}_f)_{OD} = (\dot{m}_a + \dot{m}_f) \frac{\Pi_{OD}}{\Pi} \sqrt{\frac{T_3}{T_{3OD}}} \quad (2.20)$$

Equation (2.20) correlates the change in GT pressure ratio and TIT with the change in turbine flow.

## 2.3. Engine control theory

Vendors use several techniques to part-load gas turbines: decreasing firing temperature, decreasing inlet airflow (inlet guide vane closure), and combining these methods. When controlling the turbine inlet temperature, the turbine power is being directly controlled by changing the fuel flow (section 2.3.1). The air pre-heating control aims to increase the inlet temperature and consequently to diminish the airflow. The compressor inlet temperature is increased by recirculating the compressor airflow or by recirculating the flue gases to the compressor inlet as described in sections 2.3.3 and 2.3.4 respectively. Another way of controlling the compressor airflow is by using the inlet guide vanes control as shown in section 2.3.2. For each part load technique, next to the equations derived in section 2.2, a system of non-linear equations is defined in the appendix and solved in MATLAB. For simplification, the turbine and compressor isentropic efficiencies are assumed constant for all the control techniques. In this section the results of the simulations are also presented in the T-S diagram in order to visualize graphically how the shape of the Brayton cycle changes at part load. The results of model are validated with THERMOFLEX. THERMOFLEX is a modular program with graphical interface for engineering thermodynamic simulations. The use of the Engineering Design (ED) approach in THERMOFLEX is not intended for creating newly-designed gas turbines, but is rather to employ a known engine in industry for the design and/or OD simulations. The OD computation considers the energy balance, heat transfer, and flow characteristics as well as interactions between the various components and the control system. The gas turbine of General Electric GE 6531B is selected for the validation.

### 2.3.1. Turbine inlet temperature control

The TIT is decreased (or increased) by directly controlling the fuel flow injected in the combustion chamber. In accordance with equation (2.6) the GT airflow depends on the compressor geometry ( $A_1$ ) and thermodynamic inlet conditions. For the stonewall assumption of section 2.5:

$$\dot{m}_{aOD} = \dot{m}_a. \quad (2.21)$$

The turbine flow is the sum of the compressor airflow and fuel flow. Given that  $\dot{m}_{fOD} \ll \dot{m}_{aOD}$  the turbine flow can be considered constant. Hence, in equation (2.20) the change in GT pressure ratio just depends on the turbine inlet temperature:

$$\Pi_{OD} = \Pi \sqrt{\frac{T_{3OD}}{T_3}}. \quad (2.22)$$

Figure 2.8 shows the change in GT pressure ratio when the TIT is decreased.

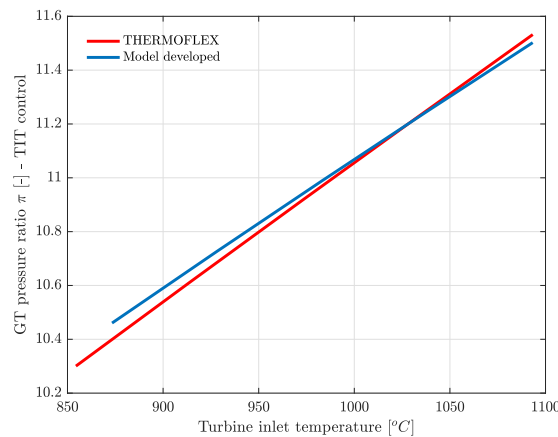


Figure 2.8: Model validation: GT pressure ratio versus TIT for THERMOFLEX (red line) and the developed model (blue line). The error is less than 0.6%.

The results of the simulation presented in the T-S diagram (figure 2.9) show that when decreasing the turbine inlet temperature from  $T_3$  to  $T_{3OD}$ , the engine load decreases.

The GT airflow stays constant whilst the GT specific work decreases because:

- the isobars diverge on temperature [14].

- The GT pressure ratio  $\pi_{OD}$  diminishes. As a matter of fact, if the GT pressure ratio did not decrease the turbine temperature drop would be higher.

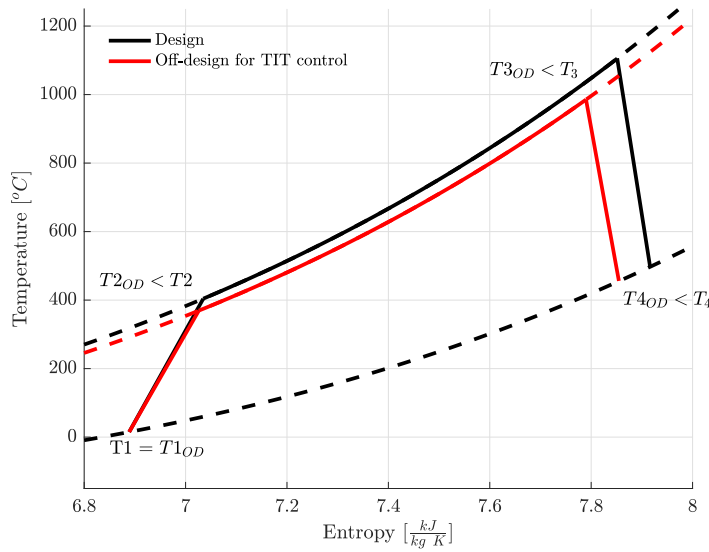


Figure 2.9: T-S diagram of Brayton cycle for TIT control: the cycle in black defines the Brayton cycle at the design conditions whereas the other in red represents the cycle when the GT load is 70% and  $T_{3OD} = 980^\circ\text{C}$ .

### 2.3.2. Inlet guide vanes control

Part load can be successfully achieved by closing the guide vanes. In section 2.2.1, equation (2.8) expresses the OD compressor airflow ( $\dot{m}_{aOD}$ ) as a function of the IGV angle of attack  $\alpha_{IGV}$ .

$$\dot{m}_{aOD} = \dot{m}_a \frac{\cos(\alpha_{IGV} + \alpha_1)}{\cos(\alpha_1)}. \tag{2.8}$$

When closing the guide vanes ( $\alpha_{IGV} > 0$ ) the GT power decreases (figure 2.11a) because less airflow enters the gas turbine (figure 2.11b) and the GT pressure ratio diminishes (figure 2.10).

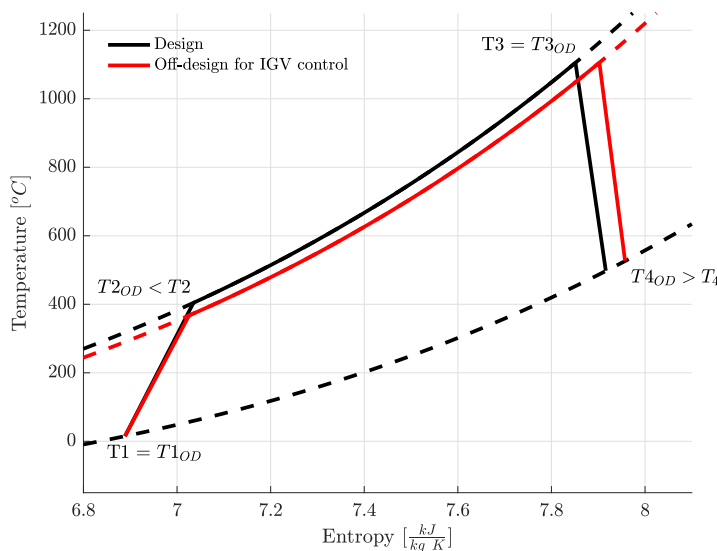


Figure 2.10: T-S diagram of Brayton cycle for IGV control: the cycle in black defines the Brayton cycle at the design point whereas the other in red represents the cycle when the GT load is 80% and  $\alpha_{IGV} = 12.5^\circ$ .

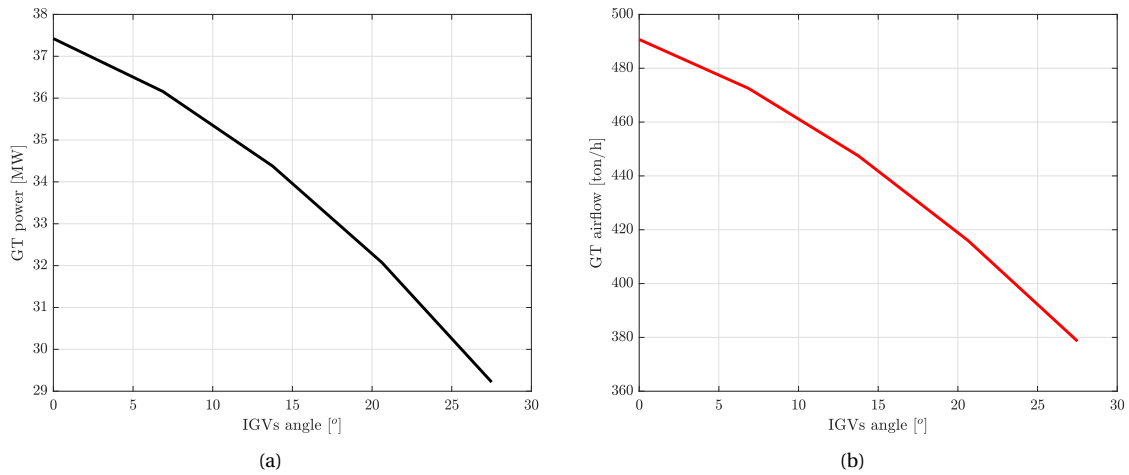


Figure 2.11: Brayton model. The GT power (a) and compressor airflow (b) decrease when closing the inlet guide vanes .

**Minimum surge margin** Figure 2.12 shows the variation of GT pressure ratio when diminishing the compressor airflow by closing the guide vanes.

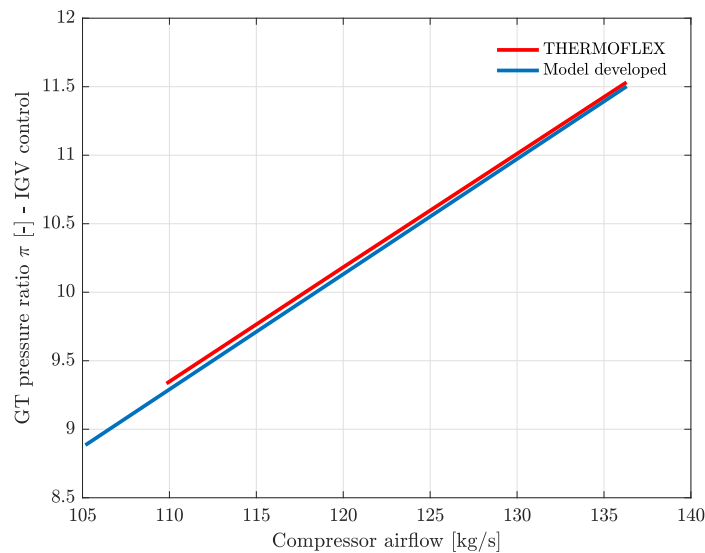


Figure 2.12: Model validation: GT pressure ratio versus GT airflow for THERMOFLEX (red line) and the developed model (blue line). The error is less than 0.1%.

In reality the guide vanes can be closed down to a certain limit (usually down to 80% of cycle load) beyond which surge and stall will occur. In the compressor map of figure 2.13 the black square represents the compressor design point whereas the green line the part load operation for IGV control. The vanes can close down to a minimum airflow because a minimum surge margin has to be maintained.

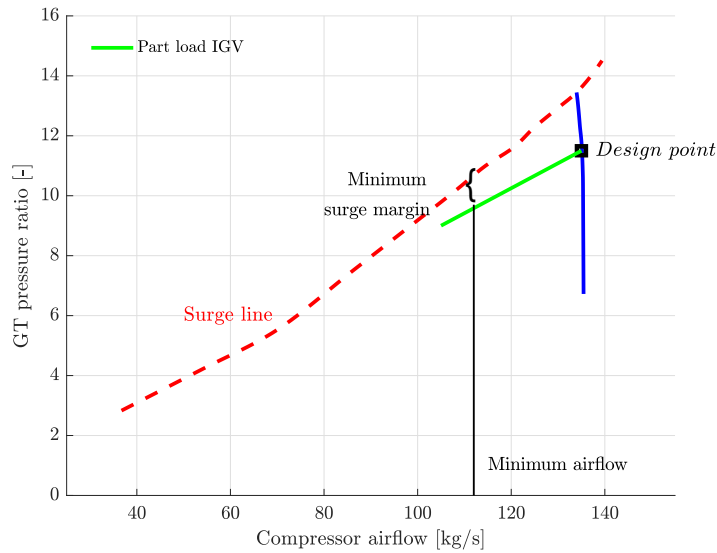


Figure 2.13: Compressor map - IGV control. The blue line is the design corrected iso-speed line (constant compressor inlet temperature and shaft rotational speed). The map shows the minimum value of inlet airflow when closing the inlet guide vanes. In reality, the surge line slightly shifts to the left improving the surge margin [26]. The worst case scenario is considered and the surge margin line is assumed to not shift.

### 2.3.3. Compressor airflow recirculation (CAR)

One possible way of increasing the compressor inlet temperature is recirculating the compressor discharge air to the compressor inlet as shown in figure 2.14. The recirculated flow is expanded in the butterfly valve and mixed with atmospheric air. Therefore, the compressor inlet temperature rises because the temperature of the recirculated airflow ( $\approx 550K$ ) is higher than the atmospheric temperature ( $\approx 293K$ ). Defining  $x_{CAR}$  as the fraction of recirculated airflow,  $m_{aOD}(1 - x_{CAR})$  is the flow that can produce useful work in the turbine.

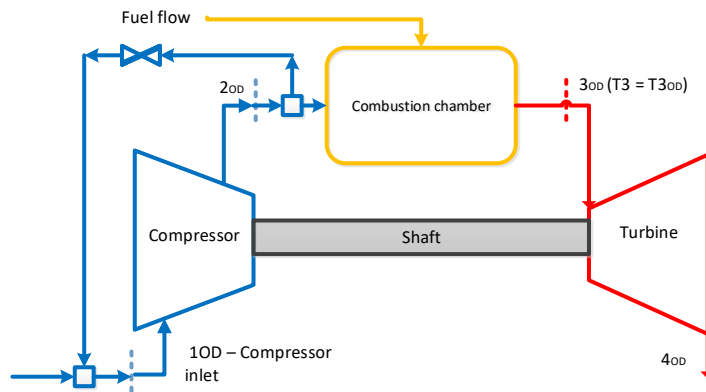


Figure 2.14: Simple Brayton model: flow diagram for CAR.

The results of the simulation are displayed in the T-s diagram of figure 2.15. The cycle in red represents the system at part load. In particular, the compressor inlet temperature rises ( $T_{1OD} > T_1$ ) and less amount of fuel is required to heat up the gases up to the turbine inlet temperature  $T_{3OD} = T_3$ .

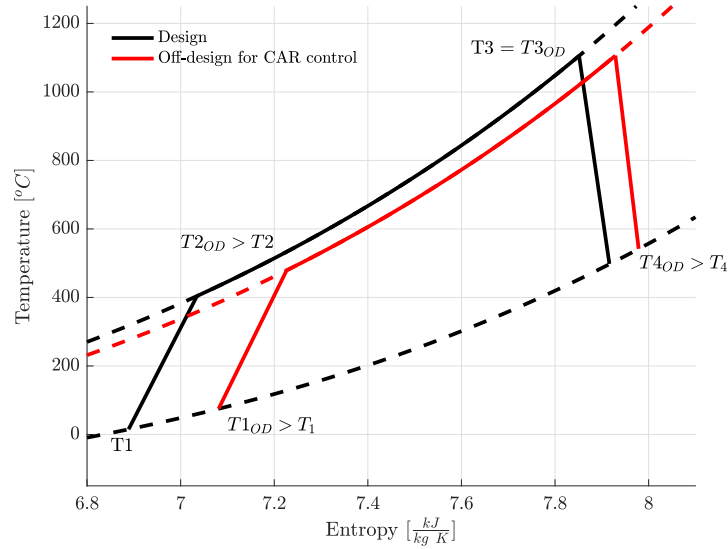


Figure 2.15: T-S diagram of Brayton cycle for CAR control: the cycle in black defines the Brayton cycle at the design point whereas the other one in red represents the cycle when the engine load is 64% and  $T_{1OD} = 45^\circ\text{C}$

The charts in figure 2.16 show how the GT power decreases when recirculating the compressor airflow to the GT inlet.

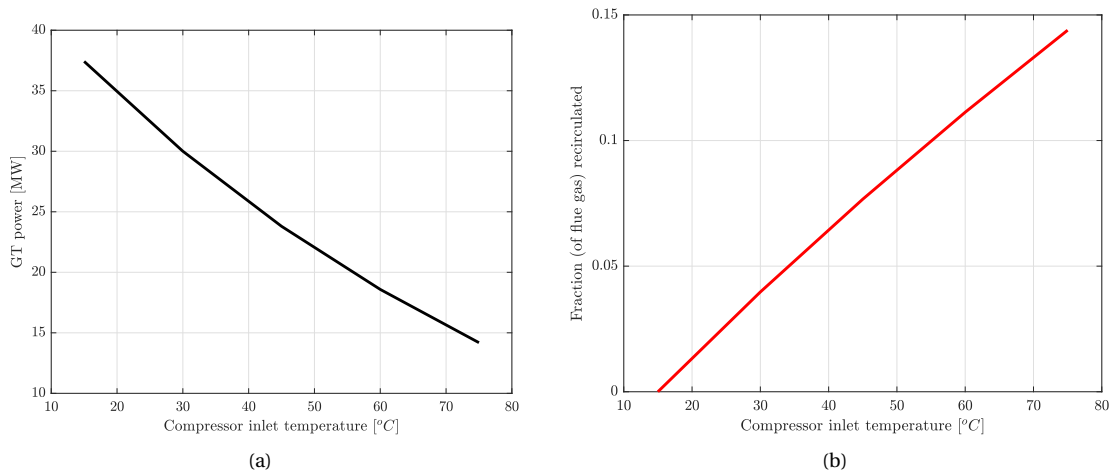


Figure 2.16: Simple Brayton model for CAR control: Compressor inlet temperature vs GT power and fraction recirculated. The black curve (a) shows how the output power decreases when the compressor inlet temperature rises whereas the red curve (b) calculates the required fraction (of airflow) recirculated. For instance, if 10 % of the airflow is recirculated, the compressor inlet temperature will rise up to  $55^\circ\text{C}$  for a GT power of approximately 20 MW.

Summarizing, in CAR control less output power is produced because:

1. less air is sucked by the compressor ( $\dot{m}_{aOD} < \dot{m}_a$ ) according to equation (2.10) .
2.  $\dot{m}_{aOD}(1 - x_{CAR})$  is the flow that can produce useful work in the turbine.

**Minimum surge margin** Unlike the IGV control, in accordance with figure 2.17 air preheating causes the GT pressure ratio and airflow to decrease because the compressor inlet temperature rises.

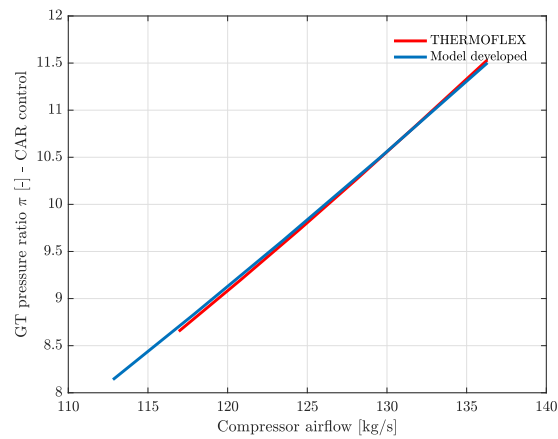


Figure 2.17: Model validation: compressor discharge pressure versus GT airflow for THERMOFLEX (red line) and the developed model (blue line). The error is less than 0.1%.

In the compressor map of figure 2.18 the black line represents the part load operation for CAR control. When increasing the compressor inlet temperature the operating point is distant from the surge line. Therefore, the compressor operates steadily at part load.

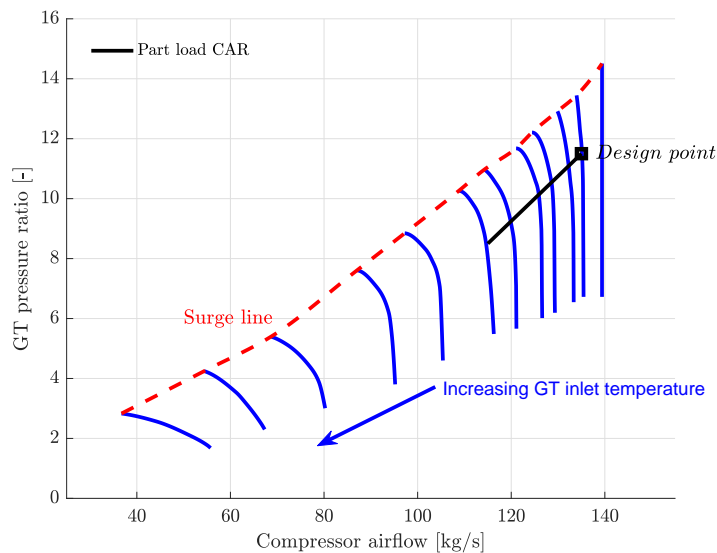


Figure 2.18: Compressor map - CAR control. The blue lines represent the operation of the compressor at different iso-corrected speeds (constant inlet temperature and shaft rotational speed). When recirculating the compressor airflow, the surge margin is respected.

### 2.3.4. Flue gases recirculation (FGR)

In FGR control, the compressor inlet temperature is increased by recirculating the exhaust gases to the compressor inlet. In such a configuration, a controlled splitter divides the flue gases stream into two main flows as exhibited in figure 2.19. At the design no flow is recirculated, thus all the exhaust gases heads to the stack. The FGR control directly varies the percentage of flow recirculated. Mixing a fraction of exhaust gases with the airflow (at ambient temperature) causes the compressor inlet temperature to rise.

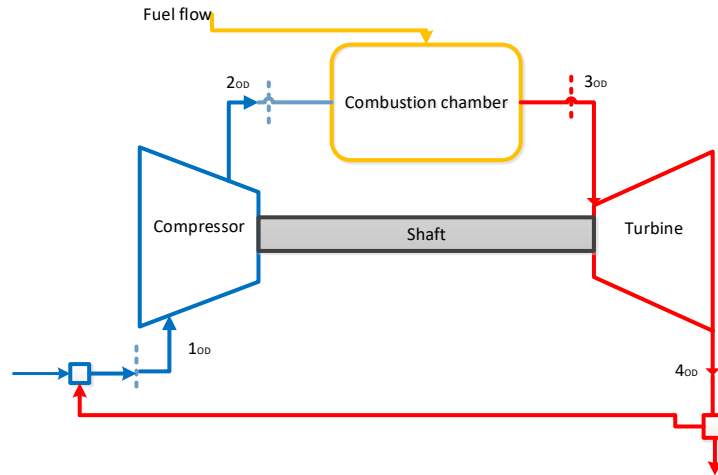


Figure 2.19: Simple Brayton model: flow diagram for FGR.

In the T-S diagram of figure 2.20, less amount of fuel is required to heat up the gases up to the (constant) turbine inlet temperature. The pressure ratio decreases due to the lower turbine flow.

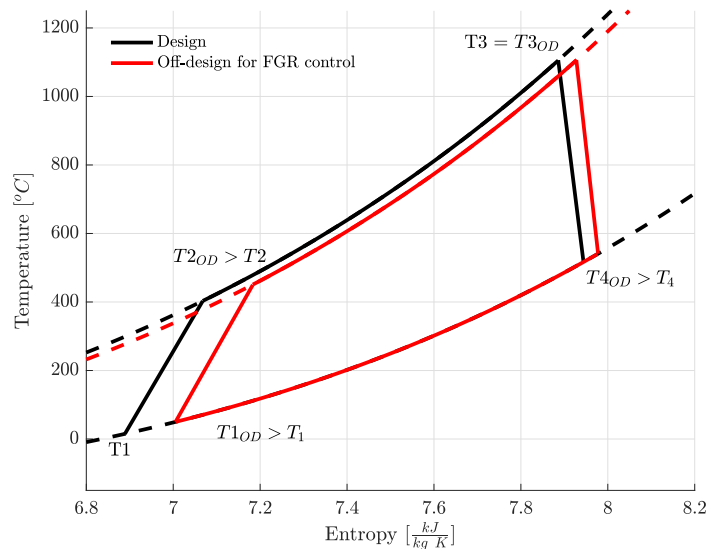


Figure 2.20: T-S diagram of Brayton cycle for FGR control: the cycle in black defines the Brayton cycle at the design point whereas the other one in red represents the cycle when the engine load is 85.3% and  $T_{1OD} = 35^{\circ}\text{C}$

Finally, figure 2.21 displays in detail how the GT power diminishes at part load when recirculating the exhaust gases to the GT inlet.

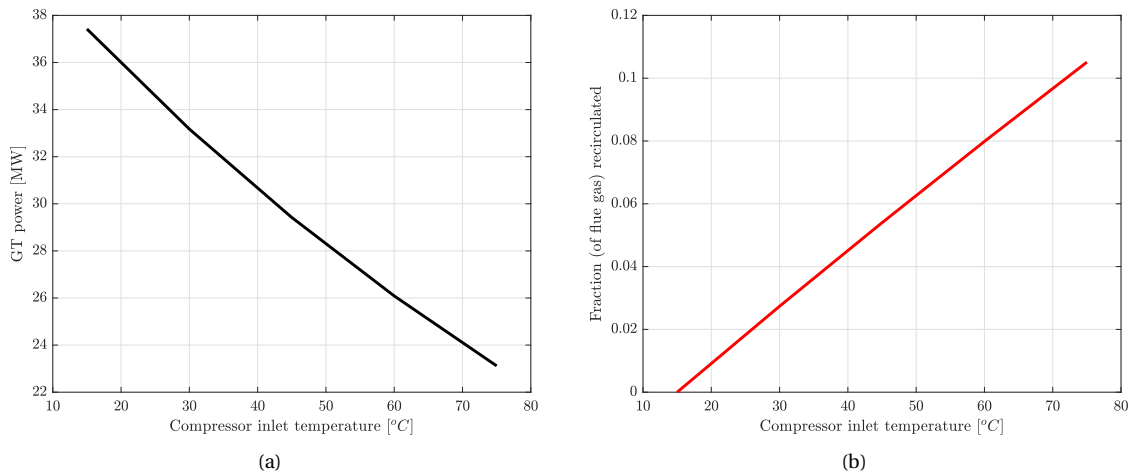


Figure 2.21: Simple Brayton model for FGR control: Compressor inlet temperature vs GT power and fraction (of flue gases) recirculated. The compressor inlet temperature rises because a fraction of the flue gases is recirculated (b) causing the output power to reduce (a). For instance, if 6% of the flue gases are recirculated, the compressor inlet temperature will rise up to 50°C for a cycle output power of approximately 26 MW.

When mixing the exhaust gases with ambient air, the molar composition of the compressor mass flow changes since the flue gases are rich in  $CO_2$ ,  $NO_x$  etc. Therefore, the oxygen concentration at the GT inlet diminishes. One of the major disadvantage of the FGR technique is the minimum molar concentration of  $O_2$  for maintaining the required level of flame stability, unburned hydrocarbons (UHC) and CO emissions. Figure 2.22 shows that when the percentage of oxygen decreases below 17% the mixture enters the non combustible zone if the combustion temperature is not high enough. This might be an issue for the combustion. However, the part load operational range can be increased using air injection or hydrogen injection [31]. It was found that for existing FGR cycles beyond the oxygen molar concentration of 14.5% at the GT inlet, the combustion becomes unstable [4, 10, 13].

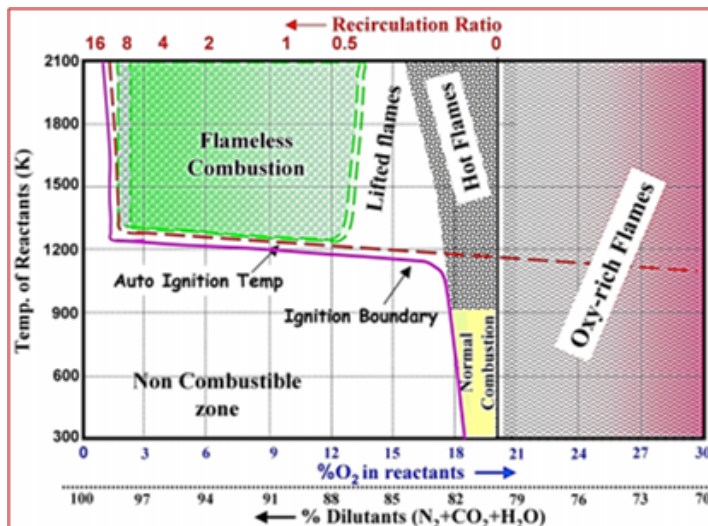


Figure 2.22: Simple Brayton model: combustion.

Furthermore, another solution to the oxygen concentration problem could be the following. Instead of mixing the flue gases with ambient air, an heat exchanger can be used to transfer heat from the hot gases to the compressor airflow. The modeling equations would be the same with the only difference that the GT airflow molar composition would not change. However, this solution might be expensive.

**Minimum surge margin** Similarly to CAR control, the GT pressure ratio and airflow diminish when recirculating the exhaust gases because the GT inlet temperature increases (figure 2.23).

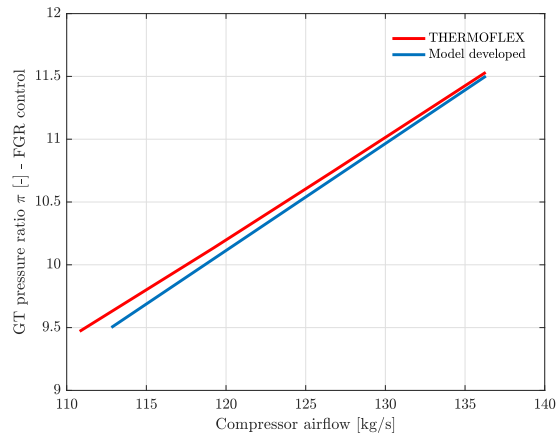


Figure 2.23: Model developed: compressor discharge pressure versus GT airflow for THERMOFLEX (red line) and the developed model (blue line). The error is less than 0.7%.

The FGR control causes the compressor inlet temperature to rise significantly. In figure 2.24, when the GT power is 25 MW (70 % of the design load) the compressor inlet temperature is  $65^{\circ}\text{C}$  and  $41^{\circ}\text{C}$  for FGR and CAR respectively.

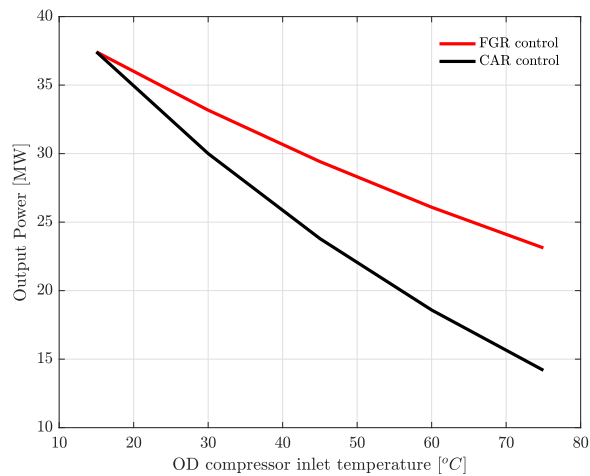


Figure 2.24: Simple Brayton model: compressor inlet temperature vs GT power for CAR and FGR controls.

For the same OD compressor airflow, the GT pressure ratio is higher for FGR control with respect to CAR control, since in CAR a fraction of airflow is recirculated to the compressor inlet and thus less mass flow enters the turbine. Figure 2.25 shows that when recirculating the flue gases to the gas turbine inlet, the operating line (in black) is far from the surge line. Therefore, when recirculating the exhaust gases there is no risk of stall/surge.

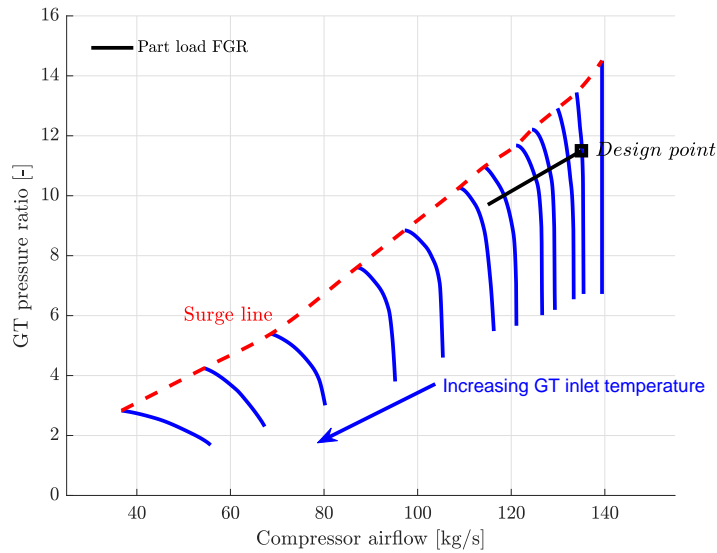


Figure 2.25: Compressor map - FGR control. The blue lines represent the operation of the compressor at different iso-corrected speeds (constant inlet temperature and shaft rotational speed). When recirculating the flue gases, the surge margin is respected.

### 2.3.5. Part load efficiency

Figure 2.26 shows that the GT efficiency drops when the gas turbine is operating at part load. When *decreasing the TIT*, the output power is reduced since isobars diverge on temperature (section 2.3.1). When *recirculating the compressor airflow (CAR control)*, a valve has to be placed to expand the flow. Therefore, a significant amount of energy is lost because the airflow recirculated does not produce useful work in the turbine.

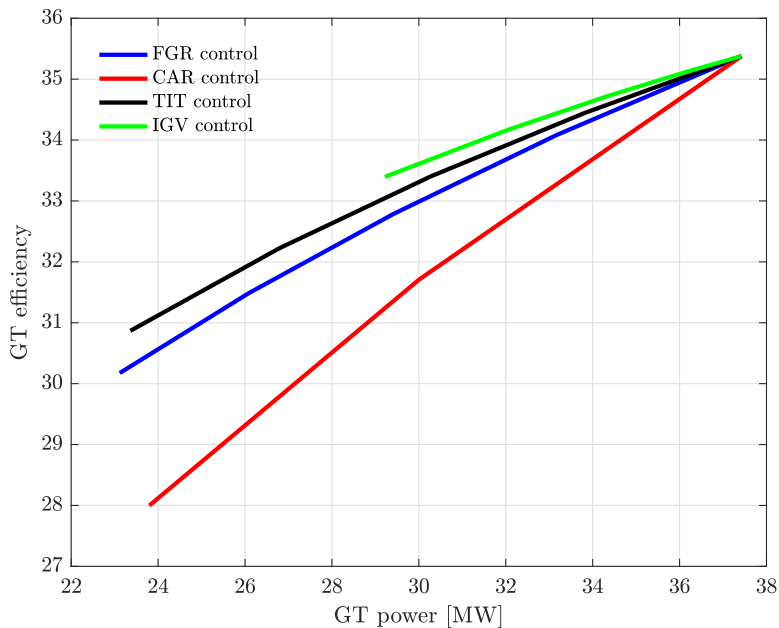


Figure 2.26: Brayton model: GT efficiency vs GT power for all the part load techniques.

On the other hand, in *FGR control* no valve is needed because the flue gases are expanded up to the atmospheric pressure and moreover, unlikely for CAR control, all the compressor airflow can produce useful work in the turbine. This is the reason for why FGR control is more efficient than CAR control. When *closing the inlet guide vanes*, the compressor airflow diminishes because the (axial) inlet velocity decreases. The GT efficiency is strictly related to the OD gas turbine pressure ratio. At part load, the GT pressure ratio decreases either because less mass flow goes to the turbine (IGV & air pre-heating controls) or because the TIT is lower (TIT control). The IGV control is found to be the most efficient control technique for part load operation for

the Brayton cycle.

## **2.4. Conclusions**

The part-load operation equations for the thermodynamic modeling of a GT have been derived and four control techniques were studied in detail: TIT, IGV, CAR and FGR control. The model developed reproduces the OD operation of the GE6531B with an accuracy higher than 99 %. The risk of compressor stalling/surging has been investigated. In particular, when closing the IGVs, the compressor airflow can be decreased down to a minimum airflow, whereas in air pre-heating control (FGR and CAR), there is no risk of stall/surge. IGV resulted to be more efficient, followed by TIT, FGR and CAR control. The further step in chapter 3 and 4 is to apply the proposed controls to a combined heat&power plant and combined cycle respectively.

# 3

## Part load operation of a combined heat and power plant

Chapter 3 deals with the thermodynamic modeling of a combined heat and power plant using THERMOFLEX. The goal is to predict the thermal efficiency at part load. The design of the CHP plant is presented in section 3.1. In section 3.2, OD simulations are run for the different part load controls of chapter 2. The system energy balance is derived and the results are explained through the temperature-heat (T-Q) diagram of the HRSG. In section 3.2.5, the optimum part load technique combination to achieve deep part load operation is proposed and the results are briefly summarized in section 3.3.

### 3.1. Modeling of the CHP plant

Figure 3.1 shows the flow diagram of a generic combined heat and power plant. When the exhaust gases exit the gas turbine they are heated up in the supplementary firing unit (SFU) before entering the heat recovery steam generator. The HRSG is made of three heat exchangers: the economizer, evaporator and super-heater. In the modeled CHP plant in THERMOFLEX the water pressure is increased by a water pump up to the evaporation pressure ( $P_{ev}$ ) of 23.5 bars and heated up to  $285^{\circ}C$  in the HRSG.

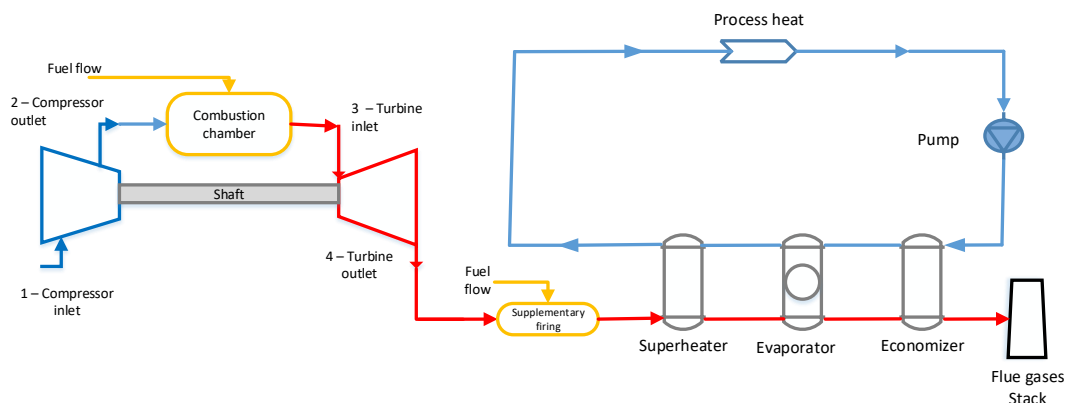


Figure 3.1: CHP plant flow diagram.

The study of the CHP plant is based on the General Electric turbine model nr. GE 6531B. Its design characteristics are shown in table 3.1. Finally, table 3.2 exhibits the HRSG design values.

Manufacturer & model	Shafts	RPM	$\pi$	TTT [ $^{\circ}C$ ]	T4 [ $^{\circ}C$ ]	Airflow [ton/h]	Shaft Power [kWe]	LHV efficiency [-]	Price [MM\$]
GE 6531B	1	5100	11.7	1104	539	496	38270	31.6	14.8

Table 3.1: Selected gas turbine for the CHP plant.

Parameter	Value	Unit	Description
$T_{in}$	80	[ $^{\circ}C$ ]	Water temperature at the inlet of the HRSG / process return temperature
$P_{ev}$	23.5	[bar]	Water evaporation pressure
$T_{out}$	285	[ $^{\circ}C$ ]	Water temperature at the outlet of the HRSG / process delivery temperature
$m_w$	22	[kg/s]	Water/steam flow in the HRSG
$T_{stack}$	141	[ $^{\circ}C$ ]	Flue gases temperature at the outlet of the HRSG / stack temperature
$T_5$	552.6	[ $^{\circ}C$ ]	Flue gases temperature at the inlet of the HRSG / outlet of the SFU
$Q_{SFU}$	2.485	[MW]	Heat added in the Supplementary firing unit (based on LHV)
$Q_{HRSG}$	65	[MW]	Process heat

Table 3.2: CHP plant - HRSG design values

The HRSG recovers 65 MW (figure 3.2) of heat from the flue gases temperature by decreasing the temperature from  $T_5 = 551.6^{\circ}C$  to  $T_{stack} = 141^{\circ}C$ . The steam produced is useful for any process application (district heating, chemical applications, power production, ect.).

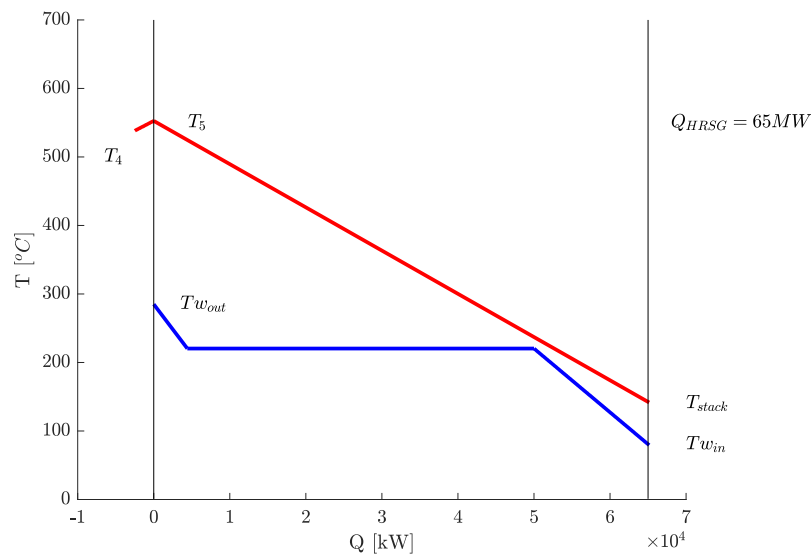


Figure 3.2: CHP plant: T-Q diagram at the design conditions. Negative values of Q express the amount of heat required in the SFU to keep the process heat  $Q_{HRSG}$  constant.

**System energy balance** If we imagine the CHP system as a whole we can write the system energy balance. Figure 3.3 represents the CHP plant as a black box. The system net fuel input ( $Q_f = \dot{m}_f LHV$ ) which is the sum of the fuel required in the combustion chamber and in the SFU is converted into electrical power ( $P_{el}$ ) in the GT and in process heat ( $Q_{HRSG}$ ) in the heat recovery steam generator. The streams of airflow/flue gases and water/steam are the two process flows:

$$\dot{m}_f LHV + \dot{m}_a h_{amb} + \dot{m}_w h_{in} = P_{el} + (\dot{m}_a + \dot{m}_f) h_{stack} + \dot{m}_w h_{out}. \quad (3.1)$$

Rearranging equation (3.1) and considering that  $Q_{HRSG} = \dot{m}_w (h_{out} - h_{in})$ :

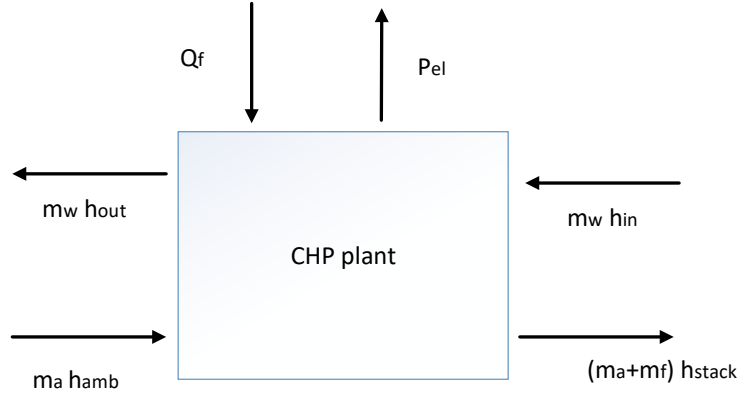


Figure 3.3: CHP plant: energy balance.

$$\dot{m}_f (LHV - h_{stack}) = P_{el} + Q_{HRSG} + \dot{m}_a (h_{stack} - h_{amb}). \quad (3.2)$$

The term  $h_{stack}$  can be considered negligible compared to the LHV of the fuel ( $\frac{h_{stack}}{LHV} \approx 0.31\%$ ). Therefore, the energy equation becomes:

$$\dot{m}_f LHV = P_{el} + Q_{HRSG} + \dot{m}_a (h_{stack} - h_{amb}). \quad (3.3)$$

Finally, the fuel input can be computed as:

$$Q_f = P_{el} + Q_{HRSG} + \dot{m}_a (h_{stack} - h_{amb}). \quad (3.4)$$

Equation (3.4) clearly shows the net fuel input is converted into electrical energy and into process heat. The remaining part  $Q_{stack} = \dot{m}_a (h_{stack} - h_{amb})$  is regarded as stack losses because it is not converted into electricity or into useful process heat:

$$Q_f = P_{el} + Q_{HRSG} + Q_{stack}. \quad (3.5)$$

### 3.2. Part load operation

At part load, the electrical power of the CHP plant is diminished by a  $\Delta P_{el} = P_{elOD} - P_{el} < 0$ . Equation (3.5) is used to compute the change in net fuel input at part load  $\Delta Q_f$ :

$$\Delta Q_f = \Delta P_{el} + \Delta Q_{HRSG} + \Delta Q_{stack}, \quad (3.6)$$

Because the purpose of this chapter is to keep the process heat delivered constant, follows that  $\Delta Q_{HRSG} = 0$ . Therefore:

$$\Delta Q_f = \Delta P_{el} + \Delta Q_{stack}. \quad (3.7)$$

where:

$$\Delta Q_{stack} = \Delta(\dot{m}_a (h_{stack} - h_{amb})). \quad (3.8)$$

In order to evaluate the performance of the combined heat&power plant the CHP efficiency is defined as follows:

$$\eta_{CHP} = \frac{P_{el} + Q_{HRSG}}{Q_f}. \quad (3.9)$$

At part load, the electrical power of the CHP plant is diminished by a  $\Delta P_{el} = P_{elOD} - P_{el} < 0$ :

$$\eta_{CHP_{OD}} = \frac{\Delta P_{el} + P_{el} + Q_{HRSG}}{\Delta Q_f + Q_f}. \quad (3.10)$$

Inserting equation (3.7) into equation (3.10):

$$\eta_{CHP_{OD}} = \frac{\Delta P_{el} + P_{el} + Q_{HRSG}}{\Delta P_{el} + \Delta Q_{stack} + Q_f}. \quad (3.11)$$

When comparing the part load efficiency of different controls in equation 3.11 the terms  $Q_{HRSG}$ ,  $\Delta P_{el}$ ,  $P_{el}$  and  $Q_f$  are constant for obvious reasons. Therefore, depending on the  $\Delta Q_{stack}$  of each control one part load technique will be more efficient than the other.

In the next sections the stack losses for each control are visualized in the T-Q diagram of the HRSG and in section 3.2.5 the part load efficiency of the combined heat & power plant is presented. Chapter 3 does not deal with the prediction of the emissions for the combustion chamber operating in OD mode. THERMOFLEX does not predict the emissions of the GT. As previously discussed in chapter 2, existing studies show combustion problems arise for FGR control since we might enter the non combustible zone. Therefore, when recirculating the exhaust gases, OD simulations are run down to the oxygen concentration of 14.5% in order to guarantee an efficient and stable combustion.

### 3.2.1. TIT control

The T-Q diagram of figure 3.4 shows the OD operation of the HRSG: because of the lower GT exhaust temperature ( $T_{4OD} < T_4$ ) the heat required in the SFU increases significantly in order to keep the process heat constant. Moreover, given that the stack mass flow do not change at part load (stonewall assumption of chapter 2) the stack temperature remains almost constant ( $T_{stackOD} \approx T_{stack}$ ). As a consequence, the delta stack losses  $\Delta Q_{stack} = \Delta(\dot{m}_a (h_{stack} - h_{amb}))$  are approximately equal to zero. This implies that  $\Delta Q_f \approx \Delta P_{el}$ . For instance, if the GT power is decreased by 5MW, as a consequence the CHP net fuel rate  $Q_f$  will diminish by 5 MW.

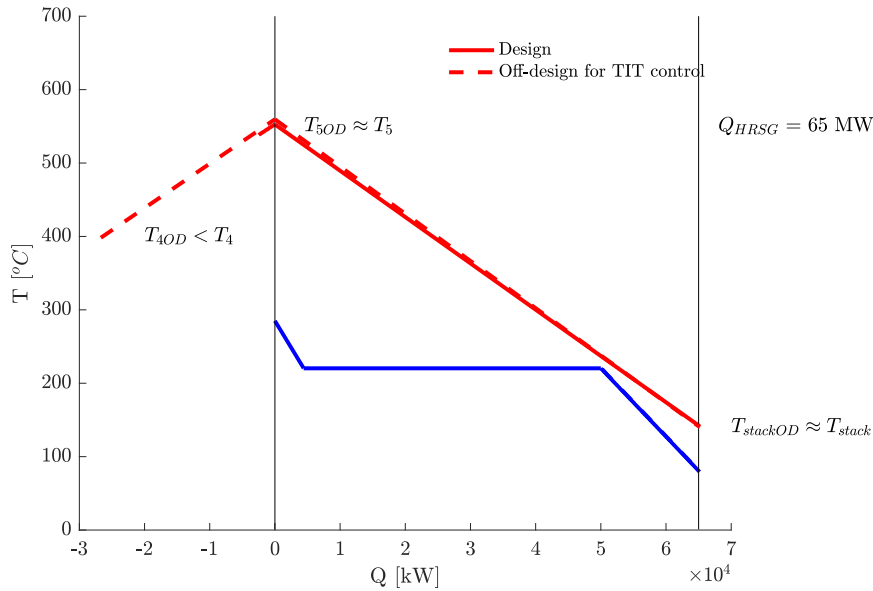


Figure 3.4: T-Q diagram for TIT control. Negative values of Q express the amount of heat required in the SFU to keep the process heat  $Q_{HRSG}$  constant. The dotted lines (- - -) represents the HRSG operation when the CHP load is 50%.

### 3.2.2. IGV control

As previously discussed in chapter 2, depending on the gas turbine, the GT airflow can be decreased down to 70 – 80% of the design value by closing the guide vanes. This limit is equal to 79% for the GE 6531B at which the GT load was found to be 82%.

Figure 3.5 shows the OD operation of the HRSG when the GT load is decreased down to the minimum GT load of 82% by closing the guide vanes. Because of the lower airflow, the slope of the flue gas red line ( $= -\frac{1}{c_{pFG} \dot{m}_{4OD}}$ ) decreases. Despite that the flue gas temperature at the inlet of the HRSG is higher ( $T_{5OD} > T_5$ ), the OD stack temperature will decrease ( $T_{stackOD} < T_{stack}$ ). As a result, according to equation (3.8), the stack losses decrease ( $\Delta Q_{stack} < 0$ ) because both the stack mass flow and temperature are lower than at design.

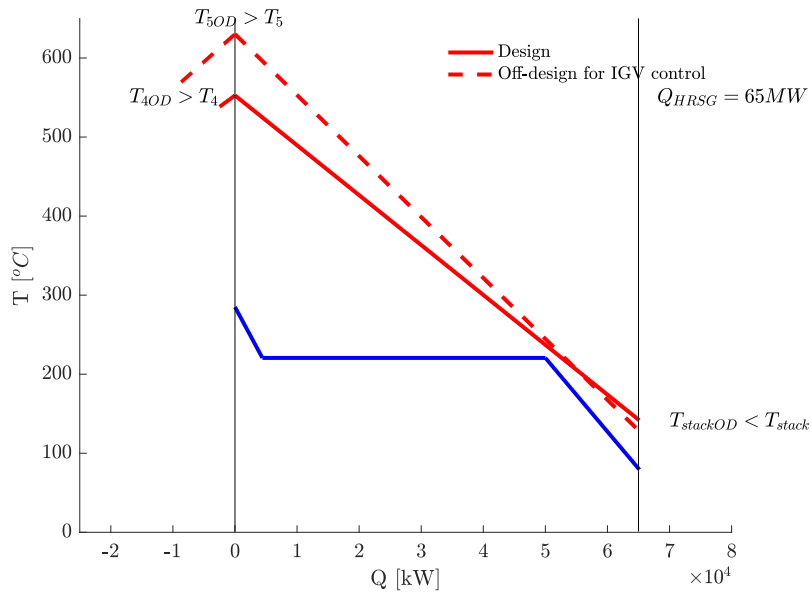


Figure 3.5: T-Q diagram for IGW control. Negative values of  $Q$  express the amount of heat required in the SFU to keep the process heat  $Q_{HRSG}$  constant. The dotted lines (- -) represents the HRSG operation for the minimum achievable CHP load of 82%.

### 3.2.3. CAR control

The same considerations of section 3.2.2 for the OD operation of the HRSG apply to the CAR control because the GT airflow diminishes. As a result, the flue gases stack temperature decreases at part load as shown in figure 3.6 and the stack losses diminish ( $\Delta Q_{stack} < 0$ ).

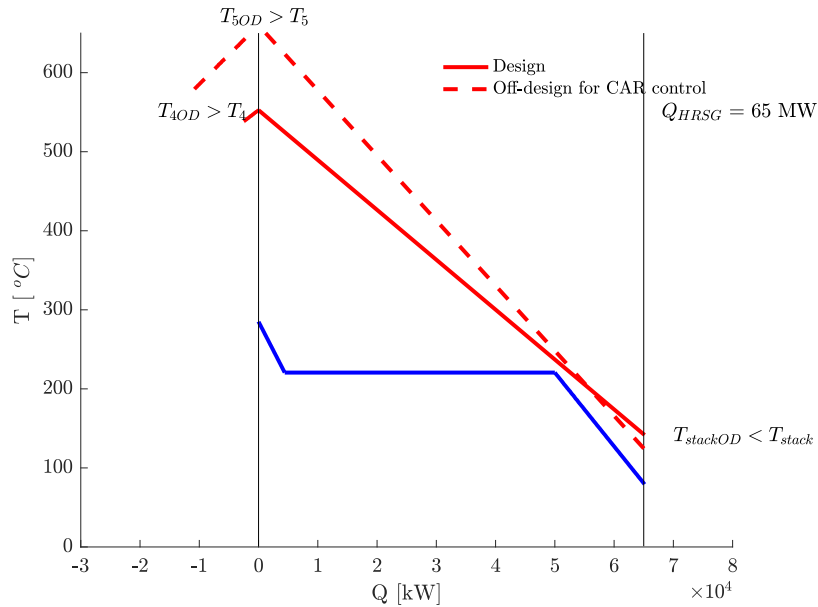


Figure 3.6: T-Q diagram for CAR control. Negative values of  $Q$  express the amount of heat required in the SFU to keep the process heat  $Q_{HRSG}$  constant. The dotted lines (- -) represents the HRSG operation when the CHP load is 50%.

### 3.2.4. FGR control

In a CHP plant, the flue gases stack temperature is usually around 130 – 150 °C. Besides diminishing the plant load, the FGR control decreases the stack temperature down to 90 - 110 °C. However, when recirculating the exhaust gases at the outlet of the economizer, the molar percentage of oxygen at the inlet of the gas turbine diminishes as shown in figure 3.7a because the flue gases mixes with the airflow at ambient temperature. Beyond the oxygen limit of 14.5%, the amount of  $O_2$  at the inlet of the gas turbine is too low to perform a stable combustion in the combustion chamber. Therefore, the minimum achievable load for the CHP plant was found to be 68% at which the oxygen mole concentration at the compressor inlet is 14.5% and the fraction of flue gases recirculated is 42.5%.

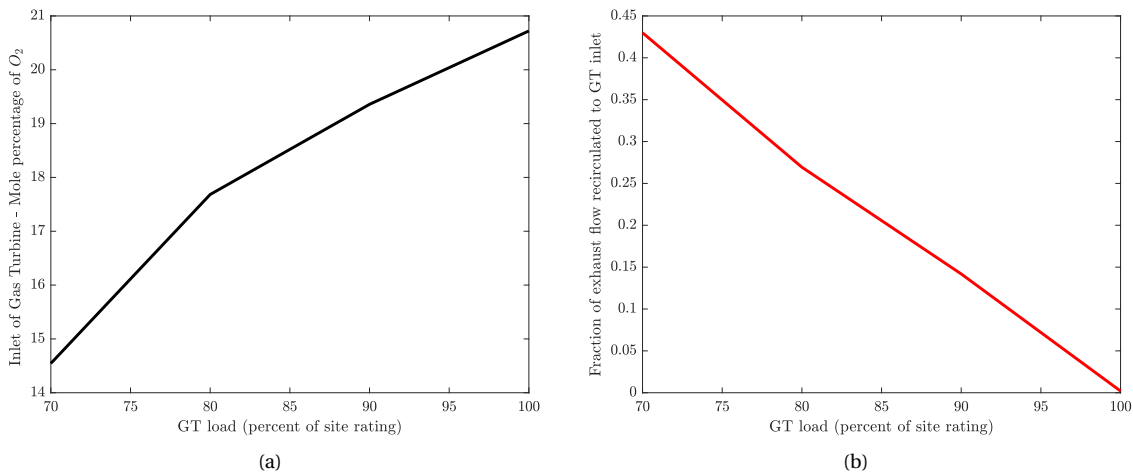


Figure 3.7: (a) FGR control for CHP plant - Mole percentage of  $O_2$  at the inlet of the gas turbine. (b) FGR control for CHP plant: fraction of exhaust gases recirculated to the gas turbine inlet

The same considerations of section 3.2.2 for the OD operation of the HRSG apply to the FGR control because the GT airflow diminishes. As a result, the flue gases stack temperature decreases at part load as shown in figure 3.8 and the stack losses diminish ( $\Delta Q_{stack} < 0$ )

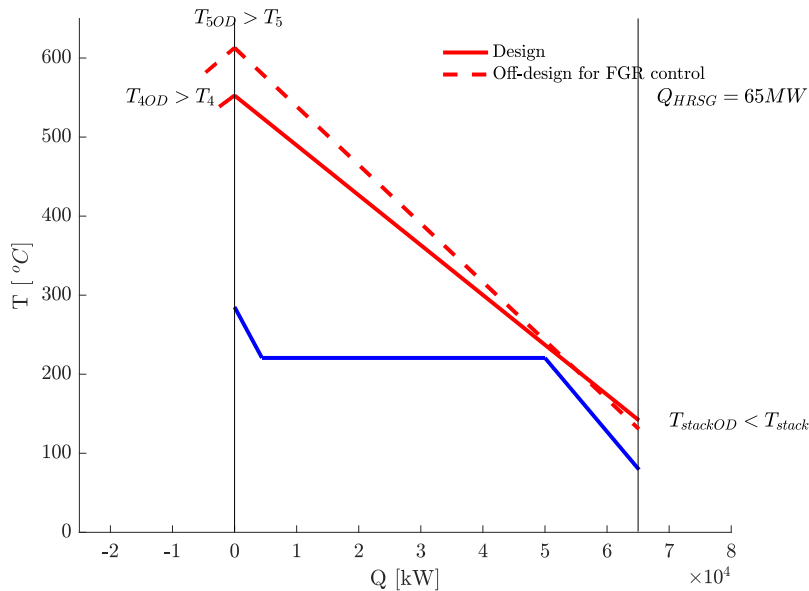


Figure 3.8: T-Q diagram for FGR control. Negative values of  $Q$  express the amount of heat required in the SFU to keep the process heat  $Q_{HRSG}$  constant. The dotted lines (- - -) represents the HRSG operation for the minimum CHP load of 68 %.

### 3.2.5. Part load efficiency

The  $\Delta Q_{stack}$  losses are computed according to equation (3.8) and are shown in figure 3.9 in order to evaluate the performance of each control.

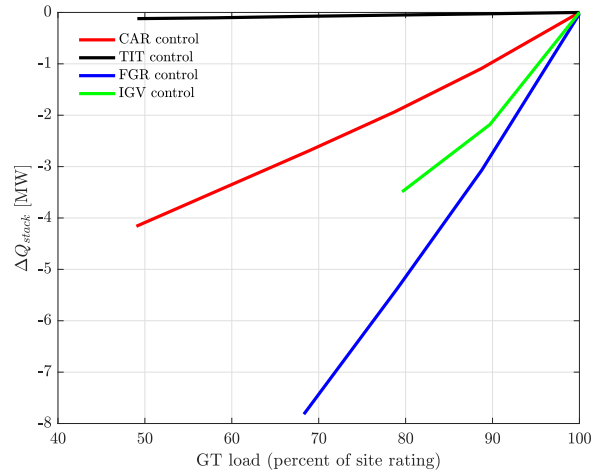


Figure 3.9: CHP plant: Delta stack losses  $\Delta Q_{StackOD}$  at part load for the developed control techniques.

In particular, for the TIT control the stack losses remain untouched as discussed in section 3.2.1. For the other controls, the stack losses will diminish because less stack flow at lower temperature heads to the stack. As a result, the TIT control is the least efficient because of the highest stack losses. Figure 3.10 shows the CHP efficiency at part load for the different part load techniques when the process heat is kept constant and equal to  $Q_{HRSG} = 65 MW$ .

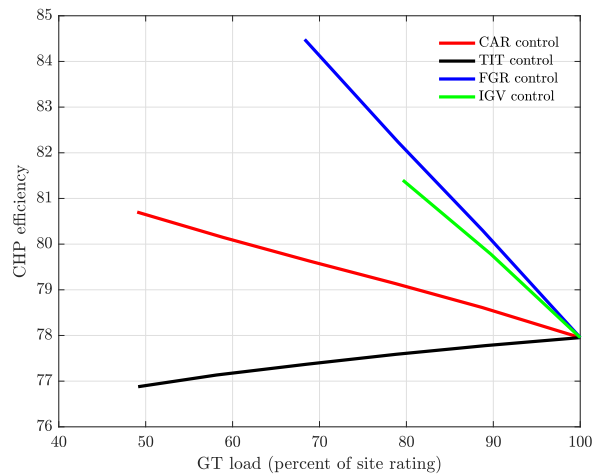


Figure 3.10: CHP efficiency vs  $GT_{load}$  for different control techniques

In chapter 2 for the gas turbine the TIT control was found to be the more efficient than air preheating control. As a matter of fact, for the GT of chapter 2 the stack losses are higher for CAR and FGR control because the turbine exhaust temperature increase at part load. As a result, for the Brayton model, the stack losses are lower for the TIT rather than air pre-heating controls as shown in figure 3.11.

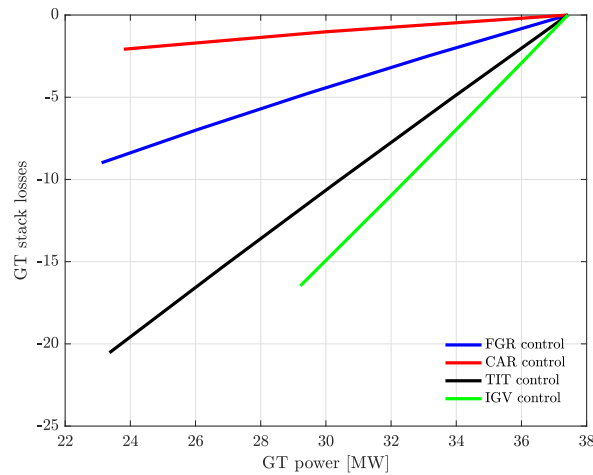


Figure 3.11: Brayton cycle: Delta stack losses  $\Delta Q_{StackOD}$  at part load for the developed control techniques. The lower the stack losses, the higher the part load efficiency.

**Optimum control combination** Although the FGR and IGV controls are the most efficient controls, the GT load can be decreased down to 68% and 82% respectively. When the load has to be decreased further, one or more controls can be combined. The most efficient part load combination was found to be the FGR recirculation followed by the the IGV control as shown in figure 3.12a.

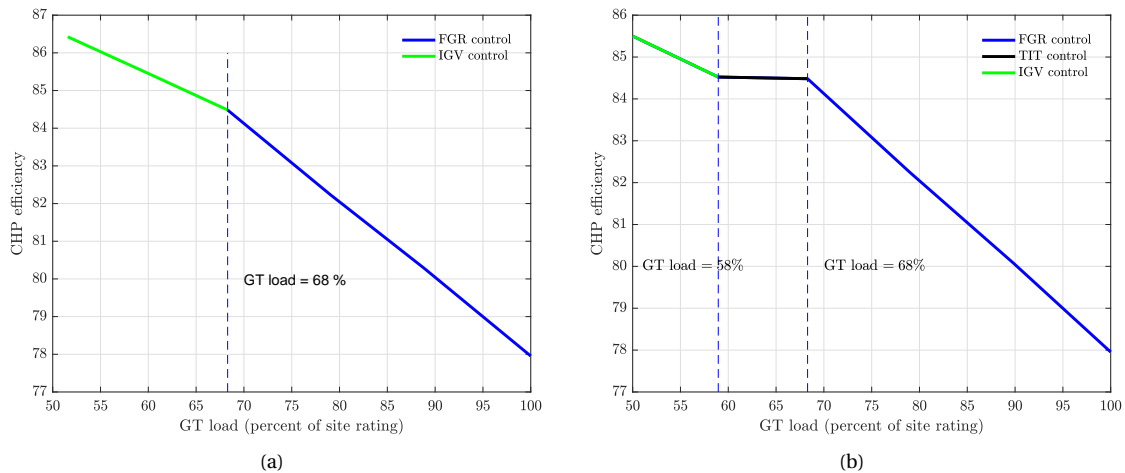


Figure 3.12: (a) CHP efficiency at part load for combined controls: FGR + IGV combination control (b) CHP efficiency at part load for optimum combined control (FGR + TIT + IGV) control.

However, after recirculating the flue gases down to the minimum oxygen concentration, when closing the IGVs the molar concentration of  $O_2$  continues to diminish (because the GT airflow decreases).

Figure 3.12b shows a possible alternative: the flue gases are recirculated down to 68% of the GT site rating. Later on, the GT TIT is decreased until the load of the GT reaches 58%. TIT diminishes the mass of fuel keeping the airflow constant so that the percentages of oxygen at the GT inlet increases. Finally, the IGV control is applied and the load decreases to 50%. Although less efficient than the (FGR + IGV) control technique (figure 3.12a), the oxygen levels are maintained higher than the minimum concentration of 14.5% in order to perform a stable combustion in the GT. Moreover, it is relevant to notice that in figure 3.12b the TIT control efficiency stays almost constant. As a matter of fact, if the TIT control is applied after the FGR control, a fraction of the

stack flow is recirculated to increase the GT inlet temperature. As a result, the stack losses decrease since less mass flow is released to the atmosphere. Therefore, if used in combination with FGR control, the efficiency of the TIT control increase.

**Standard control combination and marginal efficiency** In industry, the CHP plant load is controlled using a standard control combination of both IGV and TIT control as shown in figure 3.13. Initial load reduction is via guide vane closure. Once the vanes are closed down to the limit position, the load is decreased by diminishing the firing temperature. The (FGR +TIT +IGV) combination control of figure 3.12b resulted to be more efficient and the marginal efficiency defined as  $\eta_{margin} = \frac{\eta_{optimum} - \eta_{standard}}{\eta_{standard}}$  with respect to the standard control used in industry refers to figure 3.14a.

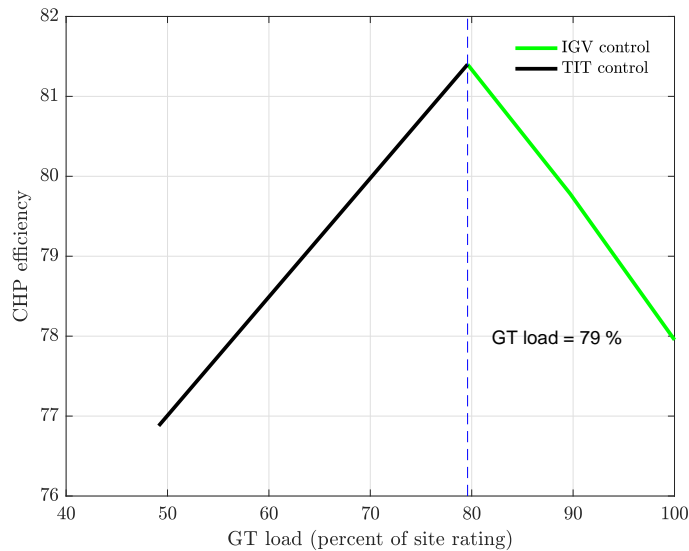


Figure 3.13: CHP plant: Standard control technique combination used in industry. The IGVs are closed up to the limit position and later on the TIT temperature is decreased.

The proposed control combination (FGR +TIT +IGV) becomes significantly more efficient than the standard one when the GT runs below 80% of the site rating reaching a marginal efficiency of 11% when the load is 50%.

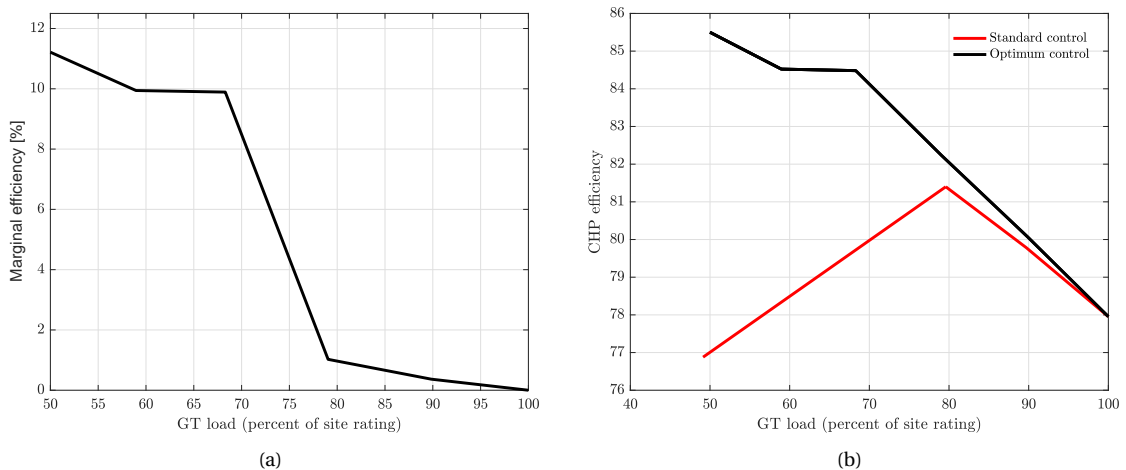


Figure 3.14: CHP plant control combination: (a) marginal efficiency  $\eta_{margin} = \frac{\eta_{optimum} - \eta_{standard}}{\eta_{standard}}$ , (b) CHP efficiency of the optimum & standard combined controls.

### 3.3. Conclusions

In this chapter, several important results were found. Firstly, according to figure 3.10 the TIT control (which was the second most efficient part load technique for the Brayton model) for the CHP plant is the least efficient because of the highest stack losses. Nevertheless, if the TIT control is used in combination with FGR control, its efficiency improves. Secondly, recirculating the flue gases is the most efficient control and figure 3.12b shows the recommended combination controls to achieve deep part load. This combination guarantees a stable combustion in the GT and increases the CHP efficiency with respect to the standard control combination used in industry up to 11% (figure 3.14a).



# 4

## Part load operation of Combined Cycles

Chapter 4 deals with the development of thermodynamic model of a combined cycle using THERMOFLEX. The goal is to predict the system efficiency at part load. The differences with the CHP plant modeling are presented in section 4.1 and the design of a case study is presented in section 4.2. The control techniques developed in chapter 2 are applied to vary the combined cycle load in section 4.3. The system energy balance is derived and the optimum combination control is presented in accordance with the cycle limitations (maximum boiler inlet temperature, minimum oxygen molar concentration and maximum IGVs closure).

### 4.1. Combined cycles (CC)

The major difference between the CHP plant and CC is that for the CC the heat recovered in the HRSG is converted into electricity. In a Rankine cycle the steam produced is expanded in three steam turbines (ST) in order to generate useful electrical energy whereas for the CHP plant the process heat was not converted in electricity. Therefore, for the combined cycle, we have to differentiate between the  $GT_{load}$  and  $CC_{load}$ . The  $CC_{load}$  is defined as follows:

$$CC_{load} = GT_{load} + ST_{load}. \quad (4.1)$$

For instance, if the GT is running at 70% it does not necessarily mean the  $CC_{load}$  is 70%. In general, the  $ST_{load}$  varies according to the part load technique used to control the plant load. Given that no supplementary firing unit is placed at the turbine exhaust, the GT exhaust coincides with the inlet of the boiler. At part load, the flue gases boiler inlet temperature (BIT) and mass flow change in accordance with the control technique used as discussed in the chapters 2 and 3. As a consequence, the OD boiler operation changes according to the control technique used (section 4.3.1). Because we are analyzing the plant as a whole, the results of the simulations are shown in terms of CC control curves and not GT control curves as for the CHP plant. Another important difference is the maximum boiler inlet temperature for part load operation. In particular, for the combined cycle the BIT is limited by the material properties of the wall insulation of the boiler and of the turbine. In this chapter a boiler inlet temperature limit of  $BIT_{limit} = 650^{\circ}C$  is assumed.

## 4.2. Design of a Combined Cycle

For this case study, the gas turbine of General Electric (model nr. 6101FA) is selected. Table 4.1 shows the design characteristics of the selected gas turbine.

Manufacturer & model	Shafts	RPM	$\pi$	TIT [ $^{\circ}C$ ]	T4 [ $^{\circ}C$ ]	Airflow [ton/h]	Shaft Power [kWe]	LHV efficiency [-]	Price [MM\$]
GE 6101FA	1	5100	14.8	1287.8	598	725.1	69290	33.83	14.8

Table 4.1: Gas turbine selected for the CC

The detailed CC flow diagram is presented in the Appendix. A schematic flow diagram is shown in figure 4.1. The HRSG/boiler provides steam for the three ST at the pressures of 100, 25 and 4.2 bars.

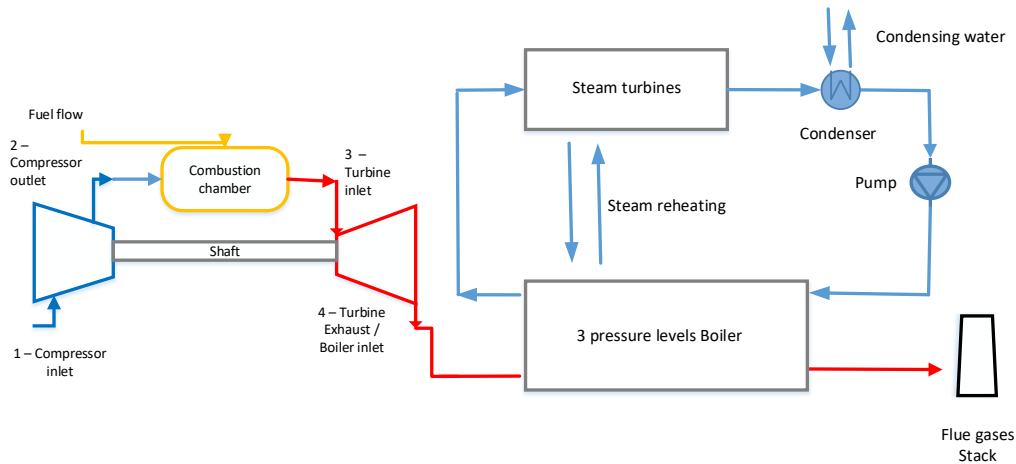


Figure 4.1: Schematic flow diagram of the CC. The detailed flow diagram is shown in the appendix.

Figure 4.2 shows the ST expansions in the h-s diagram. In the designed combined cycle, when the steam exits the high pressure turbine (HP), the steam is sent again to the boiler, reheated up to the steam turbine inlet temperature of  $STIT = 551.7^{\circ}C$  and expanded in the intermediate and low pressure steam turbines. After exiting the low pressure turbine, the steam has a temperature of  $T_{cond} = 33.5^{\circ}C$  and exits the condenser when all the vapor is condensed.

Parameter	Value	Unit	Description
BIT or $T_4$	598.7	[ $^{\circ}C$ ]	Boiler inlet temperature or GT exhaust temperature
$P_{1ev}$	4.2	[bar]	Water evaporation pressure - first pressure level of the HRSG
$P_{2ev}$	25	[bar]	Water evaporation pressure - second pressure level of the HRSG
$P_{3ev}$	100	[bar]	Water evaporation pressure - third pressure level of the HRSG
STIT	551.7	[ $^{\circ}C$ ]	HP and IP steam turbine inlet temperature
$T_{stack}$	110.2	[ $^{\circ}C$ ]	Flue gases stack temperature
$T_{cond}$	33.5	[ $^{\circ}C$ ]	Water/steam condensation temperature
$m_{cond}$	30	[kg/s]	Water/steam mass flow in the condenser

Table 4.2: CC: design values of the boiler/HRSG

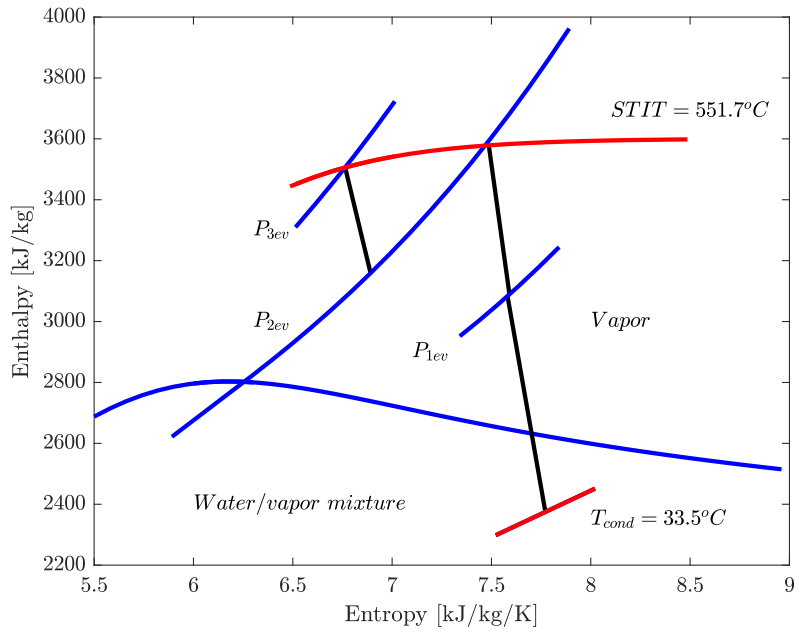


Figure 4.2: CC: ST h-s diagram at design. The blue curves represent the water/steam saturation curves and steam isobars. The red isotherm curve shows that when exiting the high pressure turbine, the steam is reheated before being expanded in the intermediate ST.

**System energy balance** Similarly to the combined heat and power plant, equation (4.2) represents the system energy balance of the combined cycle.

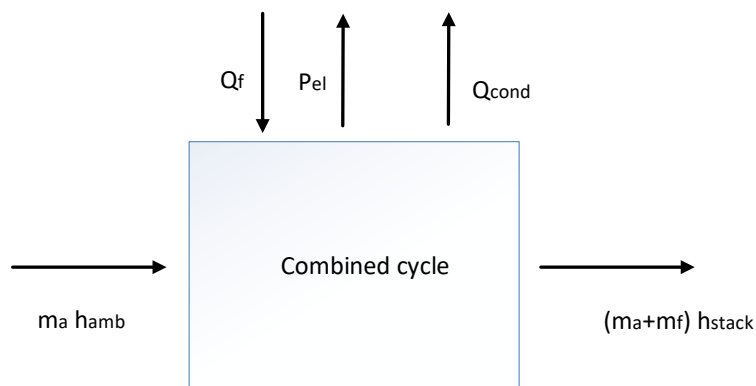


Figure 4.3: Combined cycle: energy balance.

$$Q_f = P_{el} + Q_{cond} + Q_{stack} \tag{4.2}$$

$$Q_f = P_{el} + Q_{losses} \tag{4.3}$$

The system energy balance (4.2) emphasizes the fact that a part of the net fuel input  $Q_f$  is converted into electricity  $P_{el}$  (in the GT and ST) whereas the other parts ( $Q_{stack}$  and  $Q_{cond}$ ) are regarded as losses.  $Q_{stack}$  are the stack losses defined in chapter 3. In a combined cycle  $Q_{cond}$  represent the heat rejected in the condenser.

### 4.3. Part load operation

The approach used to investigate the part load operation of the CC is similar to the approach used for the CHP plant. Analogously to the CHP plant, at part load the electrical power of the CHP plant is diminished by a  $\Delta P_{el} = P_{elOD} - P_{el} < 0$ . The change in fuel flow  $\Delta Q_f = Q_{fOD} - Q_f$  is expressed in equation (4.4):

$$\Delta Q_f = \Delta P_{el} + \Delta Q_{cond} + \Delta Q_{stack}. \quad (4.4)$$

**Steam turbines inlet temperature** At part load the steam turbine inlet temperature is controlled via spray cooling. At the inlet of the high pressure and intermediate pressure steam turbines, a desuperheater is placed wherein water is sprayed. Hence, spray cooling ensures the steam temperature stays below the design value of  $STIT = 551.7^\circ C$ . This steam temperature control is widely used industry to avoid high thermal stresses on the rotor blades which can diminish the useful life of the ST.

**Heat rejected in the condenser** When exiting the LP turbine, the steam/water mixture  $\dot{m}_{cond}$  is condensed at the temperature of  $T_{condOD} = T_{cond} = 33.5^\circ C$ . Its enthalpy  $h_{cond_{inOD}}$  depends on the condensing temperature and steam/water quality  $q_{cond_{inOD}}$ . Given that all the vapor is condensed ( $q_{cond_{outOD}} = q_{cond_{out}} = 0$ ),  $h_{cond_{outOD}} = h_{cond_{out}}$ . As a result, the heat rejected in the condenser  $Q_{condOD}$  is computed as follows:

$$Q_{condOD} = \dot{m}_{condOD} (h_{cond_{inOD}} - h_{cond_{out}}). \quad (4.5)$$

#### 4.3.1. Steam turbines load

In general, the heat transferred to the water/steam (the steam turbines load) depends on the GT exhaust temperature and mass flow.

**General boiler energy balance** In chapter 3 the process heat of the CHP plant was maintained constant. For the combined cycle, no supplementing firing unit is placed at the GT exhaust and the heat transferred from the flue gases to the water/steam ( $Q_{boiler}$ ) varies at part load in accordance with the boiler inlet temperature and GT exhaust flow. Figures 4.4a and 4.4b show how  $Q_{boiler}$  varies at part load when changing the BIT keeping the GT exhaust flow constant and when changing the GT exhaust flow keeping the BIT constant. Figure 4.4 is generic for the boiler energy balance and do not refer to any specific part load control. Figure 4.4 shows that any decrease/increase of BIT or GT exhaust flow causes the steam/water flows and steam turbines load to decrease/increase.

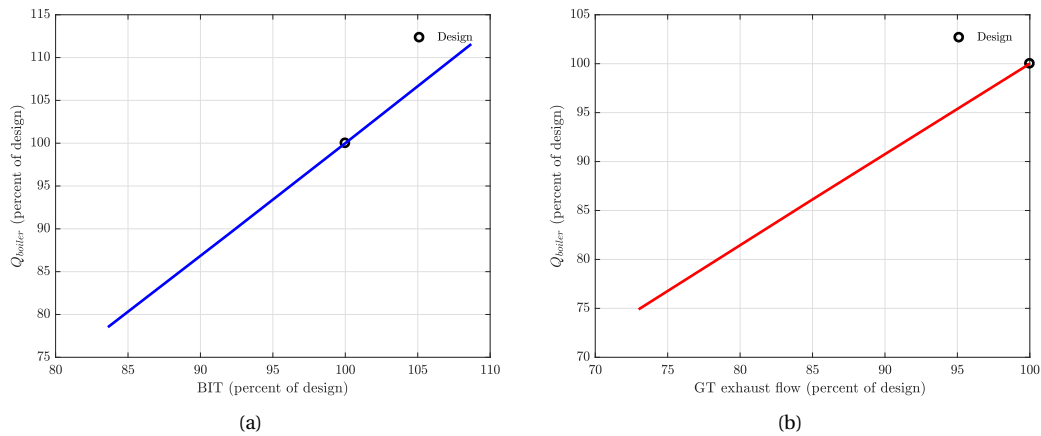


Figure 4.4: CC:  $Q_{HRSG}$  versus GT exhaust flow keeping the BIT constant (a) & BIT keeping the GT exhaust flow constant (b).

Figure 4.5 shows in detail how the  $ST_{load}$  and steam/water flow (of the condenser) diminish according to GT part load technique.

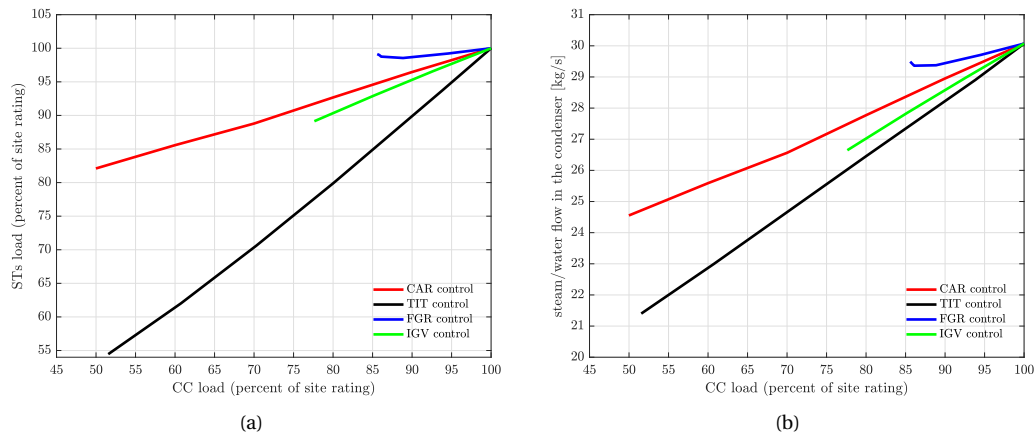


Figure 4.5: CC: $ST_{load}$  (a) & steam/water flow in the condenser (b) versus  $CC_{load}$

**TIT control** For the TIT control the GT exhaust flow stay almost constant whilst the BIT decreases. According to figure 4.4a for lower BIT less heat is transferred to the water/steam, thus less steam is produced in the boiler and consequently less power is produced in the ST.

For CAR, FGR and IGV controls the BIT increases and the GT exhaust mass flow diminishes as previously explained in chapter 2.

**FGR control** It is interesting to notice that for the FGR control, the ST load stay almost constant in figure 4.5a. As a matter of fact, although the heat transferred to the steam/water diminishes because of the lower GT exhaust flow, the increase of the BIT compensates the reduction of  $Q_{HRSG}$ .

**IGV & CAR controls** Similarly to FGR control, for IGV and CAR controls the exhaust temperature increases. However, for the same exhaust flow the increase of BIT for IGV and CAR is inferior to the FGR control. For this reason, the heat transferred to the water/steam, hence the  $CC_{load}$ , decreases more for IGV and CAR with respect to the FGR control.

### 4.3.2. Part load efficiency

The CC efficiency is defined as follows:

$$\eta_{CC} = \frac{P_{el}}{Q_f}. \quad (4.6)$$

At part load, the electrical power of the CC is diminished by a  $\Delta P_{el} = P_{elOD} - P_{el} < 0$ :

$$\eta_{CCOD} = \frac{\Delta P_{el} + P_{el}}{\Delta Q_f + Q_f}. \quad (4.7)$$

Reminding that  $\Delta Q_f = \Delta P_{el} + \Delta Q_{losses}$ :

$$\eta_{CCOD} = \frac{\Delta P_{el} + P_{el}}{\Delta P_{el} + \Delta Q_{losses} + Q_f}. \quad (4.8)$$

**Depicting losses** For the combined cycle, the delta system losses  $\Delta Q_{losses}$  are classified as follows:

- $\Delta Q_{stack}$  are the delta stack losses (figure 4.6a). Similarly to the CHP plant, because they strongly depend on the stack mass flow and temperature, for the FGR control they are also the lowest for the CC. For the TIT control the stack losses increase because the stack temperature slightly increase.
- $\Delta Q_{cond}$  regarded as delta condensation losses (figure 4.6b):

$$\Delta Q_{cond} = Q_{condOD} - Q_{cond} \quad (4.9)$$

The delta condensation losses strictly depend on the OD steam/water condensation flow and therefore on the steam turbines load (figure 4.5a).

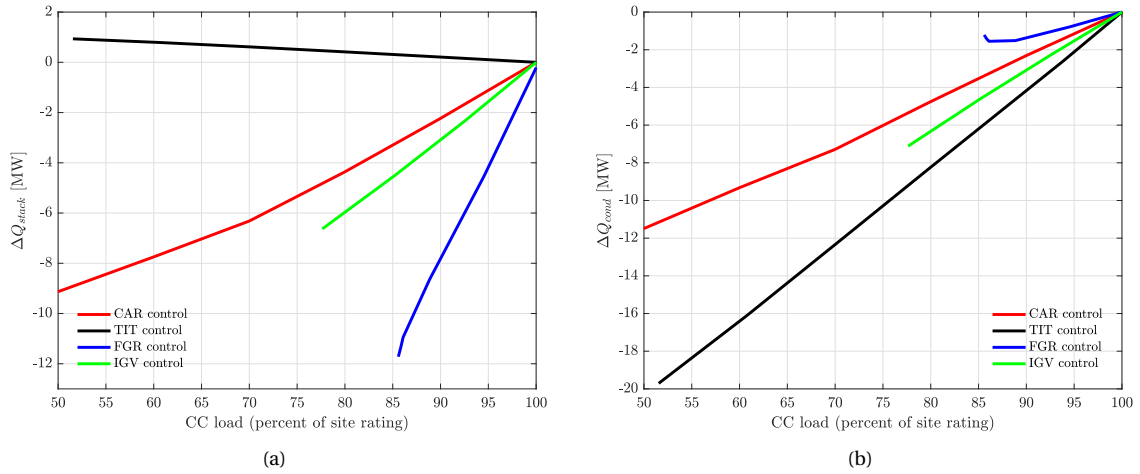


Figure 4.6: (a)  $\Delta Q_{stack}$  for the different part load techniques. (b)  $\Delta Q_{cond}$  for the different part load techniques.

When comparing the part load efficiency of different controls in equation (4.8) the terms  $\Delta P_{el}$ ,  $P_{el}$  and  $Q_f$  are constant. The only term that changes in equation (4.8) is  $\Delta Q_{losses}$ . Therefore, depending on the delta system losses  $\Delta Q_{losses}$  of each control (figure 4.7) one part load technique will be more efficient than the other.

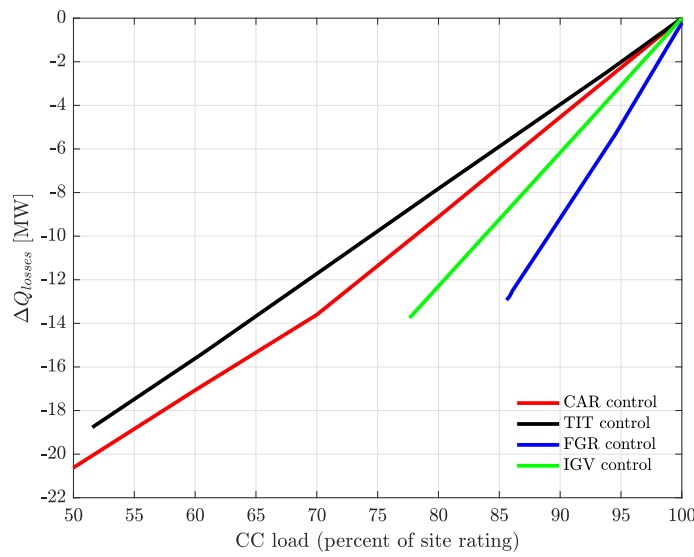


Figure 4.7: CC: delta system losses  $\Delta Q_{losses}$  for the different part load techniques. The delta system losses are equal to the sum of the delta condensation and delta stack losses.

Figure 4.8 shows the part load efficiency for the different control techniques when the CC load is decreasing. Although the condensation losses are higher for the FGR control because the ST load stay almost constant (figure 4.5), recirculating the exhaust gases to the GT inlet is found to be the most efficient control technique (lowest delta system losses). However, since the steam turbines load stay almost constant, the combined cycle load can be decreased only down to 86% otherwise the amount of oxygen at the inlet of the gas turbine would be below 14.5%. The second most efficient control is found to be IGV followed by CAR and TIT controls.

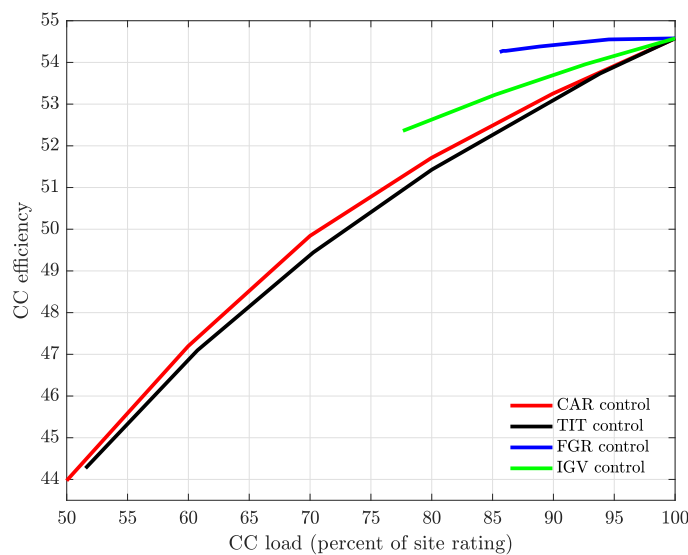


Figure 4.8: CC efficiency at part load.

**Optimum control combination.** The minimum oxygen molar concentration, the maximum boiler inlet temperature and the maximum guide vane closure limit the part load operation of the Combined Cycle. In accordance with the limitations, the most efficient (part load) control combination was found to be a combination of FGR, IGV and TIT controls as shown in figure 4.9a. Firstly, the flue gases are recirculated up to the minimum achievable load of 86% to have a stable combustion in the GT. Secondly, the inlet guide vanes are closed up to 83% of the site rating reaching the maximum BIT allowed of  $BIT_{limit} = 650^{\circ}C$  as shown in figure 4.9b. Thirdly, the BIT is maintained constant (decreasing the GT TIT and closing the IGV at the same time) until the IGVs reach the limit vanes closure. Finally, the load is decreased down to 50% reducing the GT TIT.

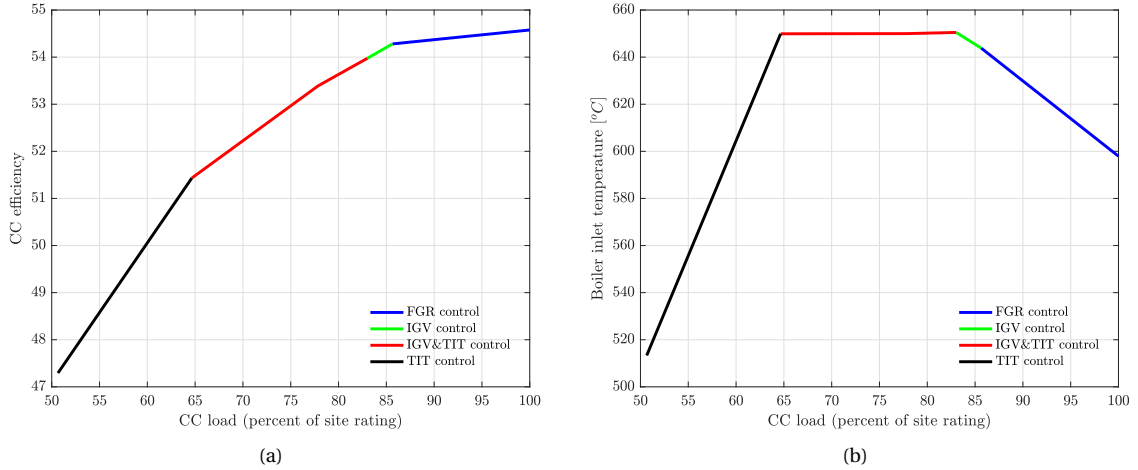


Figure 4.9: Optimum CC control combination: (a) CC efficiency & (b) Boiler inlet temperature at part load. The boiler inlet temperature is maintained below  $BIT_{limit}$  due to the limitation imposed by the material properties of the wall insulation of the boiler and of the turbine.

**Standard control combination and marginal efficiency.** In industry, the most common (part load) control combination is a combination of IGV and TIT controls. In such a control combination, the load is initially decreased via vane closure up to the limit  $BIT_{limit}$ . Later on, the BIT is kept constant (closing the IGVs and decreasing the gas turbine TIT at the same time). After reaching the maximum vane closure, the load is further decreased reducing the GT TIT. For the CC modeled, it was found that for the  $BIT_{limit}$  of  $650^{\circ}C$  the guide vanes were already reached the maximum closure. The standard control used in industry is shown in figures 4.10.

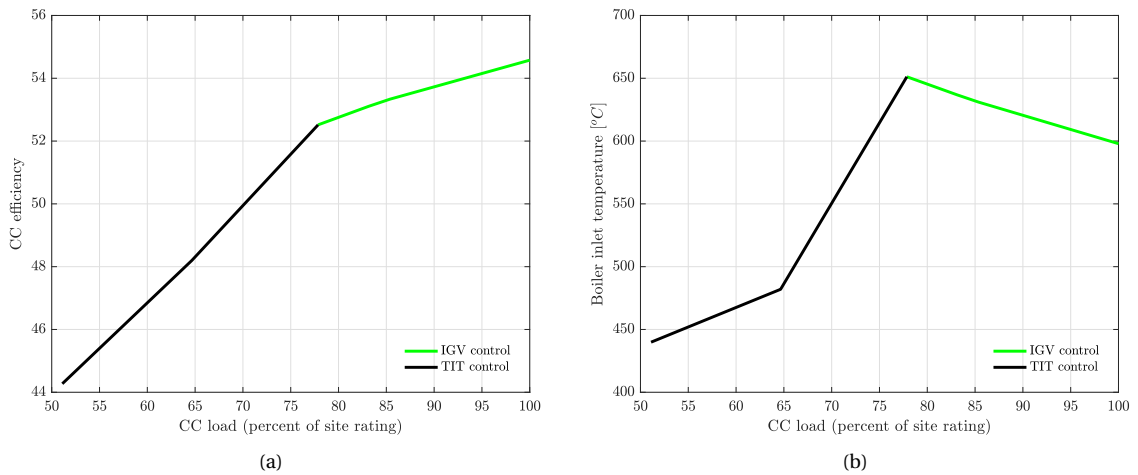


Figure 4.10: Standard CC control combination: (a) CC efficiency & (b) Boiler inlet temperature at part load.

The proposed optimum control combination is compared with the standard one and its marginal efficiency, as shown in figure 4.11a. The marginal efficiency is always positive. In general, the lower the combined cycle load, the higher the marginal efficiency. From 75 to 100 % the marginal efficiency increases up to 2 %. For lower cycle loads, the marginal efficiency increases up to around 7%.

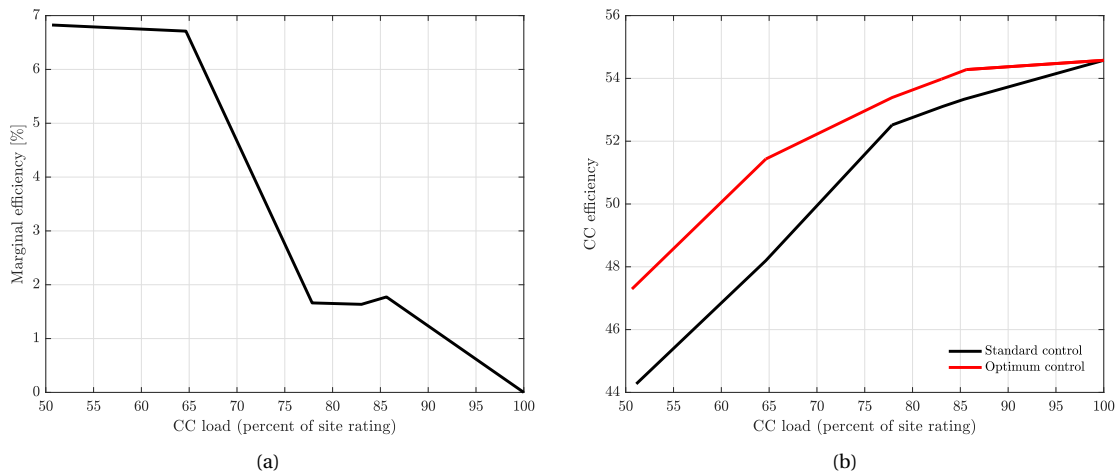


Figure 4.11: CC control combination: (a) marginal efficiency  $\eta_{marg} = \frac{\eta_{optimum} - \eta_{standard}}{\eta_{standard}}$ , (b) CC efficiency of the optimum & standard combined controls.

## 4.4. Conclusions

The goal of this chapter was to apply the control techniques developed in chapter 2 to a combined cycle. Unlike the CHP plant, the BIT limits the part load operation. Considering a maximum boiler inlet temperature of  $BIT_{limit} = 650^{\circ}C$ , a minimum compressor inlet oxygen molar concentration of 14.5%, the optimum control combination (figures 4.9) was found to improve the combined cycle efficiency at part load up to 7% (figure 4.11a) with respect to the standard control applied in industry (figure 4.10).



# 5

## Impact of part load operation on the turbine vane/blade temperature

The turbine cooling has always been an issue for GTs operating at high TIT. This chapter presents a model that either evaluates the turbine cooling requirements in a stage design or predicts the effects of part load operation on the performance and durability of the gas turbine. In section 5.2 the modeling equations are presented. The calculation scheme to estimate the cooling requirements for one blade in a stage design is presented. In section 5.3 the data from chapter 3 is used to evaluate the impact of part load operation on the blades/vanes temperature. Special attention to FGR is given.

### 5.1. Cooling of gas turbines

The turbine inlet temperature (TIT) and the GT pressure ratio are of most importance for the thermodynamic performance of a gas turbine. Figure 5.1 shows the gas turbine efficiency as a function of the GT pressure ratio and TIT.

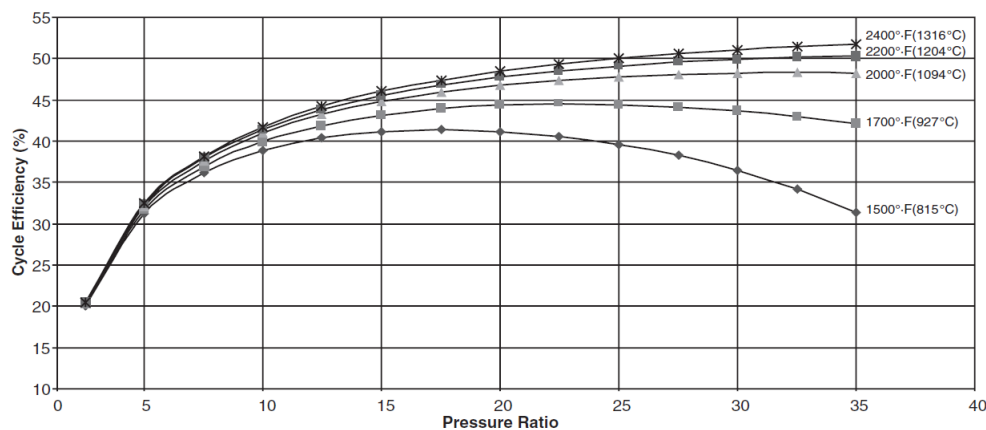


Figure 5.1: Cycle efficiency as a function of the firing temperature and pressure ratio for a compressor efficiency of 87% and turbine efficiency of 92% [5].

For instance, for a GT pressure ratio of 20, an increase of the turbine inlet temperature of  $112^{\circ}\text{C}$  produces an upgrade of the thermal efficiency of 4%. However, the turbine inlet temperature is limited by the material properties of the turbine blade and vanes. A too high temperature would lead to excessive corrosion and oxidation of the blades and thereby a reduction in its life time [5]. In the last decades, a significant increase has been achieved in higher inlet temperatures due to a combination of improved materials, like single crystals, and improved cooling mechanisms like film cooling and impingement cooling (figure 5.2).

In a cooling system, a fraction of the high pressure compressor airflow is used to cool down the vanes/blades

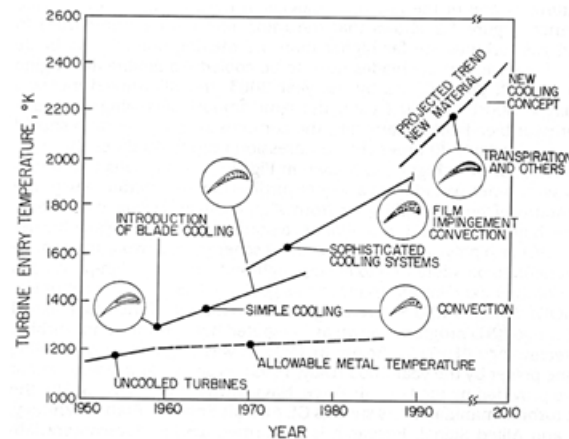


Figure 5.2: Increase of the TIT over the years [16].

of the turbine. However, a high percentage of cooling flow can decrease the turbine work and consequently decrease the GT efficiency [5, 16]. Thus, a cooling system that keeps the cooling air at a minimum and that meets the material temperature requirements need to be designed.

The cooling mechanisms are classified as follows:

- 1 External cooling mechanism (ablation, transpiration and film cooling).
- 2 Internal cooling mechanism (rib turbulated cooling, jet impingement cooling and pin fin cooling).

Sections 5.1.1 and 5.1.2 elaborates on the cooling transfer mechanisms.

### 5.1.1. External cooling

External cooling refers to the cooling mechanisms that decrease the external blade/vane surface temperature. The three main external cooling mechanisms are: ablation, transpiration and film cooling.

In *ablation* a thermal barrier coating for insulating the blades is used. It serves as insulation for the turbine blades to increase the operating temperature of the GT by 100-150 °C [16]. Research is being conducted by many universities, gas turbine manufactures companies to identify the best material suitable for working at high temperatures [16].

In *transpiration cooling* a porous material cools down the surface venting the coolant to the blade surface.

*Film cooling* ensures the temperature gradients of the material blade are kept at an acceptable level. The coolant, that is the fluid that decreases the temperature of the blades, is introduced along the vane/blade surface through holes to protect the airfoils from high temperatures (figure 5.4).

Film cooling and ablation are selected by manufactures as external cooling mechanisms since nowadays transpiration cannot be readily applied in GT cooling [16].

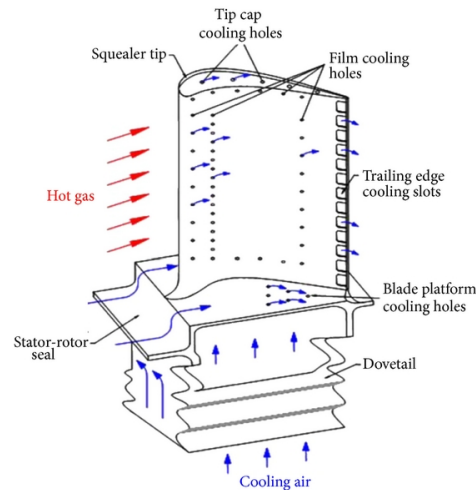


Figure 5.3: Blade/vane external heat transfer: film cooling.

### 5.1.2. Internal cooling

Unlike the film cooling which provides direct protection to the airfoils from the hot gases flow, the internal cooling removes heat from inside the airfoils. In a cooling system the coolant airflow is a fraction of the compressor discharge flow. It enters the turbine blades because of the pressure difference between the compressor discharge and turbine inlet. Figure 5.4 shows a longitudinal cut of a turbine blade.

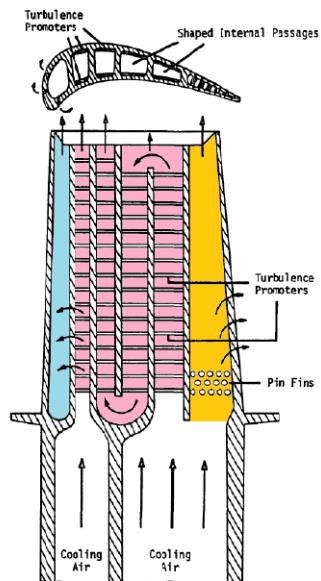


Figure 5.4: Blade cooling mechanisms in gas turbines [16].

One of the most used cooling systems of a blade in a gas turbine is the *convection cooling*. The coolant which flows inside the middle part of turbine blades/vanes (pink area in figure 5.4) removes heat. To enhance the heat transfer, turbulence promoters are used. This is the reason for why *convection cooling* is also regarded as *rib turbulated cooling*.

*Jet impingement cooling* is used where the most critical conditions exist, for example the stagnation point of a rotor blade in the leading edge of the blades/vanes (area in blue in figure 5.4). Jet impingement consists of an air jet flow to remove heat (figure 5.5 and figure 5.6). After impinging the blade internally the coolant can be used in the trailing edge of the blade/vane for film cooling (figure 5.6).

*Pin fin cooling* consists of a cooling channel in the trailing edge of the vanes/blade where the coolant is slowed

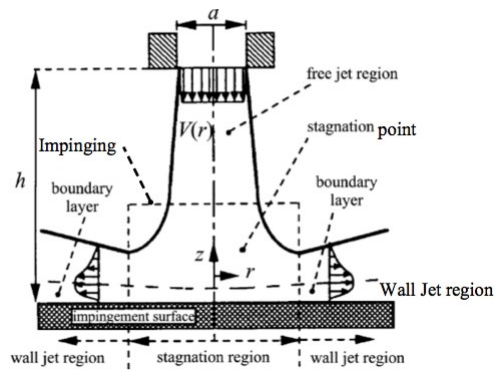


Figure 5.5: Internal cooling: jet impingement nozzle.

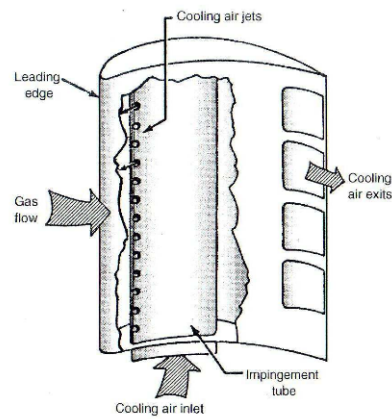


Figure 5.6: Blade cooling mechanisms in gas turbines: jet impingement

down by obstacles called pin fins oriented vertically to the flow direction (orange area in figure 5.4). Because the pins protrude to the external vane/blade surface, pin film cooling is a combination of both internal and external heat transfer.

## 5.2. Turbine cooling equations

For the on-design, the model calculates the requirements (coolant mass flow) to decrease the temperature of one blade down to the maximum allowable temperature  $T_{max}$ . A maximum blade temperature of  $T_{max} = 900^{\circ}C$  is considered [16]. For this model, the blades/vanes geometry are shown in figure 5.7. The blade/vane shape is assumed to be paralelepipedal for the sake of simplicity.

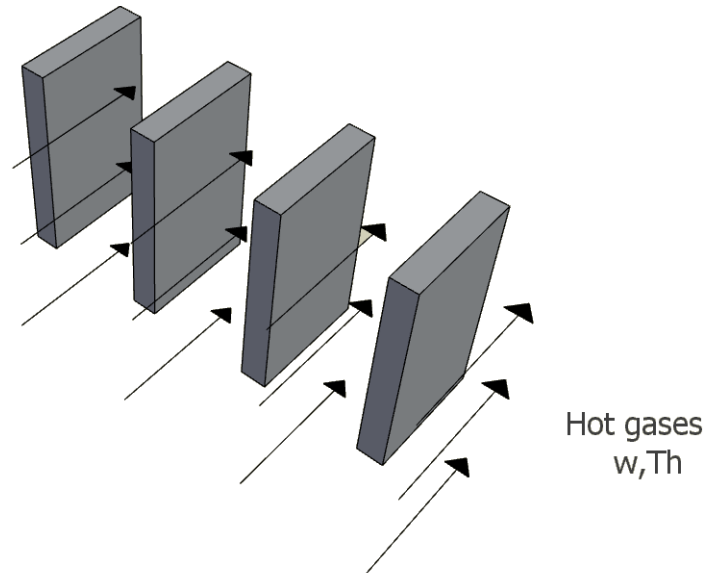


Figure 5.7: Turbine cooling: vanes/blades shape.

**Wall composition:** Figure 5.8 shows the multi-layered surface of a turbine blade. The thermal barrier coating is connected to the blade superalloy through a bounding agent. In real life applications when designing a cooling system, the thermal barrier coating is not taken into account. In case of malfunction with the thermal barrier coating, the blade would still be cooled down without damaging the blade.

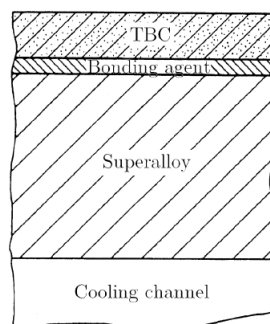


Figure 5.8: Multi-layered surface of blade.

Three heat resistances in series represent schematically the heat transfer mechanisms in a blade (see figure 5.9) [16]. In particular,  $T_c$ ,  $T_{w_i}$  and  $T_{w_o}$  and  $T_f$  are the coolant temperature, the inner and outer wall temperature and the film temperature. The coolant temperature is equal to  $T_c = 350^{\circ}C$  from chapter 3.

For this model a superalloy of thickness of  $t_s = 2\text{ mm}$  with a thermal conductivity of  $k_s = 25\text{ W/mK}$  is assumed.  $\frac{1}{h_{ext}}$  and  $\frac{1}{h_{int}}$  are the heat transfer resistances due to external and internal heat transfer[19].

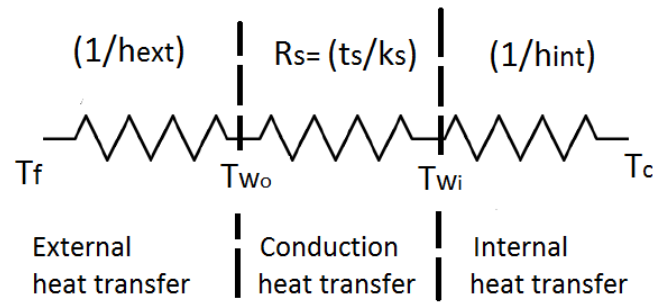


Figure 5.9: Schematic temperature profile in a blade.

**Calculation procedure:** The thermodynamic properties (density, conductivity, viscosity, heat capacities etc.) are computed using the data from chapter 3 and with the help of the thermodynamic library FLUID-PROP [8]. The blade is split in two sections, the leading edge and middle-trailing edge sections:

- Leading edge: here the most critical conditions exist since it is the stagnation point of the blade. This section of the blade is cooled internally with impingement cooling. No film cooling is applied.
- Middle-trailing edge: Internal heat transfer takes place due to convection cooling. Film cooling is applied for decreasing the temperature of the blade.

At thermal equilibrium, the heat absorbed by the blade ( $Q_{ext}$ ) has to be equal to the heat absorbed by the coolant in order to keep the blade temperature at  $T_{max}$ . Hence, at thermal equilibrium:

$$\begin{cases} Q_{ext} = Q_{imp} & \text{at the leading edge} \\ Q_{ext} = Q_{conv} & \text{at the middle-trailing edge} \end{cases} \quad (5.1)$$

At both the leading and middle-trailing edges the external heat transfer is estimated in accordance with the modeling equations of section 5.2.1. To calculate the (internal) coolant requirements an initial guess of the coolant mass flow (both for convection and impingement cooling) is made and the internal heat transfer  $Q_{imp}$  and  $Q_{conv}$  are calculated according to the procedure shown in section 5.2.2. If thermal equilibrium is reached, the calculation is stopped. Otherwise, the (internal) coolant mass flow is increased and simulations runs until the differences  $\Delta Q_1$  between  $Q_{conv}$  and  $Q_{ext}$  and  $\Delta Q_2$  between  $Q_{imp}$  and  $Q_{ext}$  meet the convergence criteria  $\Delta Q_1, \Delta Q_2 < 0.5W$ .

### 5.2.1. External heat transfer ( $Q_{ext}$ )

The following assumptions and simplifications are made made for calculating the external heat transfer:

1. The velocity of the hot gases  $w$  is assumed constant through the blades/vanes for the sake of simplicity.  $w = 450 \frac{m}{s}$  since it is a typical velocity in axial turbines [5].
2. Typical values for the blade/vane geometry are selected [16] (see table 5.1 and figure 5.10).
3. The turbine inlet temperature of  $TIT = 1093^\circ C$  from chapter 3.

Parameter	Value	Description
$h$	1.0cm	Chord height
$w_c$	6cm	Chord width
$l$	1.5cm	Chord length

Table 5.1: Vanes/blades geometric design.

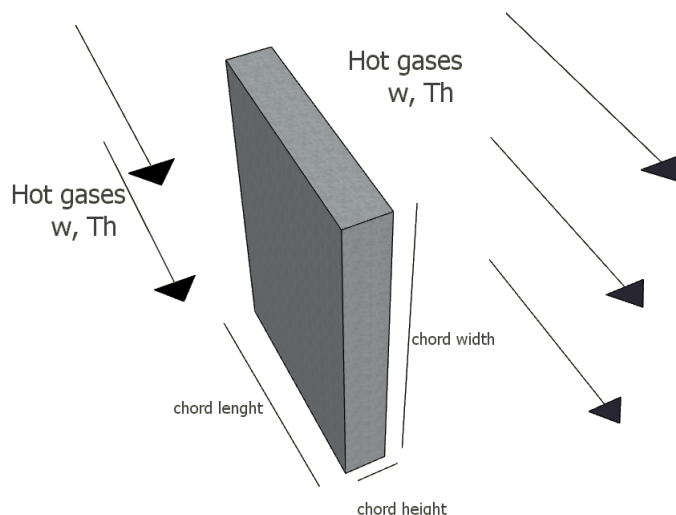


Figure 5.10: Turbine blade cooling: vanes/blades shape simplification.

**Hot gases temperature** If TIT is the GT turbine inlet temperature, a static temperature of the hot gases  $T_h$  can be calculated from the definition of total temperature [11] in equation (5.2):

$$TIT = T_h \left( 1 + \frac{k_{FG} - 1}{2} \frac{w^2}{k_{FG} R_h T_h} \right) \quad (5.2)$$

where  $k_{FG}$  is the isentropic exponent of the hot gases,  $w$  is the hot gases velocity and  $R_h$  is the gas constant of the hot gases. The hot gases temperature  $T_h$  is required for the computation of the external heat transfer in the next two paragraphs. In the middle-trailing edge  $T_h$  is calculated according to equation (5.2) whereas in the leading edge the temperature of the hot gases is equal to the TIT since it is stagnation point of the blade (figure 5.11).

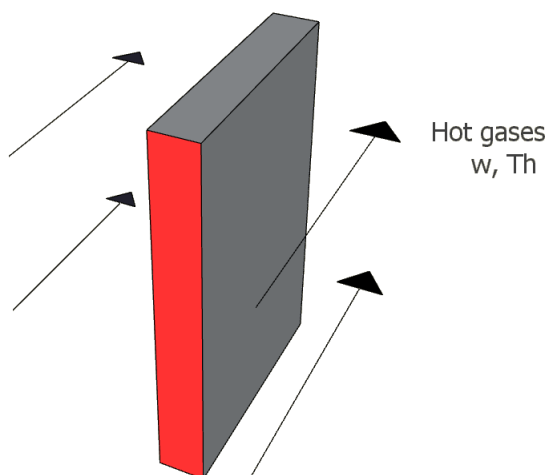


Figure 5.11: Stagnation point (red area) in the leading edge.

**Middle-trailing edge** External heat transfer in the middle-trailing edge occurs due to film cooling: a thin layer of coolant is used to cool down the external blade surface. Many researchers have investigated film cooling on flat surfaces. Recent studies show the results of film cooling on flat surfaces can be adapted to real gas turbines with some correction factors [16]. As shown in figure 5.12, in film cooling the coolant mixes with hot gases creating a film layer. Its temperature  $T_f$  is higher than the maximal wall temperature  $T_{max}$ . Therefore, the heat absorbed by the blade/vane is equal to:

$$Q_{ext} = h_{ext} A_{ext} (T_f - T_{max}), \quad (5.3)$$

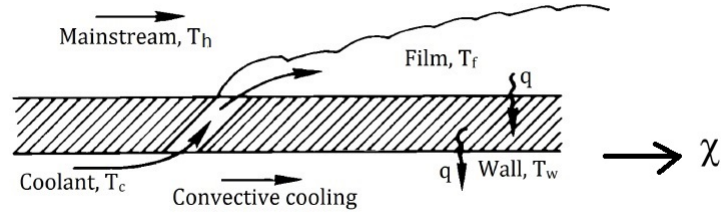


Figure 5.12: Turbine blade cooling - film cooling [5].

where  $A_{ext}$  is the heat transfer area in the middle-trailing edge and equal to  $A_{ext} = 2 l w_c$  (see figure 5.10). In order to compute  $Q_{ext}$  both  $T_f$  and the external heat transfer coefficient  $h_{ext}$  (due to convection between the film and the wall) have to be estimated. In order to estimate the film temperature, the film effectiveness is used. The film cooling effectiveness  $\bar{\eta}_f$  in equation (5.4) correlates the film cooling temperature  $T_f$  with the temperature of the hot gases  $T_h$  and the coolant temperature  $T_c$ .

$$\bar{\eta}_f = \frac{T_h - T_f}{T_h - T_c} \quad (5.4)$$

Jabbari and Goldstein (1978) [19] proposed an equation that calculates the laterally averaged film cooling effectiveness for a flat surface with two rows of cooling holes with a parameter  $\epsilon$ . The parameter  $\epsilon$  is defined as:

$$\epsilon = \frac{6 \chi}{M \pi D_{hole}} \left( Re_c \frac{\mu_c}{\mu_h} \right)^{-0.25}, \quad (5.5)$$

where:

1.  $\mu_c$  and  $\mu_h$  represent the dynamic viscosity of the coolant and hot gases flow respectively. Furthermore,  $Re_c$  is the Reynolds calculated for the film channel which diameter is  $D_{hole}$ .
2.  $M$  is the **blowing rate**:  $M = \frac{\rho_c V_c}{\rho_h w}$ .  $V_c$  is the velocity of the coolant in the film holes. A blowing ratio  $M = 0.5$  and film hole diameter of  $D_{hole} = 2 \text{ mm}$  [16] are selected.
3.  $\chi$  is the streamwise distance from the film holes ( $0 < \chi < l$ ).

The laterally averaged film effectiveness  $\bar{\eta}_{flat}$  is computed as:

$$\bar{\eta}_{flat} = (1 + 0.249\epsilon)^{-0.8} \quad (5.6)$$

Far downstream the film holes ( $\frac{\chi}{D_{hole}} > 5$ ) the  $\bar{\eta}_{flat}$  decreases as the gas-coolant mixture temperature diminishes. Therefore,  $\bar{\eta}_{flat}$  is streamwise averaged in equation (5.7).

$$\bar{\eta}_f = \frac{\int_0^l \bar{\eta}_{flat}(\chi) d\chi}{l} \quad (5.7)$$

Summarizing, equation (5.7) computes the (laterally & streamwise) averaged film effectiveness  $\bar{\eta}_f$ . Hence, the film temperature can be computed using equation (5.4):

$$T_f = T_h - \bar{\eta}_f (T_h - T_c). \quad (5.8)$$

The further step is the computation of the heat transfer  $Q_{ext}$ . In order to do so, the heat transfer coefficient  $h_{ext}$  has to be estimated. Hence, Prandtl and Reynolds numbers are calculated:

$$Pr_h = \frac{c_{p_h} \mu_h}{k_h} \quad (5.9)$$

$$Re_h = \frac{\rho_h w l}{\mu_h} \quad (5.10)$$

where  $c_{p_h}$ ,  $\mu_h$  and  $k_h$  represent the heat capacity of at constant pressure, dynamic viscosity and thermal conductivity of the hot gases respectively. Knowing both the Reynolds and Prandtl numbers, the Nusselt number is estimated. If the flow regime is laminar ( $Re_h < 10^4$ ) equation (5.12) calculates the Nusselt. Otherwise, for turbulent regimes ( $Re_h > 10^4$ ) equation (5.11) is used [2].

$$Nu_h = 0.0228 Re_h^{\frac{4}{5}} Pr_h^{\frac{1}{3}}. \quad (5.11)$$

$$Nu_h = 0.331 Re_h^{\frac{1}{2}} Pr_h^{\frac{1}{3}}. \quad (5.12)$$

From the definition of the Nusselt number, the heat transfer coefficient is calculated:

$$h_{ext} = \frac{k_h Nu_h}{l} \quad (5.13)$$

Finally, the external heat transfer  $Q_{ext}$  is calculated as:

$$Q_{ext} = h_{ext} A_{ext} (T_f - T_{max}). \quad (5.14)$$

At the middle-trailing edge the results of the calculations for the external heat transfer for one blade are shown in table 5.2.

Parameter	Value	Description
$\bar{\eta}_f$	4.08 %	Streamwise & laterally averaged film effectiveness
$T_h$	1022 [°C]	Hot gases temperature
$T_f$	994.6 [°C]	Film temperature
$h_{ext}$	911.6 W/m <sup>2</sup> .K	External heat transfer coefficient
$A_{ext}$	18cm <sup>2</sup>	External heat transfer area
$Q_{ext}$	155.28 W/m <sup>2</sup> .K	External heat transfer

Table 5.2: Turbine cooling model: external heat transfer design calculations for the middle-trailing edge.

**Leading edge** External heat transfer in the leading edge occurs due to convection between the hot gases and the wall. No film cooling is applied in the leading edge. The calculation of the heat transfer is similar to the previous section with the following differences:

- $\bar{\eta}_{film} = 0$  since no film cooling is applied.
- The external heat transfer area is  $A_{ext} = h w_c$  as shown in figure 5.11.

At the leading edge the results of the calculations for the external heat transfer for one blade are shown in table 5.3.

Parameter	Value	Description
$\bar{\eta}_f$	0 %	Streamwise & laterally averaged film effectiveness
$T_h = TIT$	1093 [ $^{\circ}C$ ]	Hot gases temperature
$T_f = T_h$	1093 [ $^{\circ}C$ ]	Film temperature
$h_{ext}$	594.47 W/ $m^2.K$	External heat transfer coefficient
$A_{ext}$	6 $m^2$	External heat transfer area
$Q_{ext}$	68.84 W/ $m^2.K$	External heat transfer

Table 5.3: Turbine cooling model: external heat transfer design calculations for the leading edge.

### 5.2.2. Internal heat transfer ( $Q_{int}$ )

The coolant mass flow for internal cooling is the sum of the coolant required for impingement  $\dot{m}_{c_{imp}}$  and convection  $\dot{m}_{c_{conv}}$ , that is:

$$\dot{m}_{coolant} = \dot{m}_{imp} + \dot{m}_{conv} \quad (5.15)$$

A fraction of the compressor discharge flow is used to cooled down the turbine blades. This fraction, regarded as cooling to main-stream ratio ( $CMR$ ), is defined as the ratio between the coolant mass flow ( $\dot{m}_{coolant}$ ) and the GT airflow ( $\dot{m}_a$ ):

$$CMR = \frac{\dot{m}_{coolant}}{\dot{m}_a} = \frac{\dot{m}_{imp} + \dot{m}_{conv}}{\dot{m}_a} = CMR_{conv} + CMR_{imp} \quad (5.16)$$

The next two paragraphs of this section elaborates on convective and impingement heat transfer.

**Convective heat transfer (middle-trailing edge)** The following assumptions are made in order to compute the internal heat transfer due to convection  $Q_{conv}$  fo a given coolant flow  $\dot{m}_{c_{conv}}$  :

1. No turbulators in the cooling channels.
2. No radiation heat transfer between the cooling mass flow and the wall (and vice versa).
3. The temperature of the wall is constant across the channels to simplify the calculations.

Furthermore, typical values of the cooling channels geometry are selected defined in table 5.4 [16].:

Parameter	Value	Description
Hcc	6 $mm$	Channel height
Wcc	2.5 $mm$	Channel width
Acc	15 $mm^2$	Channel cross sectional area
$d_h$	3.5 $mm$	Hydraulic diameter of the channel
$n_{CC}$	4	Number of parallel cooling channels

Table 5.4: Cooling channels geometry

For a given coolant mass flow  $\dot{m}_{conv}$  that flows in one of cooling channels the heat transfer coefficient due to convection  $h_{conv}$  is computed as follows:

The velocity in the channel  $V_m$  is computed according to equation (5.17):

$$V_m = \frac{\dot{m}_{conv}}{\rho A_{cc}}, \quad (5.17)$$

where  $\rho$  is the density of the coolant mass flow before entering the channels. At this position the Prandlt and Reynolds numbers are computed:

$$Pr = \frac{c_p \mu}{k}. \quad (5.18)$$

$$Re = \frac{\rho V_m d_h}{\mu}. \quad (5.19)$$

where  $c_p$ ,  $\mu$  and  $k$  represent the heat capacity at constant pressure, dynamic viscosity and thermal conductivity of the coolant before entering the channels respectively. Knowing both the Reynolds and Prandtl numbers, the Dittus-Boelter equation estimates the Nusselt number inside the channel [2]:

$$Nu = 0.023 Re^{0.8} Pr^{0.4}. \quad (5.20)$$

The further step is the computation of the internal heat transfer coefficient due to convection  $h_{conv}$ . From the definition of the Nusselt number, the heat transfer coefficient is calculated:

$$h_{conv} = \frac{k Nu}{d_h}. \quad (5.21)$$

Figure 5.13 shows the coolant mass flow path when it enters the channel.

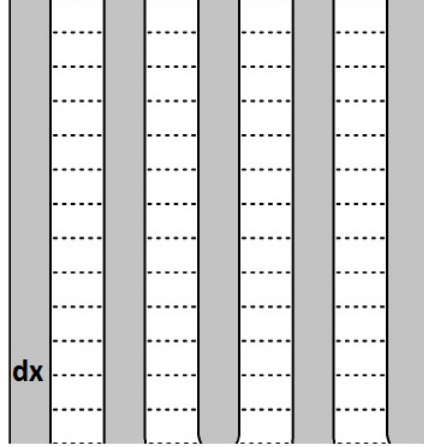


Figure 5.13: Internal cooling: longitudinal cut of the cooling channels in a turbine blade/vane

In particular, as the cooling airflow passes through the cooling channel its temperature increase, hence its thermodynamic properties (density, conductivity and dynamic viscosity) change and so the heat transfer coefficient. Therefore, a discretization of the mass flow path in "n" small control volumes of length  $dx$  is necessary in order to estimate the average internal transfer coefficient due to convection. The smaller the  $dx$ , the more accurate the estimation.

In this iterative calculation, the outlet temperature of one control volume is the inlet temperature of the next. Therefore, for  $i = 1, 2, 3 \dots n$ , the cooling heat  $Q_{conv_i}$  and the outlet temperatures of each control volume  $T_{i+1}$  are computed in an iterative calculation:

$$Q_{channel_i} = \frac{2 \pi d_h dx (T_{max} - T_i)}{\frac{1}{h_{conv_i}} + R_s}, \quad (5.22)$$

$$T_{i+1} = T_i + \frac{Q_{channel_i}}{c_{p_i} \dot{m}_{imp}}, \quad (5.23)$$

where  $R_s$  is the heat transfer resistance due to conduction in the blade (figure 5.9).

The total heat due to convection per channel is the sum of the heat absorbed in the "n" control volumes by the coolant and considering there are  $n_{CC} = 4$  cooling channels (see table 5.4):

$$Q_{channel} = \sum_{i=1}^{n_{CC}} Q_{channel_i}. \quad (5.24)$$

An average heat transfer coefficient can be defined as:

$$\bar{h}_{conv} = \frac{Q_{channel}}{A_{conv} (T_{max} - T_c)}, \quad (5.25)$$

where  $A_{conv} = 2 \pi d_h w_c$  is the heat transfer area of the channel.

From assumption 3, the wall temperature was assumed to be constant. Hence, if the same coolant mass flow

enters the other  $n_{CC} - 1$  channels, the coolant will absorb the same heat in all the channels and the total heat transfer due to convection  $Q_{conv}$  is computed as:

$$Q_{conv} = n_{CC} Q_{channel}. \quad (5.26)$$

For convective cooling the accuracy of the estimation of the heat transfer coefficient depends on the number of discretizations points of the cooling path as previously discussed previously. Figure 5.14 show the asymptotic behavior of the coolant outlet temperature when increasing the number of discretizations.

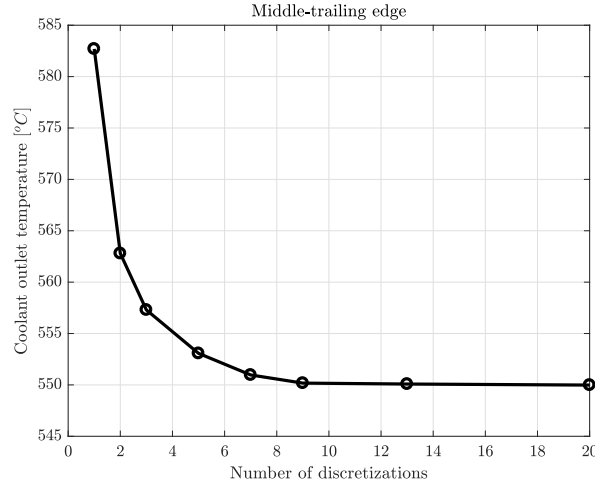


Figure 5.14: Turbine cooling model. Design calculations of the coolant outlet temperature for convection cooling. The solution converges for infinite numbers of discretizations.

The number of discretization of 13 is selected because the solution is enough accurate and a higher number of discretizations points will be a waste of CPU time. The results of the computation are shown in the table 5.5.

Parameter	Value	Description
$m_{conv}$	0.72 g/s	Coolant airflow for convection per vane/blade
$\bar{h}_{conv}$	70.1 W/m <sup>2</sup> .K	Averaged internal heat transfer coefficient of one channel channel
$A_{conv}$	10.2 cm <sup>2</sup>	Heat transfer area of one channel
$Q_{conv}$	155.4 W/m <sup>2</sup> .K	Internal heat transfer per vane/blade

Table 5.5: Turbine cooling model. Design results for internal cooling in the middle-trailing edge.

**Jet impingement** This type of cooling system is used where the most critical conditions exist, for example the stagnation point of a rotor blade ( $TIT = T_h$ ) [16]. In jet impingement cooling, the coolant passes through the jet nozzles inside the blade and impinges the hot metal surface (figure 5.15) resulting in a high heat transfer coefficient. After impinging the metal surface, the coolant mass flow heads to the exit. Furthermore, figure 5.15 shows the impingement array configuration and table 5.6 exhibits the design parameter for this case study. For a given coolant flow  $\dot{m}_{imp}$ , if  $A_j$  is the impingement area, the number of jets  $n_j$  and the coolant mass flow  $\dot{m}_j$  per jet are calculated as:

$$n_j = \frac{A_j}{L_{jx} L_{jy}}, \quad (5.27)$$

$$\dot{m}_j = \frac{\dot{m}_{imp}}{n_j} \quad (5.28)$$

The coolant flow in the nozzles  $Q_j$  per unit area is computed according to the mass balance at the jet nozzle in equation (5.29):

$$Q_j = \frac{4 \dot{m}_j}{\pi d_j^2}, \quad (5.29)$$

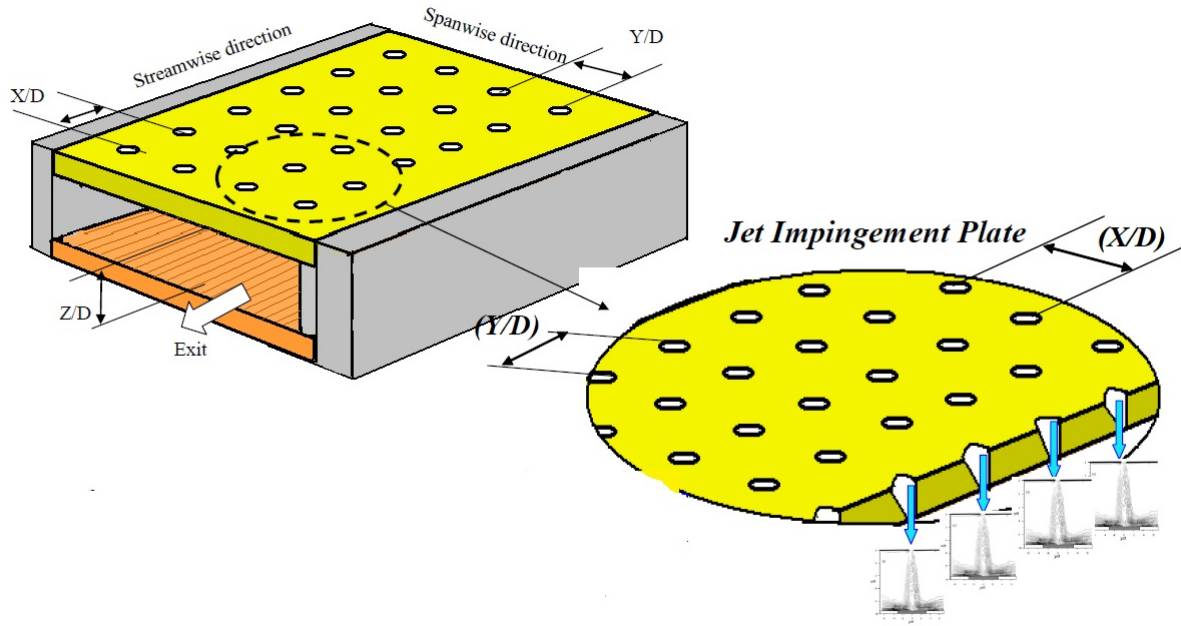


Figure 5.15: Internal cooling: jet impingement array.

Parameter	Value	Description
$d_j$	1 mm	Jet/nozzle diameter
$x/d$	3	Stream-wise distribution
$y/d$	2.5	Span-wise distribution
$z/d$	1	Height distribution
$n_{jy}$	4	Number of jets span-wise
$n_{jx}$	20	Number of jets stream-wise
$L_{jy} = n_{jy} y/d d$	h	Span-wise length
$L_{jx} = n_{jx} x/d d$	$w_c$	Stream-wise length
$A_j = L_{jy} L_{jx}$	6 cm <sup>2</sup>	Jet impingement area

Table 5.6: Design impingement cooling - geometry parameters.

The procedure followed to estimate the heat transfer due to impingement is based on the paper “Streamwise Flow and Heat Transfer Distributions for Jet Array Impingement with Cross flow” [15]. Before the coolant enters the jets, the Prandlt and Reynolds numbers are computed:

$$Pr = \frac{c_p \mu}{k} \quad (5.30)$$

$$Re_j = \frac{Q_j d_j}{\mu} \quad (5.31)$$

where  $\rho$ ,  $c_p$ ,  $\mu$  and  $k$  represent the density, heat capacity at constant pressure, dynamic viscosity and thermal conductivity of the coolant respectively. The flow distribution parameter (which changes depending on the array configuration) and the jet discharge coefficient are defined. [15]:

$$\beta = \frac{C_D \sqrt{2} \frac{\pi}{4}}{\left(\frac{y}{d}\right) \left(\frac{z}{d}\right)} \quad (5.32)$$

From now on, an iterative calculation is done for each of the jet nozzles that the array contains in the stream-wise direction  $x$ . The first jet has a sub index of 1 until the last jet that will have the sub index  $n_{jx}$  (figure

5.16).

$$\frac{x_i}{x_{n_{jx}}} = \left(i - \frac{1}{2}\right) \quad \text{for } i = 1, 2, \dots, n_{jx} \quad (5.33)$$

It was possible to estimate the channel cross flow mass velocity  $Q_c(x_i)$  based on the channel cross-sectional area [15]:

$$\frac{Q_c(x_i)}{Q_j} = \frac{1}{\sqrt{2} C_D} \frac{\sinh \left[ \beta \left( \frac{x_i}{x_{n_{jx}}} - \frac{1}{2} \right) \right]}{\cosh \left[ \beta \left( \frac{x_i}{x_{n_{jx}}} \right) \right]} \quad \text{for } i = 1, 2, \dots, n_{jx}. \quad (5.34)$$

The following assumptions were made in order to estimate the heat transfer coefficient due to impingement  $h_{imp}$ :

1. The fluid properties are constant across the jet array.
2. A jet discharge coefficient of  $C_D = 0.4$  has been selected [15].

Following Florschütz's paper [15] the Nusselt number can be estimated. But first a set of coefficient and exponent must be defined using equation (5.35) and table 5.7.

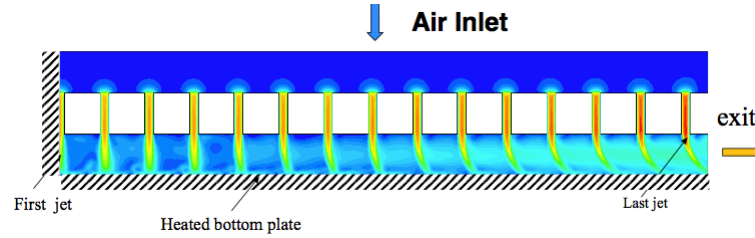


Figure 5.16: Internal cooling: velocity distribution in jet impingement array.

Coefficient	C	nx	ny	nz
A	1.18	-0.944	-0.0642	0.169
m	0.612	0.059	-0.032	-0.022
B	0.437	-0.095	0.219	0.275
n	0.092	-0.005	0.599	1.04

Table 5.7: Constants to use in equation (5.35) [15].

$$A, m, B \text{ and } n = C \left(\frac{x}{d}\right)^{nx} \left(\frac{y}{d}\right)^{ny} \left(\frac{z}{d}\right)^{nz}. \quad (5.35)$$

Finally the correlation for the Nusselt number is given in equation (5.36) [15]:

$$Nu_i = A Re_j^m \left\{ 1 - B \left[ \left( \frac{z}{d} \right) \left( \frac{Q_c(x_i)}{Q_j} \right) \right]^n \right\} Pr^{\frac{1}{3}} \quad \text{for } i = 1, 2, \dots, n_{jx}. \quad (5.36)$$

Therefore, the heat transfer coefficients for each jet nozzle can be easily computed:

$$h_i = \frac{Nu_i k_i}{d_j} \quad \text{for } i = 1, 2, \dots, n_{jx}. \quad (5.37)$$

An averaged heat transfer coefficient due to impingement is defined in equation (5.38) and the averaged heat transfer calculated in equation (5.39) :

$$h_{imp} = \overline{h_{imp}} = \frac{\sum_{i=1}^{n_{jx}} h_i}{n_{jx}}, \quad (5.38)$$

$$Q_{imp} = \overline{Q_{imp}} = \frac{A_j (T_{max} - T_c)}{\frac{1}{h_{imp}} + R_s}, \quad (5.39)$$

where  $R_c$  is the heat resistance due to convection in the blade (figure 5.9).

Impingement is responsible for the highest heat transfer coefficients [16]. This happens due to the high velocities of the jets in the impingement array (figure 5.15). The velocity changes from jet to jet. In particular, the results from figure 5.17a are conclusive on the effect of the interaction between the jets streamwise. In this type of jet array (inline), the cross velocity increases the farther the cooling air is from the first jet. This increase will be faster at first but later on will become slower. As a matter of fact, there is an accumulation of air in the streamwise direction making an increase in the cross flow velocity. Furthermore, the flow of air has the main constrain that all the flow must exit at the end of the streamwise channel. This has a direct effect on the heat transfer of the downstream jets because the interaction between jets in the streamwise direction upstream produce a cross velocity that will reduce the cooling effect of the jet impingement on the downstream. Figure 5.17b shows the Nusselt number is inversely proportional to the cross velocity.

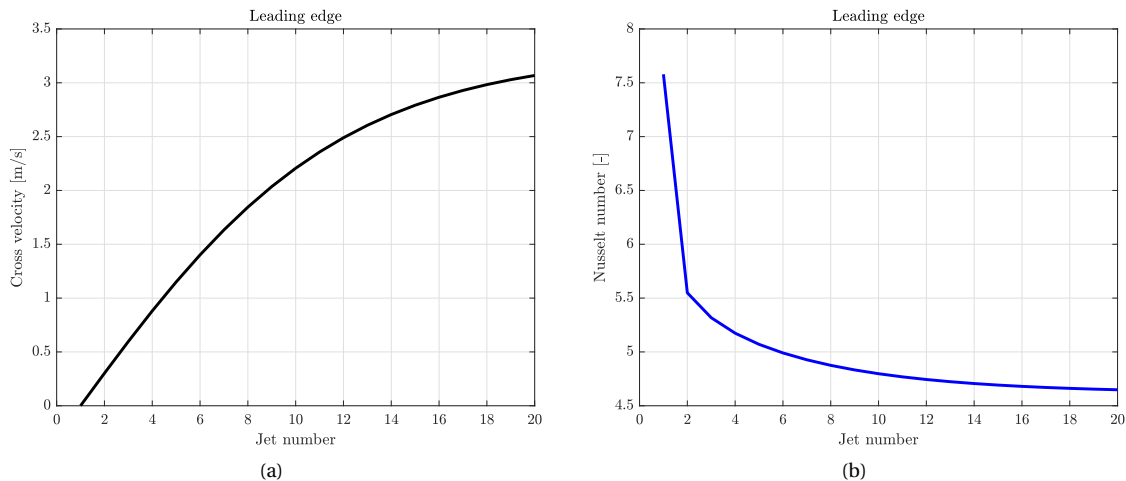


Figure 5.17: Turbine cooling model. Cross flow velocity (a) and Nusselt number per jet (b) for impingement cooling.

The behavior of the Nusselt number across the streamwise channel is similar (but inverse) to the one shown by the cross velocity. A rapid decrease at first and then it stabilizes. When designing a jet impingement is important to take into account this phenomenon that will reduce the cooling effect of the system. This implies that the higher cross velocity the lower the heat transfer coefficient due to impingement. A possible solution is to combine jet impingement with film cooling so that the streamwise flow is no longer confined.

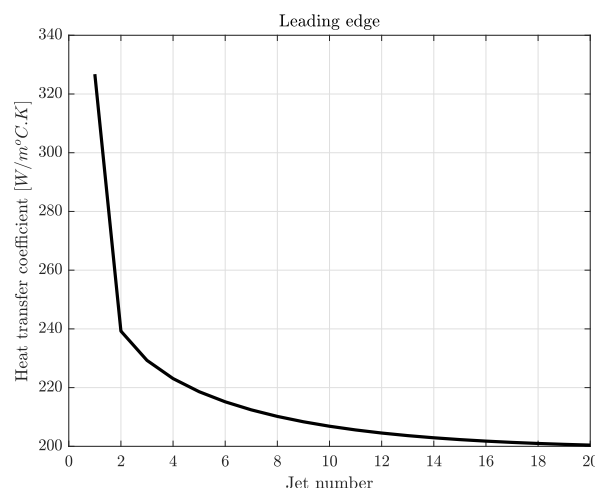


Figure 5.18: Turbine cooling model. Heat transfer coefficient per jet for impingement cooling.

The results for impingement cooling are shown in the table 5.8.

Parameter	Value	Description
$\dot{m}_{imp}$	0.39 g/s	Coolant airflow per vane/blade for impingement
$h_{imp}$	209 W/m <sup>2</sup> .K	Averaged internal heat transfer coefficient for impingement
$Q_{imp}$	68.97 W/m <sup>2</sup> .K	Internal heat transfer for impingement
$A_j$	6cm <sup>2</sup>	Jet impingement heat transfer area

Table 5.8: Turbine cooling model. Design results for internal cooling in the leading edge.

### 5.3. Part load operation

At part load the internal and external heat transfer vary. In particular, the variables that mostly influence the heat transfer are the following:

- 1 Coolant mass flow. The design coolant flow for each vane/blade is calculated in the previous section. At part load the GT airflow decreases and so the coolant mass flow does (see chapter 2). For the OD case studies, the coolant to main- stream ratios  $CMR_{imp}$  and  $CMR_{conv}$  are assumed constant. For instance, if the GT airflow decreases by the 10%, it implies the coolant mass flow diminishes also by 10%.
- 2 Thermodynamic properties of the coolant before entering the blades/vanes. The compressor temperature and pressure change at part load (see chapter 2) and so the thermodynamic properties (density, thermodynamic conductivity, dynamic viscosity etc.) of the coolant do. These changes have an impact on the internal heat transfer coefficients  $h_{conv}$  and  $h_{imp}$ .
- 3 Thermodynamic properties of the turbine flow. Similarly to item 2, the thermodynamic properties of the turbine mass flow vary. These changes have an impact on the external heat transfer coefficient  $h_{ext}$ .
- 4 Coolant flow composition. For FGR control the composition of the coolant mass flow changes since the the flue gases are recirculated to the GT inlet . The flue gas composition is shown in table 5.9 below from chapter 3.

$GT_{load}$	Volumetric percentage [%]			
	$CO_2$	$H_2O$	$N_2$	$O_2$
100	0.37	1.03	77.8	20.72
88.7	0.6	2.64	76.46	19.37
79	1.23	4.56	75.47	17.74
68	2.56	8.22	73.64	14.7

Table 5.9: FGR for CHP plant. Volumetric percentage composition at the GT inlet. Data taken from chapter 3.

- 5 Velocity of the hot gases (w) in the turbine. For simplification, this velocity is assumed constant at part load.

### 5.3.1. Coolant flow

In this section the impact of the most important variables that affect the blades/vanes temperature is investigated both for IGV and FGR control.

1. Coolant mass flow. Figure 5.19 shows how the coolant mass flow change at part load for both IGV and FGR control. For obvious reasons, the lower the coolant flow, the higher the metal temperature.

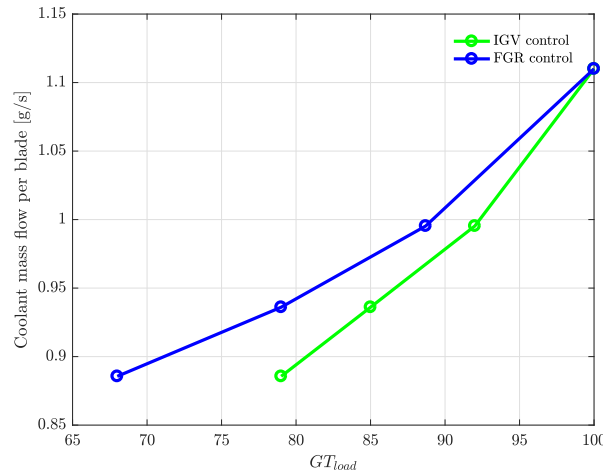


Figure 5.19: Turbine cooling model. Coolant mass flow at part load.

2. Coolant temperature and pressure. Figures 5.20a and 5.20b shows how the coolant pressure and temperature vary for both controls. When the coolant pressure decreases, so the mass flow velocity in the jet nozzles and cooling tubes do. For lower Reynolds, the heat transfer coefficients decrease and as a consequence the metal temperature rises. On the other hand, for obvious reasons the lower the coolant temperature the lower the blade temperature (figure 5.20b).

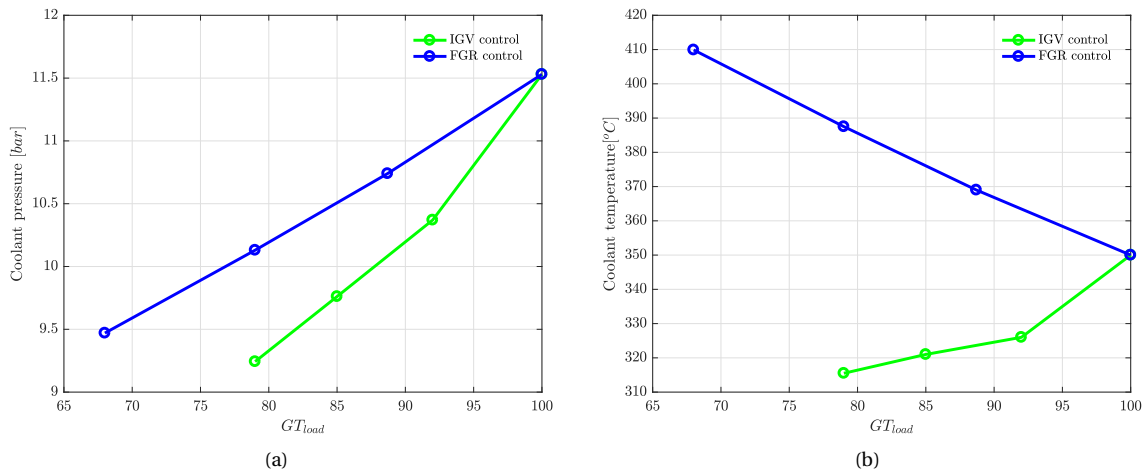


Figure 5.20: Turbine cooling model. Coolant pressure(a) and temperature (b) at part load.

3. Coolant flow composition (see table 5.9). For FGR control the composition of the coolant mass flow changes since the the flue gases are recirculated to the GT inlet and they mix with ambient air to the GT inlet as discussed in chapter 2 and 3.

### 5.3.2. Off-design simulations

Initial guesses of the blade temperature both for impingement and convection cooling are made. The heat transfer coefficients and film effectiveness are calculated using the calculation procedure of sections 5.2.2 and 5.2.1. If thermal equilibrium is reached, the calculation is stopped. Otherwise, the blade temperature is increased and simulations runs until the differences  $\Delta Q_1$  between  $Q_{conv}$  and  $Q_{ext}$  and  $\Delta Q_2$  between  $Q_{imp}$  and  $Q_{ext}$  meet the convergence criteria  $\Delta Q_1, \Delta Q_2 < 0.5W$ .

The OD computations are similar to the design calculations with the only difference that for the off-design calculations the blade temperatures (of the leading and middle-trailing edges) are the unknowns whereas the coolant mass flows are knowns (figure 5.19). The results for both IGV and FGR controls are presented below. Figure 5.21 show how the temperature of the blade varies at part load in the leading and middle-trailing edges.

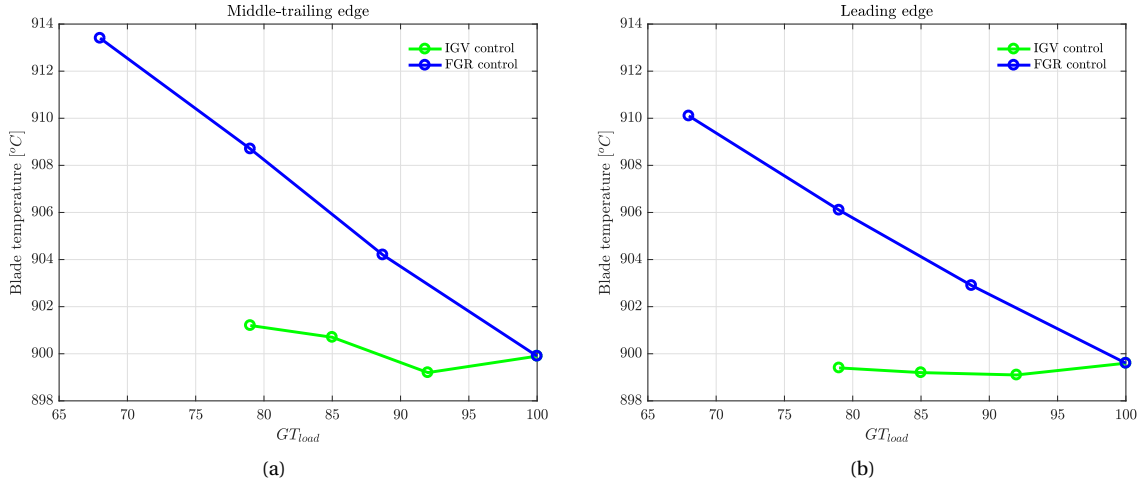


Figure 5.21: Turbine cooling model. Blade temperature profile at part load for FGR and IGV controls for the middle-trailing(a) and leading(b) edges.

**IGV control** When reducing the plant load closing the guide vanes, the coolant pressure and temperature decrease (figures 5.20a and 5.20b). Although the internal heat transfer coefficient decrease because the coolant pressure diminishes (see previous section), the coolant temperature drop keeps the metal temperature almost constant.

**FGR control** On the other hand, for the FGR control the coolant temperature increases at part load. This causes the metal temperature to increase up to  $914^{\circ}C$ . The change in coolant composition does not affect significantly the heat transfer: figure 5.22 shows the effect of the coolant composition on the heat transfer. If the compressor inlet composition did not change when recirculating the flue gases, the blade temperature would decrease less than 0.1%. This happens because the Prandtl number (responsible for the change in thermodynamic properties) remains almost constant at part load (see appendix). Finally, figure 5.23 shows the film effectiveness slightly changes at part load. In the appendix, the change in heat transfer coefficient, Reynolds, Nusselt and Prandtl numbers are shown in detail both for IGV and FGR control.

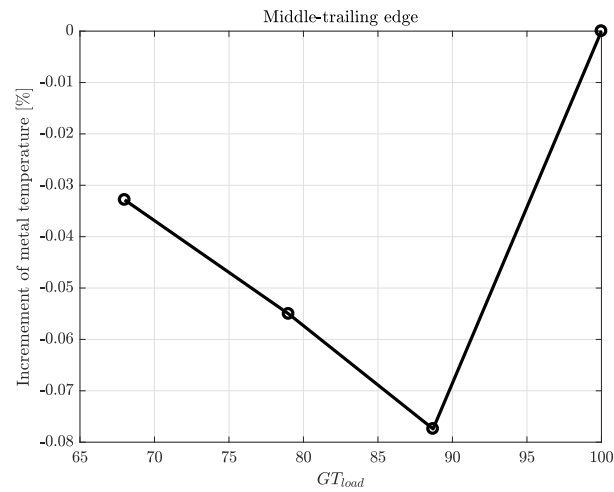


Figure 5.22: Turbine cooling model for FGR control. Percent of metal temperature increase if the coolant composition would not change.

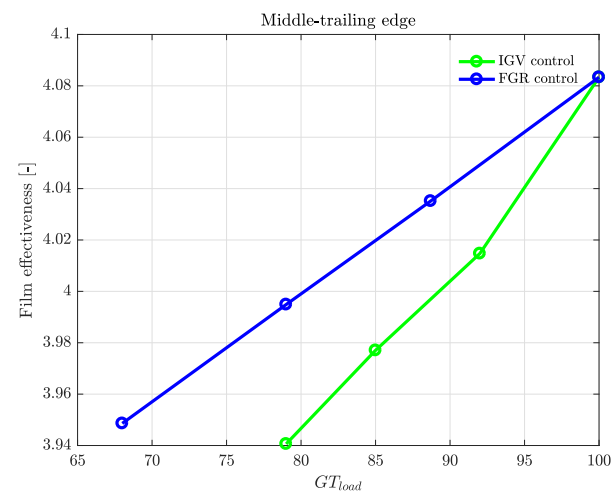


Figure 5.23: Turbine cooling model for FGR control. Film cooling effectiveness at part load for IGV and FGR controls.

## 5.4. Conclusions

The object of this section was to evaluate the impact of part load operation on the turbine blade/vane temperature. The results of simulations estimate an increase of the turbine metal temperature at part load for FGR since the coolant temperature rises at part load. The change of the coolant composition due to the recirculation of the exhaust gases does not affect the heat transfer. On the other hand, when closing the guide vanes the blades/vanes temperature stays almost constant.



# 6

## Case study including duct/blower calculations and limitation imposed by the turbine blade temperature

This chapter is about a case study of the combined heat and power plant modeled in chapter 3. Unlike chapter 3, the proposed combination controls of this chapter take into account the duct/blower (required to push the air to the gas turbine inlet) calculations and the limitations imposed by the maximum turbine blade temperature. Sections 6.1 and 6.2 elaborates on the turbine blade temperature limitation and on the duct/blower calculations respectively.

### 6.1. Proposed solutions to the limitation imposed by the turbine temperature

In chapter 5, it was found that the turbine cooling imposes a limitation on the FGR control because the blade temperature exceeds the limit of  $T_{max} = 900^{\circ}C$  and the proposed control of chapter 3 (see figure 6.1) has to be adjusted to meet the maximum blade temperature requirements.

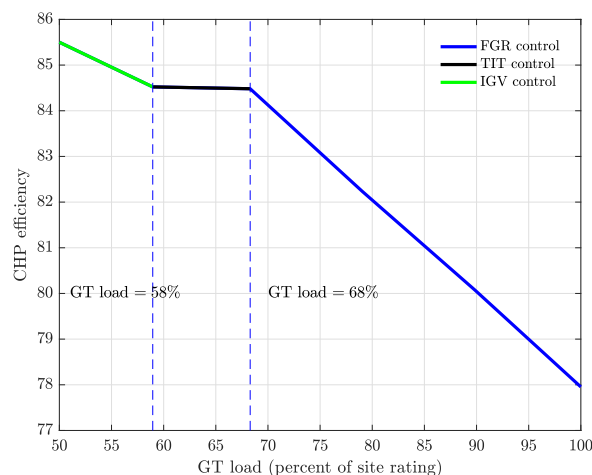


Figure 6.1: Optimum control combination for the CHP plant of chapter 3.

Therefore, the GT load cannot be decreased from 100 to 68 % just recirculating the exhaust gases to the GT inlet otherwise the turbine blade temperature will exceed the maximum allowable temperature. In order to overcome this issue two alternatives are proposed in sections 6.1.1 and 6.1.2.

### 6.1.1. FGR&TIT+ IGV combination control

One possible solution is to initially decrease the GT load by combining FGR with some another control that decreases the turbine blade temperature at part load. The following part load combinations are analyzed:

1. FGR & CAR control. The combination of CAR with FGR cannot decrease the blade temperature at part load since CAR control, similarly to FGR, increases the compressor discharge temperature keeping the TIT constant.
2. FGR & IGV control. This solution is not acceptable since at part load the reduction of the blade temperature is so small for IGV (see figure 5.21) that it is not worth to combine these two controls.
3. FGR & TIT control. The TIT control has the effect of decreasing the hot gases temperature and therefore the turbine blade temperature.

The combination of FGR and TIT control is selected since when decreasing the GT TIT the heat absorbed by the blade decreases and so the blade temperature. The control of figure 6.1 is adjusted in accordance with the blade cooling requirements imposed by the turbine. The new control combination is proposed in figure 6.2. In such a control, the GT load is decreased by recirculating the flue gases and by decreasing the turbine inlet temperature at the same time. The turbine cooling model of chapter 5 is used to calculate the TIT at which the blade temperature is  $T_{max} = 900^{\circ}C$ . However, when combining the TIT with the FGR control the efficiency of the combined heat and power plant decreases since the TIT control is least efficient control for the combined heat and power plant as previously discussed in chapter 3.

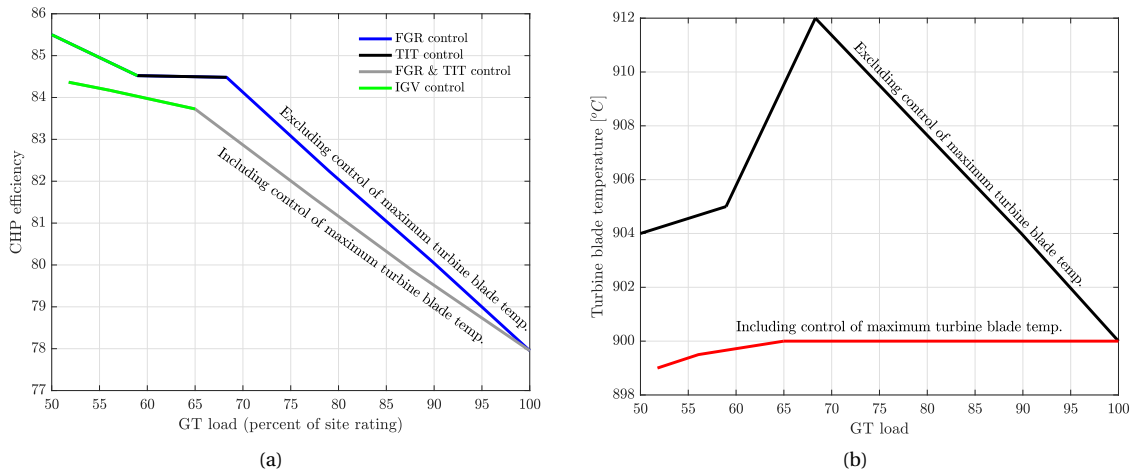


Figure 6.2: Case study. FGR&TIT+ IGV combination control (including control of maximum turbine blade temperature) (a) and turbine blade temperature profile at part load.

### 6.1.2. IGV + FGR&TIT combination control

Another way of maintaining the turbine blade temperature below  $T_{max} = 900^{\circ}C$  is to initially decrease the load via IGV control. When reaching the maximum vane closure, the flue gases are recirculated and the TIT is reduced at the same time to ensure the the temperature of the blade stays below the maximum temperature (similarly to section 6.1.1). Figures 6.3 show the control curve.

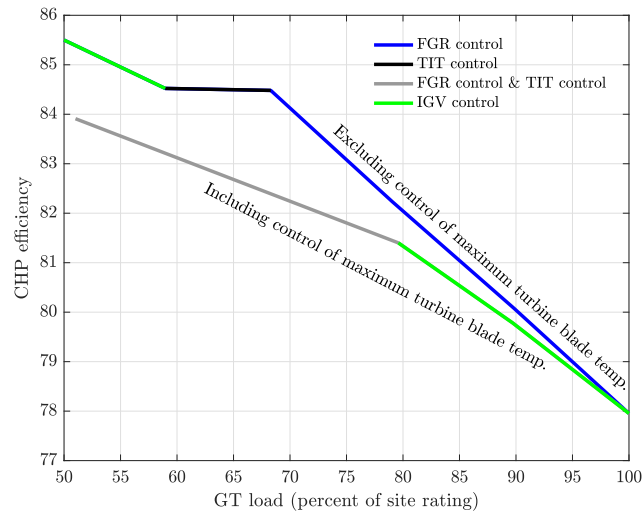


Figure 6.3: Case study. IGV + FGR&TIT combination control (including control of maximum turbine blade temperature).

## 6.2. Blower

When recirculating the exhaust gases a blower (figure 6.4) and a exhaust duct have to be placed to push the air to the inlet of the gas turbines.

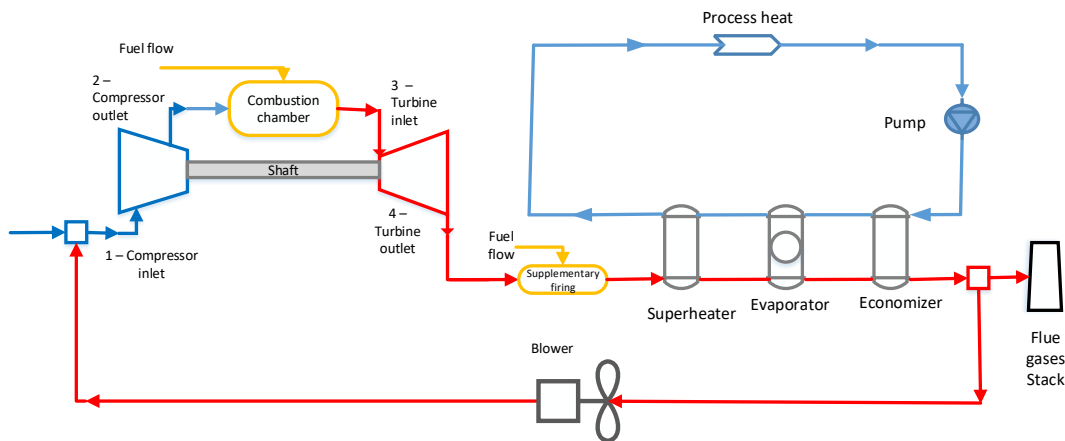


Figure 6.4: CHP plant flow diagram with blower.

In industry, a blower is a centrifugal fan that provides a pressure rise against the duct resistance where the air flows through. In addition to the duct pressure losses, since the stack temperature of the flue gases is relatively high ( $\approx 130^{\circ}C$ ), the duct is insulated by a layer (of thickness  $t_i = 5cm$ ) of resin bonded glasswool. The glasswool caters up to  $230^{\circ}C$  and its thermal conductivity is quite low ( $k_g = 0.04W/m.K$ ) to ensure a good thermal insulation.

In this case study, the heat losses to the surroundings are considered negligible. Furthermore, the selected duct has a length of  $L = 20m$  and diameter of  $D_{duct} = 1.2m$ . For the duct and blower calculations, the density of the exhaust air is assumed to be constant and equal to  $\rho_{duct} = 0.89kg/m^3$ .

**Velocity in the exhaust duct** The velocity in the ducts is calculated according to the mass balance equation:

$$v_{duct} = \frac{m_{duct}}{\rho_{duct} A_{duct}} \tag{6.1}$$

$v_{duct}$  depends on the mass flow  $m_{duct}$  and therefore on the percentage of recirculated flue gases and on the GT airflow.

**Duct pressure losses** The pressure losses depend on the velocity in the duct and therefore on the percentage of exhaust gases recirculated in accordance with equation (6.1). There are two kind of pressure drops: the duct distributed pressure losses ( $\Delta P_d$ ) and the duct fitting losses ( $\Delta P_f$ ):

$$\Delta P_{duct} = \Delta P_d + \Delta P_f \tag{6.2}$$

- The distributed pressure losses concern the losses due to friction along the pipe. At low speed ( $Mach_{duct} < 0.3$ ) the air behaves as an incompressible fluid [24]. Therefore, in order to estimate the distributed pressure losses along the duct  $\Delta P_{duct}$ , the Darcy -Weisbach equation [25] is used:

$$\Delta P_d = C_d \frac{L}{D_{duct}} \rho_{duct} \frac{v_{duct}^2}{2} \tag{6.3}$$

where  $C_d$  is a dimensionless friction factor and  $\rho_{stack}$  is the density of the stack flow.

The only unknown in equation (6.3) is  $C_d$  and it can be estimated knowing the roughness of the duct  $\epsilon$  using the Coolebrok-White equation [25]:

$$\frac{1}{\sqrt{C_d}} = -2 \log \left( \frac{2.51}{Re_{duct} \sqrt{C_d}} + \frac{\epsilon_{duct}}{3.71 D_{duct}} \right) \tag{6.4}$$

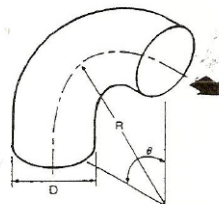
The typical surface roughness of an industrial duct is  $\epsilon_{duct} = 0.001 m$  [25].

If the mass flow recirculated is known, the distributed pressure losses can be computed. For instance, when the engine load is 65% (via FGR control) using equation (6.4) the friction factor  $C_d$  is estimated to be equal to 0.004 and  $\Delta P_d$  was found to be approximately 8 Pa.

- Fittings such as elbows and tees are responsible for high pressure losses in a duct system. It is assumed that 5 elbows are required to recirculate the exhaust gases to the GT inlet. Figure 6.5 shows the selected elbow geometry: for a 90° elbow with a R/D ratio of 0.5 the dimensionless fitting friction factor  $C_f$  is 0.71. The duct fitting pressure losses are computed multiplying the fitting friction factor by the dynamic

Use the velocity pressure ( $V_v$ ) of the upstream section. Fitting loss (TP) = C ×  $V_v$

A. Elbow, Smooth Radius (Die Stamped), Round(2)



Coefficients for 90° Elbows: (See Note 1)

R/D	0.5	0.75	1.0	1.5	2.0	2.5
C	0.71	0.33	0.22	0.15	0.13	0.12

Note 1: For angles other than 90° multiply by the following factors:

θ	0°	20°	30°	45°	60°	75°	90°	110°	130°	150°	180°
K	0	0.31	0.45	0.60	0.78	0.90	1.00	1.13	1.20	1.28	1.40

Figure 6.5: Fitting pressure losses for a 90° C curved elbow [17].

velocity pressure  $\rho_{duct} \frac{v_{duct}^2}{2}$ :

$$\Delta P_f = 5 C_f \rho_{duct} \frac{v_{duct}^2}{2} \tag{6.5}$$

In general, the pressure losses depends on the velocity in the duct. For the optimum control of figure 6.2b, the maximum exhaust flow (and therefore velocity) in the tube is detected when the engine load is 65% by recirculating the flue gasaes to the GT inlet. At this load, the fitting pressure losses were found to be around 6.4 kPa. The distributed pressure losses are small compared to the fitting pressure losses ( 8 « 6400 Pa).

**Blower power** The blower has to provide a pressure rise of  $\Delta P_{duct}$ . The blower power can be estimated using equation 6.6:

$$P_{blower} = \frac{\dot{m}_{duct}}{\rho_{duct}} \frac{\Delta P_{duct}}{\eta_{blower}}, \quad (6.6)$$

where  $\eta_{blower} = 0.8$  is the blower efficiency [17].

The blower power can be therefore computed at part load for both the combined controls of section 6.1.1 and 6.1.2.

#### Example of calculation for the FGR&TIT + IGV combination control

For the FGR&TIT + IGV combination control proposed when diminishing the plant load the exhaust gases start to recirculate. The velocity in the recirculating duct increases (figure 6.6) until reaching a maximum of  $46\text{ m/s}$  before closing the inlet guide vanes.

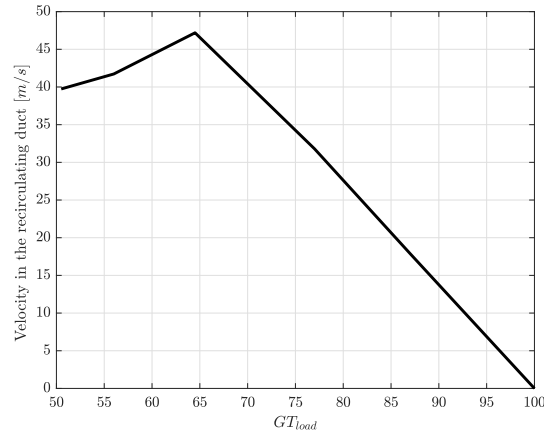


Figure 6.6: Velocity profile in the recirculating duct for the deep part load control.

Figure 6.7a shows how the blower power changes at part load of figure 6.2a. Similarly to the velocity profile, when recirculating the exhaust gases the blower power increases until it reaches a peak when the engine load is 65%. At 65% of the GT load the percentage of oxygen reached the minimum value of 14.5%. Hence, the IGV control is applied and the blower power decreases since the GT airflow diminishes.

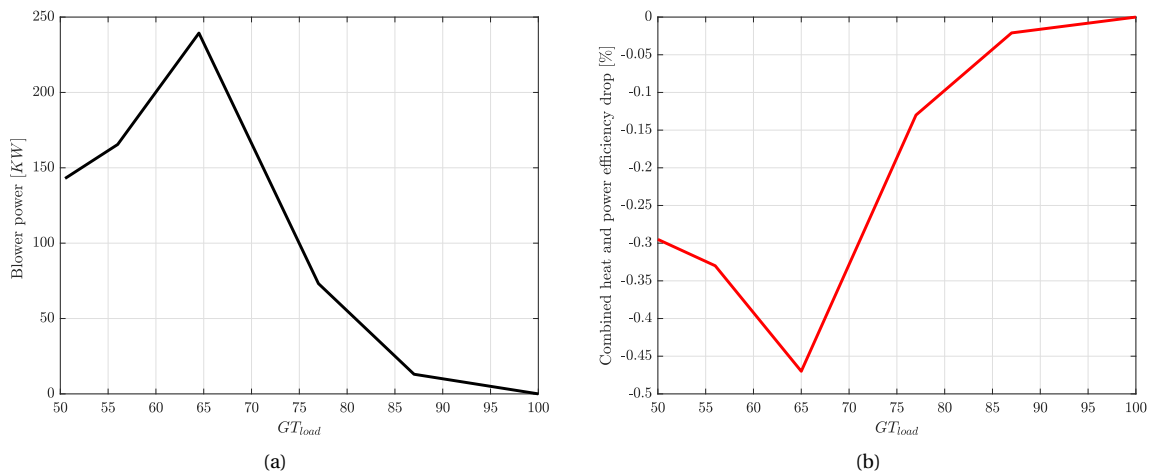


Figure 6.7: Blower power(a) and CHP plant efficiency drop (b) with respect to the optimum control with turbine cooling limitations of figure 6.2a

The combined heat and power efficiency slightly drops due to the use of the blower as shown in figure 6.7b. The maximum efficiency drop of the combined heat and power plant is found to be 0.45% when the blower power is maximum (GT load =65%).

### 6.3. Summary and conclusions

Figure 6.8 is representative for the results of this case study. Two optimized controls are proposed: the FGR&TIT + IGW and IGW + FGR&TIT combination controls.

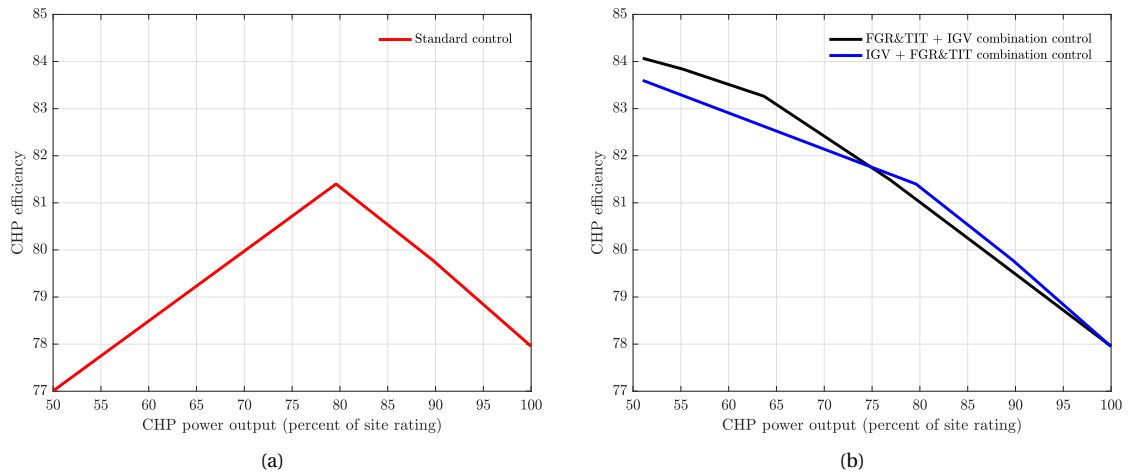


Figure 6.8: Results of the case study: combined heat and power plant efficiency at part load for the different controls.

As previously discussed in chapter 3, the standard control is a combination of IGW and TIT controls. Although for this control the part load efficiency increases up to around 81.5%, for gas turbines loads lower than 80%, the part load efficiency drops because the TIT control is inefficient for a combined heat and power plant. In order to increase the part load efficiency, two part load combination controls are proposed. Unlike the optimum control proposed in chapter 3, this chapter takes into account the duct/blower calculations and the limitation imposed by the maximum turbine blade temperature. For obvious reasons, at deep part load ( $GT_{load} < 75\%$ ), the FGR&TIT + IGW combination control is selected increasing the part load cycle efficiency up to 9% with respect to the standard control. On the other hand if, for any reason the CHP plant has to produce more electricity ( $GT_{load} > 75\%$ ), the IGW + FGR&TIT combination is chosen.

# Conclusions and recommendations

## 7.1. Conclusions

The objective of this master thesis is to enable part load operation with FGR and to quantify the operating range and efficiency of the different control strategies for a combined cycle and a combined heat and power installation. In order to do so, a systematic approach has been used.

The part-load operation equations for the thermodynamic modeling of a GT were derived and four control techniques were studied in detail: TIT, IGV, CAR and FGR control. The Brayton model developed has been validated with THERMOFLEX and it reproduces the OD operation of the GE6531B with an accuracy higher than 99 %. Some of the limiting factors of the part load operation of the GT are identified:

- The risk of compressor stalling/surging has been investigated in the compressor map. The guide vanes can close down to a minimum airflow whereas for the other controls there is no risk of surge/stall.
- For the FGR control, the minimum oxygen concentration at the GT inlet limits the operation of the combustion chamber. When recirculating the exhaust gases, OD simulations are run down to the oxygen concentration of 14.5% in order to guarantee an efficient and stable combustion.
- Another limiting factor of the GT part load operation is the maximum turbine blade temperature. The turbine cooling model presented evaluates the turbine cooling requirements in a stage design and predicts the effects of part load operation on the performance and durability of the gas turbine. The results of simulations estimate an increase of the turbine metal temperature at part load for FGR because of increase of the coolant temperature at part load. The change of the coolant composition due to recirculation of the exhaust gases does not affect the heat transfer. On the other hand, when closing the guide vanes the blade temperature stays almost constant.
- When recirculating the exhaust gases a blower and an exhaust duct have to be placed to push the air to the inlet of the gas turbines.

The part load controls are applied to a combined heat an power plant and combined cycle. Several important results are found:

- the FGR control is the most efficient control because of the lowest stack losses.
- The TIT control (which was the second most efficient part load technique for the Brayton model) is the least efficient. Nevertheless, if the TIT control is used in combination with FGR control, its efficiency improves.
- The use of FGR improves the part load efficiency of the modeled CHP plant up to 9% with respect to the traditional control strategies. The calculations take into account the following limiting factors: risk of compressor stall/surge, minimum oxygen concentration of 14.5%, maximum turbine blade temperature of 900 °C and blower/duct calculations.

- The use of FGR improves the part load efficiency of the modeled CC up to 7% with respect to the traditional control strategies. Unlike the CHP plant the boiler inlet temperature limits the part load operation. The calculations take into account the following limiting factors: risk of compressor stall/surge, minimum oxygen concentration of 14.5% and maximum boiler inlet temperature of 650°C.

## 7.2. Recommendations

Future studies should focus on the following aspects:

- **Combustion stability at reduced Oxygen levels.** For the FGR control, the minimum oxygen concentration at the GT inlet was assumed to be 14.5% from the literature. The reduction of oxygen levels and the increase of reactants temperature lean toward MILD combustion [31] which is known to be stable and with low emissions. The fundamental mechanisms appearing in FGR combustion are not well identified and the control strategies to stabilize the combustion have been limited to macro-studies. More research is required on this topic, on a fundamental level, to enable and improve combustion under FGR conditions.
- **Part load emissions.** Another part load limiting factor is given by the plant emissions (NO<sub>x</sub>, CO, CO<sub>2</sub> and unburned hydrocarbons). In particular, FGR is a common technology for NO<sub>x</sub> reduction [9], but only some indicative studies are available. These studies focus mostly on increasing CO<sub>2</sub> levels in exhaust gases [7, 13, 21, 23, 27] to facilitate CO<sub>2</sub> capture. Further studies can quantify the emissions of the part load control proposed.
- For the **turbine cooling model** developed the following improvements can be implemented:
  - Validation of the model with existing models in literature.
  - The blades were assumed to have a parallelepipedal shape for the sake of simplicity. Further studies can investigate the heat transfer on a real turbine blade (airfoil shape).
  - Including the pin fin cooling as internal heat transfer mechanism.
- **Economic study.** The business case of power plants is difficult in a fluctuating energy market that requires more and more flexibility with increasing pressure on the reduction of emissions. FGR could be used to retro-fit current installations into profitable installations. However, applying the enlarged FGR conditions and modifying the plants requires verifying the interest of applying this technology on existing installations. This could be performed through a techno-economic analysis of how power plants would perform with FGR.

# Appendix

## A - Simple Brayton model: TIT control

For the TIT control the system of non-linear equations is the following:

$$\left\{ \begin{array}{l} \dot{m}_{aOD} = \dot{m}_a \quad \text{Stonewall assumption} \\ T_{1OD} = T_1 \\ T_{2OD} = T_{1OD} \left[ \frac{\left( \Pi_{OD}^{\frac{k-1}{k}} - 1 \right)}{\eta_{isC}} + 1 \right] \quad \text{OD Compressor discharge temperature} \\ \dot{m}_{fOD} LHV + \dot{m}_{aOD} c_p T_{2OD} = (\dot{m}_{aOD} + \dot{m}_{fOD}) c_{pFG} T_{3OD} \quad \text{OD Combustor energy balance} \\ \Pi_{OD} = \Pi \sqrt{\frac{T_{3OD}}{T_3} \frac{(\dot{m}_{aOD} + \dot{m}_{fOD})}{(\dot{m}_a + \dot{m}_f)}} \quad \text{OD GT pressure ratio} \\ T_{4OD} = T_{3OD} \left[ \left( \frac{1}{\Pi_{OD}^{\frac{k_{FG}-1}{k_{FG}}}} - 1 \right) \eta_{isT} + 1 \right] \quad \text{OD Turbine discharge temperature} \end{array} \right. \quad (7.1)$$

Six equations with six unknowns (in red). For a given OD TIT ( $=T_{3OD}$ ) the system of equations is solved in MATLAB.

## B - Simple Brayton model: IGV control

For the IGV control the system of non-linear equations is the following:

$$\left\{ \begin{array}{l} \dot{m}_{aOD} = \dot{m}_a \frac{\cos(\alpha_{IGV} + \alpha_1)}{\cos(\alpha_1)} \quad \text{OD compressor air flow} \\ T_{1OD} = T_1 \\ T_{2OD} = T_{1OD} \left[ \frac{\left( \Pi_{OD}^{\frac{k-1}{k}} - 1 \right)}{\eta_{isC}} + 1 \right] \quad \text{OD Compressor discharge temperature} \\ \dot{m}_{fOD} LHV + \dot{m}_{aOD} c_p T_{2OD} = (\dot{m}_{aOD} + \dot{m}_{fOD}) c_{pFG} T_{3OD} \quad \text{OD Combustor energy balance} \\ T_{3OD} = T_3 \quad \text{Constant turbine inlet temperature} \\ \Pi_{OD} = \Pi \sqrt{\frac{T_{3OD}}{T_3} \frac{(\dot{m}_{aOD} + \dot{m}_{fOD})}{(\dot{m}_a + \dot{m}_f)}} \quad \text{OD GT pressure ratio} \\ T_{4OD} = T_{3OD} \left[ \left( \frac{1}{\Pi_{OD}^{\frac{k_{FG}-1}{k_{FG}}}} - 1 \right) \eta_{isT} + 1 \right] \quad \text{OD Turbine discharge temperature} \end{array} \right. \quad (7.2)$$

Seven equations with seven unknowns (in red). For a given  $\alpha_{IGV}$  the system of equations is solved in MATLAB.

## C - Simple Brayton model: CAR control

For the CAR control the system of non-linear equations is the following:

$$\left\{ \begin{array}{l} \dot{m}_{aOD} = \dot{m}_a \sqrt{\frac{T_1}{T_{1OD}}} \quad \text{OD compressor air flow - Air Preheating} \\ x = \frac{T_{1OD} - T_1}{T_{2OD} - T_1} \quad \text{Energy and mass balance at the mixer (GT inlet)} \\ T_{2OD} = T_{1OD} \left[ \frac{\left( \Pi_{OD}^{\frac{k-1}{k}} - 1 \right)}{\eta_{isC}} + 1 \right] \quad \text{OD Compressor discharge temperature} \\ \dot{m}_{fOD} LHV + \dot{m}_{aOD} c_p T_{2OD} = (\dot{m}_{aOD} + \dot{m}_{fOD}) c_{pFG} T_{3OD} \quad \text{OD Combustor energy balance} \\ \Pi_{OD} = \Pi \sqrt{\frac{T_{3OD}}{T_3} \frac{(\dot{m}_{aOD} (1-x) + \dot{m}_{fOD})}{(\dot{m}_a + \dot{m}_f)}} \quad \text{OD GT pressure ratio} \\ T_{4OD} = T_{3OD} \left[ \left( \frac{1}{\Pi_{OD}^{\frac{k_{FG}-1}{k_{FG}}}} - 1 \right) \eta_{isT} + 1 \right] \quad \text{OD Turbine discharge temperature} \end{array} \right. \quad (7.3)$$

Seven equations with seven unknowns (in red). For a given  $T_{1OD}$  the system of equations is solved in MATLAB.

## D - Simple Brayton model: FGR control

For the FGR control the system of non-linear equations is the following:

$$\left\{ \begin{array}{l}
 \dot{m}_{aOD} = m_a \sqrt{\frac{T_1}{T_{1OD}}} \quad \text{OD compressor airflow - Air Preheating} \\
 x = \frac{T_{1OD} - T_1}{T_{4OD} - T_1} \quad \text{Energy and mass balance at the mixer (GT inlet)} \\
 T_{2OD} = T_{1OD} \left[ \frac{\left( \Pi_{OD}^{\frac{k-1}{k}} - 1 \right)}{\eta_{isC}} + 1 \right] \quad \text{OD Compressor discharge temperature} \\
 \dot{m}_{fOD} LHV + \dot{m}_{aOD} c_p T_{2OD} = (\dot{m}_{aOD} + \dot{m}_{fOD}) c_{pFG} T_{3OD} \quad \text{OD Combustor energy balance} \\
 T_{3OD} = T_3 \quad \text{Constant turbine inlet temperature} \\
 \Pi_{OD} = \Pi \sqrt{\frac{T_{3OD}}{T_3} \frac{(\dot{m}_{aOD} + \dot{m}_{fOD})}{(\dot{m}_a + \dot{m}_f)}} \quad \text{OD GT pressure ratio} \\
 T_{4OD} = T_{3OD} \left[ \left( \frac{1}{\Pi_{OD}^{\frac{k_{FG}-1}{k_{FG}}}} - 1 \right) \eta_{isT} + 1 \right] \quad \text{OD Turbine discharge temperature}
 \end{array} \right. \quad (7.4)$$

Seven equations with seven unknowns (in red). For a given  $T_{1OD}$  the system of equations is solved in MATLAB.

### E - CC flowdiagram at design

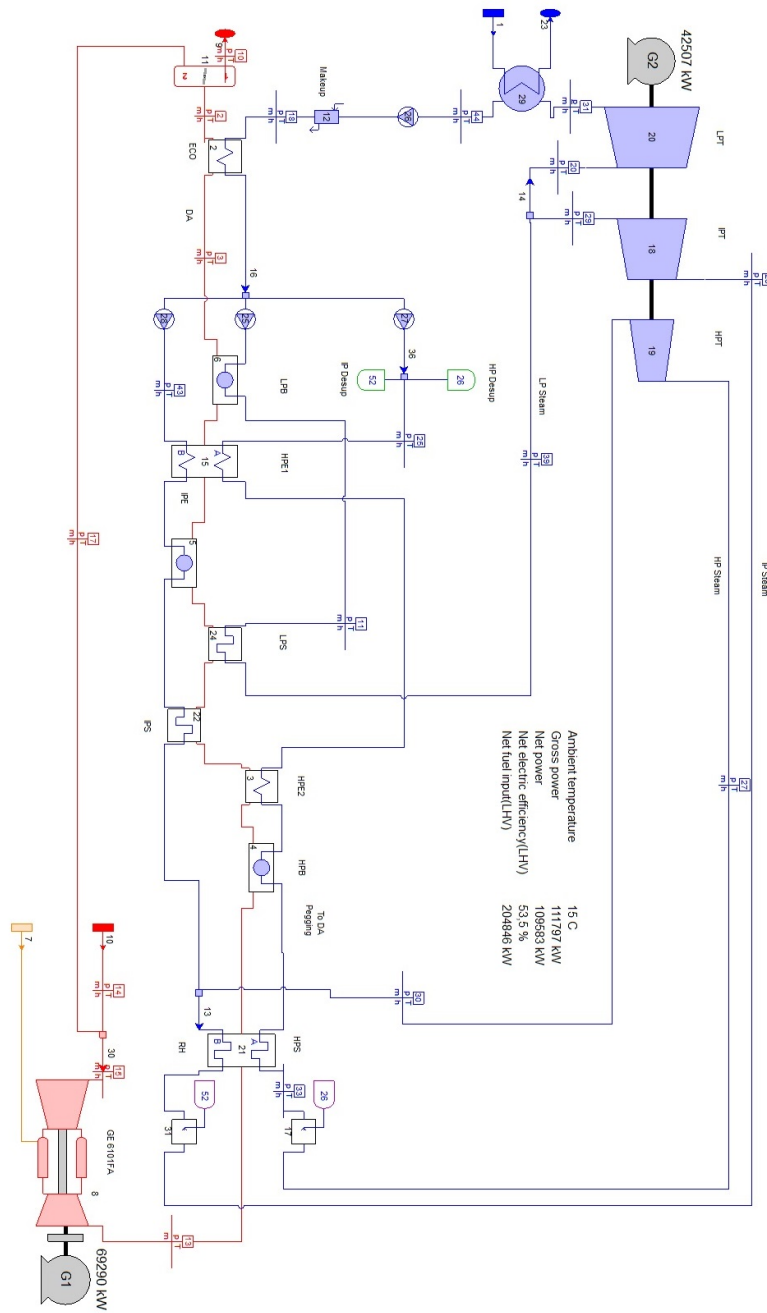


Figure 7.1: Combined cycle flow diagram at design.

## F - Turbine cooling model - Results of part load simulation IGV control

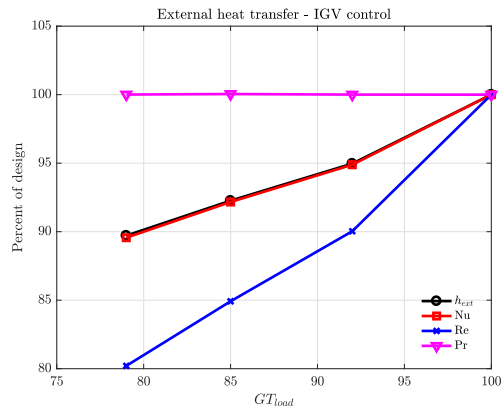


Figure 7.2: Turbine cooling model. External heat transfer for IGV control.

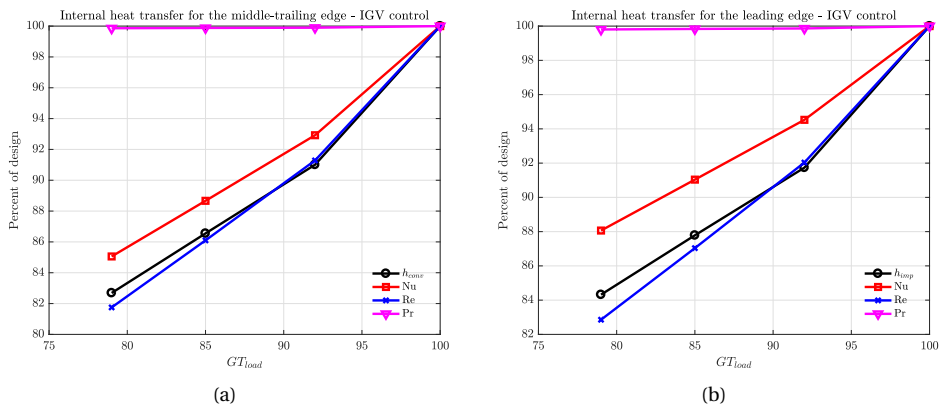


Figure 7.3: Turbine cooling model. Internal heat transfer for convection cooling (a) and impingement cooling (b) for IGV control.

### FGR control

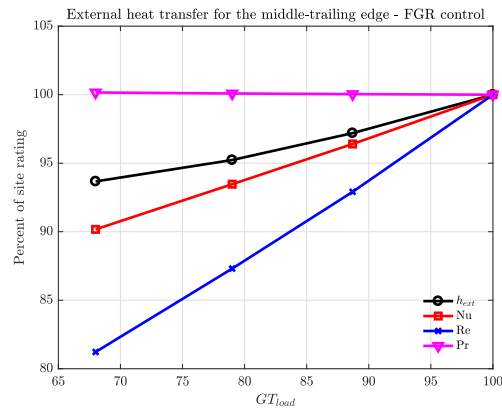


Figure 7.4: Turbine cooling model. External heat transfer for FGR control.

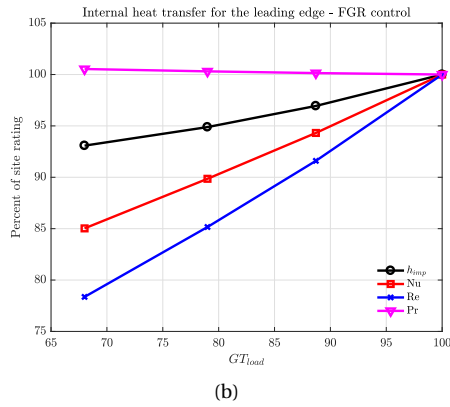
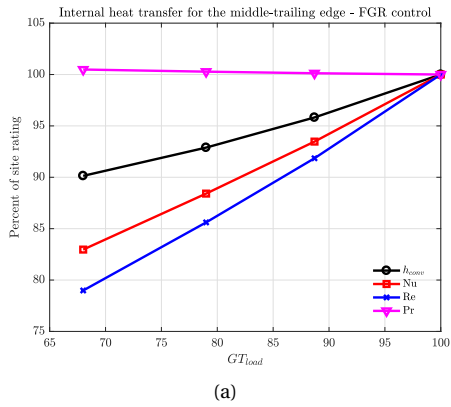


Figure 7.5: Turbine cooling model. Internal heat transfer for convection cooling (a) and impingement cooling (b) for FGR control.



# Bibliography

- [1] Variable Inlet Guide Vanes Boost Centrifugal Air Compressor Efficiency. <http://www.airbestpractices.com/technology/air-compressors/variable-inlet-guide-vanes-boost-centrifugal-air-compressor-efficiency>. Accessed: 2010-04-05.
- [2] Adrian Bejan. *Convection heat transfer*. John Wiley & Sons, 2013.
- [3] Thom Best, Karen N Finney, Derek B Ingham, and Mohamed Pourkashanian. Impact of CO<sub>2</sub>-enriched combustion air on micro-gas turbine performance for carbon capture. *Energy*, 115:1138–1147, 2016.
- [4] Olav Bolland and Philippe Mathieu. Comparison of two CO<sub>2</sub> removal options in combined cycle power plants. *Energy Conversion and Management*, 39(16):1653–1663, 1998.
- [5] Meherwan P Boyce. *Gas turbine engineering handbook*. Elsevier, 2011.
- [6] Anne Sjoerd Brouwer, Machteld van den Broek, Ad Seebregts, and André Faaij. Operational flexibility and economics of power plants in future low-carbon power systems. *Applied Energy*, 156:107–128, 2015.
- [7] Maria Cristina Cameretti, Renzo Piazzesi, Fabrizio Reale, and Raffaele Tuccillo. Combustion simulation of an exhaust gas recirculation operated micro-gas turbine. *Journal of engineering for gas turbines and power*, 131(5):051701, 2009.
- [8] P Colonna and TP Van der Stelt. Fluidprop: a program for the estimation of thermo physical properties of fluids. *Energy Technology Section, Delft University of Technology, Delft, The Netherlands*, <http://www.FluidProp.com>, 2004.
- [9] Arthur R Dinicolantonio. Flue gas recirculation for NO<sub>x</sub> reduction in premix burners, March 3 1992. US Patent 5,092,761.
- [10] Mario Ditaranto, Jørgen Hals, and Tor Bjørge. Investigation on the in-flame NO reburning in turbine exhaust gas. *Proceedings of the Combustion Institute*, 32(2):2659–2666, 2009.
- [11] S Larry Dixon and Cesare Hall. *Fluid mechanics and thermodynamics of turbomachinery*. Butterworth-Heinemann, 2013.
- [12] Ahmed M Elkady, Andrei Evulet, Anthony Brand, Tord Peter Ursin, and Arne Lynghjem. Application of exhaust gas recirculation in a DLN F-class combustion system for postcombustion carbon capture. *Journal of Engineering for Gas Turbines and Power*, 131(3):034505, 2009.
- [13] Andrei T Evulet, Ahmed M Elkady, Anthony R Branda, and Daniel Chinn. On the performance and operability of GE's dry low NO<sub>x</sub> combustors utilizing exhaust gas recirculation for postcombustion carbon capture. *Energy Procedia*, 1(1):3809–3816, 2009.
- [14] Mauro Felli. *Lezioni di fisica tecnica*, volume 1. Morlacchi editore, 2004.
- [15] LW Florschuetz, CR Truman, and DE Metzger. Streamwise flow and heat transfer distributions for jet array impingement with crossflow. In *ASME 1981 International Gas Turbine Conference and Products Show*, pages V003T09A005–V003T09A005. American Society of Mechanical Engineers, 1981.
- [16] Je-Chin Han, Sandip Dutta, and Srinath Ekkad. *Gas turbine heat transfer and cooling technology*. CRC Press, 2012.
- [17] ASHRAE Handbook. HVAC systems and equipment. *American Society of Heating, Refrigerating, and Air Conditioning Engineers, Atlanta, GA*, 1996.

- [18] AR Howell. *The Present Basis of Axial Flow Compressor Design. Pt. 1. Cascade Theory and Performance*. HM Stationery Office, 1942.
- [19] MY Jabbari and RJ Goldstein. Adiabatic wall temperature and heat transfer downstream of injection through two rows of holes. *Journal of Engineering for Power*, 100(2):303–307, 1978.
- [20] TS Kim. Comparative analysis on the part load performance of combined cycle plants considering design performance and power control strategy. *Energy*, 29(1):71–85, 2004.
- [21] Jonathan Lewis, Richard Marsh, Agustin Valera-Medina, Steven Morris, and Hesham Baej. The use of co2 to improve stability and emissions of an igcc combustor. In *ASME Turbo Expo 2014: Turbine Technical Conference and Exposition*, pages V04AT04A029–V04AT04A029. American Society of Mechanical Engineers, 2014.
- [22] Eric Martinot. Renewables. global futures report 2013. 2013.
- [23] Timothy C Merkel, Xiaotong Wei, Zhenjie He, Lloyd S White, JG Wijmans, and Richard W Baker. Selective exhaust gas recycle with membranes for co2 capture from natural gas combined cycle power plants. *Industrial & Engineering Chemistry Research*, 52(3):1150–1159, 2012.
- [24] Michael J Moran. Engineering thermodynamics. In *The CRC Handbook of Mechanical Engineering, Second Edition*. CRC Press, 2004.
- [25] Bruce Roy Munson, Donald F Young, and Theodore H Okiishi. Fundamentals of fluid mechanics. *New York*, 3(4), 1990.
- [26] Ronald C Pampreen. *Compressor surge and stall*. Concepts Eti, 1993.
- [27] Petter E Røkke and Johan E Hustad. Exhaust gas recirculation in gas turbines for reduction of co2 emissions; combustion testing with focus on stability and emissions. *International Journal of thermodynamics*, 8(4):167–173, 2005.
- [28] Claire Soares. *Gas turbines: a handbook of air, land and sea applications*. Butterworth-Heinemann, 2011.
- [29] IEA Statistics. Renewables information. *Paris, France: International Energy Agency*, 2016.
- [30] Motoaki Utamura, Shinichi Hoizumi, Yasushi Takeda, Toshihiko Sasaki, Hideaki Komatsu, Seiichi Kirikami, Takeshi Suzumura, Tetsuo Sasada, Takashi Ikeguchi, Shigehisa Sugita, et al. Gas turbine exhaust recirculation method and apparatus, March 20 2001. US Patent 6,202,400.
- [31] J Warnatz, U Maas, and RW Dibble. Combustion springer. *New York*, 1996.